UNIVERSITÉ DE MONTRÉAL

PHYSICAL MODELING OF THE HUMAN TRUNK FOR SIMULATION OF SCOLIOTIC SURGERY

RUI ZHANG
DÉPARTEMENT DE GÉNIE INFORMATIQUE
ÉCOLE POLYTECHNIQUE DE MONTRÉAL

MÉMOIRE PRÉSENTÉ EN VUE DE L'OBTENTION
DU DIPLOME DE MAÎTRISE ÈS SCIENCES APPLIQUÉES
(GÉNIE INFORMATIQUE)
AVRIL 2005

© Rui Zhang, 2005.

UNIVERSITÉ DE MONTRÉAL

ÉCOLE POLYTECHNIQUE DE MONTRÉAL

Ce mémoire intitulé :

PHYSICAL MODELING OF THE HUMAN TRUNK FOR SIMULATION OF SCOLIOTIC SURGERY

présenté par : ZHANG Rui

en vue de l'obtention du diplôme de : Maîtrise ès sciences appliquées

a été dûment accepté par le jury d'examen constitué de :

M., GUIBAULT François, Ph.D., président

Mme CHERIET Farida, Ph.D., membre et directrice de recherche

M., STEWART Neil, Ph.D., membre et codirecteur de recherche

M., DELORME Sébastien, Ph.D., membre

ACKNOWLEDGEMENTS

My deepest gratitude extends to Farida Cheriet, my thesis supervisor. She helped me tremendously to become a better researcher, and provided constant inspiration, feedback and support, as well as a wealthy of intriguing ideas and financial aid to make me able to finish my research. It was a great honor and a real pleasure for me to work with her. I sincerely thank Neil Stewart for acceptance to be my co-advisor. He gave me many helpful comments on the thesis. I also want to thank the members of my thesis committee, François Guibault and Delorme Sébastien, for their patience in reading drafts of my thesis, and their valuable feedback.

Special thanks to Qinhu Liao for many inciting conversations and good research ideas, for being a constant friend in good and bad times. He provided me the initial 3D solid mesh so that my research could continue.

Thanks to Valérie Pazos for beneficial cooperation. Her help with collecting and processing the raw data from patients is greatly appreciated.

The LIV4D research group is a stimulating and enjoyable research environment. I especially want to thank Jonathan Boisvert and Charles Bergeron for many useful suggestions and comments on my work. Thanks to Michel Archambault, Luke Windisch, Luc Duong, and Yueyun Shu for many inspiring conversations, and for their constant friendship and support.

Finally, a special thank to my wife and my family, who made many sacrifices over time to help me reach this point. Their love, support and encouragement has been invaluable over the years. This thesis is dedicated to them.

RÉSUMÉ

La scoliose est une déformation tridimensionnelle complexe du système musculo-squelettique qui est couplée, du point de vue biomécanique, à une rotation transversale des corps vertébraux et qui peut entraîner une cyphose anormale de la colonne thoracique et / ou une lordose de la colonne lombaire. Les patients sévèrement affectés doivent subir une chirurgie corrective par ostéosynthèse qui consiste à instrumenter la colonne en utilisant trois types d'implants : les tiges, les vis et les crochets afin d'exercer des forces sur les vertèbres de sorte à corriger les déformations. Pour simuler les corrections internes des vertèbres et de la surface externe sous l'effet de forces externes variables, plusieurs chercheurs ont appliqué différentes méthodes pour simuler la procédure de chirurgie. Un modèle d'éléments finis, qui cependant n'inclut pas les tissus mous, a été développé à l'Hôpital Sainte Justine de Montréal pour simuler la déformation de la cage thoracique et des vertèbres sous l'effet d'un traitement. La stratégie de chirurgie conventionnelle est basée sur l'expérience du médecin et un modèle préopératoire 3D du patient qui peut être mis à jour par recalage d'informations de positionnement intraopératoires (Bucholz 1994). L'objectif global de ce projet de maîtrise est de simuler l'effet d'une chirurgie sur la surface externe du tronc avant d'effectuer le traitement afin de fournir au chirurgien un outil qui va lui permettre de prendre de meilleures décisions dans le choix de la stratégie. Un modèle personnalisé 3D du tronc est obtenu par recalage d'un modèle préopératoire 3D des structures osseuses obtenu à partir des images à rayons-X et la surface externe 3D du tronc obtenue à partir d'un système de numériseurs 3D de la compagnie InSpeck Inc, Montréal.

Les objectifs spécifiques de ce projet consistent à (1) analyser et améliorer manuellement la qualité du maillage 3D décrivant le volume délimité par la surface externe du tronc et la surface des structures osseuses sous jacentes pour éviter des éléments non valides et améliorer la précision des résultats de simulation, (2) développer et évaluer un algorithme dynamique d'éléments finis pour simuler la déformation des structures à travers le temps, (3) calculer les conditions aux frontières en se basant sur un ensembles

de repères anatomiques identifiés sur les vertèbres avant et après la chirurgies, (4) valider l'algorithme proposé et évaluer les erreurs de précision en comparant les résultats simulés sur un modèle synthétique et les résultats de la même simulation obtenus à partir du logiciel ANSYS sur le même modèle, (5) Définir et mesurer une métrique d'erreur pour évaluer le modèle proposé à partir de données réelles d'un patient.

Nous avons d'abord obtenu un maillage du tronc complet d'un patient. La qualité du maillage a été ensuite évaluée à l'aide d'un paramètre approprié décrivant le rapport d'aspect calculé sur l'ensemble des tétraèdres composant le maillage, et le résultat analytique indiquait que certains tétraèdres avaient une forme géométrique non valide dans la région d'intersection entre le maillage des tissus mous et le maillage des vertèbres. Étant donné que les tétraèdres non valides affectent sévèrement la convergence vers la solution de l'équation différentielle numérique du système, ces derniers ont été réajustés manuellement. Les données réelles étant limitées à un seul patient, les opérations sur le maillage ont été effectuées de façon spécifique au patient utilisé pour l'évaluation du modèle.

Le développement de la méthode d'éléments finis a été effectué en deux étapes. La première étape était de choisir un polynôme linéaire comme fonction d'interpolation pour former un espace linéaire continu dans chaque tétraèdre et calculer son gradient interne. La matrice globale de rigidité est obtenue par assemblage des matrices de rigidité des tétraèdres, qui sont calculées selon différentes lois de comportement (élastique linéaire ou hyper-élastique non linéaire) et les paramètres biomécaniques spécifiques à la région d'appartenance du tétraèdre. La seconde étape est de construire une équation différentielle dynamique. Dans notre projet, une méthode d'intégration implicite a été implémentée et plusieurs facteurs comme la complexité et la précision des résultats ont été analysés afin de déterminer le schéma optimal. Pour fournir une procédure de déformations successives le schéma d'intégration de Newmark a été choisi pour résoudre l'équation différentielle ordinaire à travers le temps.

Les conditions aux frontières sont définies en se basant sur différents schémas de déformation. Dans le cas de déplacements pures, le déplacement d'un point est effectué

le long d'une ligne considérée comme la courbe d'interpolation linéaire entre deux extrémités qui désignent la position d'un ensemble de repères anatomiques identifiés sur les vertèbres avant et après la chirurgie. Le pas de déplacement est divisé de façon uniforme par un facteur de dix et le déplacement est effectué de façon graduelle jusqu'à atteindre l'état d'équilibre final. Le schéma d'application de forces consiste à considérer une série de ressorts dont une extrémité pointe toujours vers la position finale d'équilibre et se déplace le long de la courbe linéaire d'interpolation. L'autre extrémité produit une force élastique sur chaque vertèbre et entraîne le tronc complet à se déformer pour atteindre l'état d'équilibre.

La validation de l'algorithme proposé a été effectuée en comparant les résultats obtenus par la déformation d'un ensemble d'objets synthétiques simples à l'aide du code implémenté à ceux obtenus avec le logiciel ANSYS. La distance entre les surfaces des objets déformés par ANSYS et ceux déformés par l'algorithme proposé a été calculée. Une analyse quantitative des résultats obtenus a été effectuée afin d'estimer la précision du modèles proposé. Finalement, une comparaison des résultats de simulation sur les données réelles d'un patient a permis d'effectuer une évaluation préliminaire du modèle proposé. Un modèle d'éléments finis utilisant une propriété d'élasticité linéaire avec des déplacements purs a fourni de meilleurs résultats. La distance moyenne entre les surfaces simulées et les surfaces réelles est de 10.2607mm. Le classement par ordre du meilleur au plus pire est le modèle d'élément finis avec déplacements purs suivi du modèle avec un schéma linéaire d'application de forces et enfin un modèle basé sur un schéma non linéaire d'application de forces.

Nous avons démontré, à travers ce projet, la faisabilité d'utiliser une méthode d'éléments finis pour simuler l'effet d'une chirurgie correctrice de scoliose sur la surface externe du tronc. Cependant, la complexité du corps humain rend difficile la construction d'un maillage précis des différentes structures du tronc qui devrait inclure les différents organes ainsi que les interactions entre eux. Notre modèle étant limité à la surface externe du tronc et la surface des structures osseuses sous jacentes, il ne peut pas atteindre une haute précision. Par conséquent, une meilleure précision des résultats de

simulation nécessiterait le développement d'un maillage plus raffiné des différentes structures du tronc humain incluant les propriétés mécaniques des différents organes.

ABSTRACT

Scoliosis is a complex three-dimensional deformity of the musculo-skeletal system that is biomechanically coupled with a transverse rotation of the vertebral bodies and may be accompanied by abnormal kyphosis of the thoracic spine and /or lordosis of the lumbar spine. Severely affected patients must take corrective surgery by spine instrumentation with osteosynthesis, which uses three implantable elements: rod, hooks and screws to introduce forces on the vertebrae and to reduce the spinal deformities. To simulate the effect of deformation of internal vertebrae and the external surface under varied external forces, many researchers have applied different methods to simulate the procedure of surgery, and a good finite element model, which however does not include soft tissue, has been developed in Ste. Justine Hospital of Montreal to simulate the deformation of the rib cage and vertebrae. The traditional surgery strategy is based on the doctor's experience and the patient's three-dimensional preoperative model which can be updated with the real treated case to register it with intraoperative localization (Bucholz 1994). The global objective of this MSc project is to simulate the effect of surgery on the external surface of the trunk before scoliotic surgery and provide an approach to simulation to help the doctor make better decisions before surgery. A personalized 3D model is directly constructed by registering a preoperative 3D model built from patient's X-ray and his 3D external trunk surface coming from 3D image Capturer (InSpeck Inc, Montreal).

Specific objectives of this project consist of (1) analyze and enhance manually the quality of the acquired 3D mesh of the integral trunk to avoid bad elements and improve the simulated result, (2) develop and evaluate a dynamic finite element algorithm to simulate the procedure of deformation of the patient's internal surface over time, (3) compute the boundary conditions based on the position of points on vertebrae before and after surgery, (4) validate our algorithms and error accuracy by comparing our simulated results with theoretic values and ANSYS software simulated results, (5) define and

measure the error distance metric which is used to evaluate the model from real data for one patient.

We first obtained a complete trunk mesh for one patient. The mesh quality was then evaluated by a suitable aspect ratio parameter defined on a tetrahedron, and the analytic result indicated there are some tetrahedrons with bad geometric shape on the intersection region between the external soft tissue mesh and the vertebral mesh. The bad tetrahedrons severely influenced the convergence of the numerical differential equation solver, and thus are manually readjusted. Since we only obtained a single patient's data, all the operations on the mesh are only implemented on this scoliotic patient's data set.

The development of the finite element method was undertaken in two steps. The first step is to choose a linear polynomial as interpolation function, to form a linear continuous space in each tetrahedron and compute its inner gradient. The global stiffness matrix is obtained by assembling each small tetrahedral stiffness matrix, which is computed according to a different constitutive law (linear or nonlinear hyperelastic) and the specific biomechanical parameters in the region where it is situated. The second step is to construct a dynamic differential equation. In our project, the implicit integration method is implemented and its many factors such as time complexity, and accuracy of the result, are compared to determine the final scheme. To form a successive deformation procedure, the Newmark integration scheme was chosen to solve the ordinary differentiation equation over time.

The boundary conditions are defined based on various deformation schemes. The point displacement in the pure displacement algorithm is designed along a line interpolation curve between the two ends, which come from the preoperative and postoperative radiographic data about key points on each vertebra. The displacement is evenly divided into ten parts and gradually moves to the final equilibrium state. The force application scheme constructs a series of springs for which one end always points at the final balance position and also moves along a line interpolation curve. Its other end produces an elastic force on each vertebra and causes the whole trunk to move and deform to the equilibrium state.

The validation of algorithms is executed by implementing the deformation of some simple synthetic objects by using both our code and the ANSYS software, and by computing the distance error between the surfaces of two deformed results. The quantitative analysis is used as a reference to estimate the accuracy of our deformable model.

Finally, the analysis of error between the simulated result of our model and the patient's clinical data are computed to evaluate our model. The linear elasticity based on finite elements with pure displacement achieves the best simulation result, whose average distance error is only 10.2607 (mm) after averaging the distance error in two directions. Next best is the linear finite element force application. The order from best to worst is linear finite element pure displacement, linear finite element force application, and non-linear finite element force application.

The work carried out in the framework of this project showed that using the finite element method to simulate scoliotic surgery is feasible. But because the complexity of the human body leads to difficulty in constructing an accurate human trunk mesh, which should reflect all human organs and the relationship of connection between them, our model, which only includes vertebra, coarse ligaments and soft tissue, cannot achieve very high simulation accuracy. Consequently, a better simulation would require the development of clearer mesh definition and research on the biomechanical properties of human organs.

CONDENSÉ

Introduction

Le but ultime de ce projet de maîtrise est de développer un modèle d'éléments finis pour simuler l'effet d'une chirurgie correctrice de la scoliose sur la surface externe du tronc. Durant les cinq dernières années plusieurs modèles mathématiques complexes ont été étudiés et plusieurs données expérimentales ont été acquises afin de décrire les déformations biomécaniques du tronc humain.

Étant donné que chaque organe du tronc humain possède ses propriétés spécifiques, les modèles de simulation proposés ont été développés de façon spécifique à l'application d'intérêt et par conséquent les modèles physiques sous-jacents ont été configurés selon les besoins de l'application. Certains modèles biomécaniques basés sur les éléments finis ont été développés pour simuler le mécanisme de correction des déformations scoliotiques sous l'effet d'un traitement sur une géométrie spécifique de patients (Patwardan 1990, Wynarsky1991, Aubin 1993). Ces études ont montré comment une meilleure correction pourrait être obtenue mais le mécanisme biomécanique complexe de la déformation de la colonne sous l'effet d'un traitement n'est pas encore clairement documenté. Un des modèles biomécaniques qui a été développé pour la simulation de traitement de déformations scoliotiques est basé sur la géométrie personnalisée de la colonne vertébrale et de la cage thoracique obtenue par reconstruction 3D radiographique. (Aubin 1995). Ce modèle a été utilisé pour simuler le traitement par corset sur les structures osseuses du tronc. Même si ce modèle permet d'identifier les points de chargement qui peuvent entraîner une meilleure correction, ce modèle ne prend pas en considération l'action des tissus mous sous l'effet d'un chargement.

Ce projet de recherche vise à fournir à l'orthopédiste un outil qui lui permettra de simuler l'effet d'une chirurgie correctrice de la scoliose sur la surface externe du tronc. L'outil permettra ainsi de montrer au patient son apparence après la chirurgie selon les différentes stratégies possibles. Le patient pourra ainsi participer à la décision dans le choix de la stratégie.

Une première étape consiste à construire un modèle géométrique de l'ensemble des structures anatomiques du tronc. Celui-ci est obtenu à partir d'un recalage du modèle 3D des structures osseuses obtenu par reconstruction radiographique et la surface externe du tronc obtenue par des numériseurs 3D. Ensuite un maillage tétraédrique est généré entre la surface externe du tronc et la surface des structures osseuses du tronc. La deuxième étape consiste à développer un modèle d'éléments finis déformable du tronc, en associant des propriétés mécaniques aux différents éléments tétraédriques, afin d'évaluer l'effet d'une chirurgie correctrice de la scoliose sur la géométrie externe du tronc. Ce modèle physique sera en mesure de propager l'effet d'un chargement sur la colonne vertébrale sur les autres structures du tronc jusqu'à la surface externe du tronc. Le résultat sera comparé à la surface externe du tronc acquise avec les numériseurs 3D après la chirurgie afin de valider le modèle. Une fois validé, le modèle permettra la simulation de la géométrie externe du patient pour différentes stratégies opératoires. Par conséquent, le choix d'une stratégie optimale sera possible grâce à la visualisation 3D du résultat simulé.

État de l'art

Anatomie et propriétés biomécaniques de la colonne vertébrale

Le tronc humain est composé d'une structure osseuse complexe et de ligaments qui protègent les organes internes et qui sert de support aux structures externes. Le squelette est composé de trois parties : les vertèbres, la cage thoracique et le bassin. La colonne vertébrale, axe médial ostéo-articulaire du corps humain, assure trois types de fonctions biomécaniques principales (White 1990) : dynamique (transmission du chargement entre les parties inférieures et supérieures du corps), cinématique (permettant des mouvements physiques) et protectrice (de la moelle épinière). Ses vertèbres se composent de deux parties distinctes : un bloc osseux antérieur, appelé corps, et un anneau osseux postérieur appelé arc neural. Entre les vertèbres, le disque intervertébral transmet les forces de compression entre deux vertèbres. En plus des disques un ensemble de ligaments

permettent de lier deux vertèbres adjacentes. Le thorax qui est une zone cylindrique est composé de douze paires de cotes qui sont jointes par le sternum.

La scoliose

La scoliose est définie comme une déformation tridimensionnelle complexe de la colonne vertébrale sur le plan frontal qui implique des déformations au niveau des vertèbres, de la cage thoracique (entraînant une asymétrie appelée gibbosité) et du bassin. Dans la majorité des cas, la scoliose apparaît juste avant et à l'adolescence pendant la poussée de croissance. En général, la colonne et le squelette vont continuer à se déformer en l'absence de traitement. Lorsque la déformation est très sévère (angle de Cobb >40 degrés) et que la progression continue même si des traitements non chirurgicaux ont été effectués alors une chirurgie correctrice s'impose.

Techniques de modélisation

La méthode d'éléments finis tient compte des propriétés physiques des matériaux lors de la simulation de déformations. Cette approche décrit une forme à l'aide d'un ensemble d'éléments de base (triangles, quadrilatères, tétraèdres) et des fonctions de forme à support compact. Ce qui permet des représentations continues du matériau avec des niveaux variables de continuité. Un modèle d'éléments finis est complètement défini par le choix de ses éléments, ses fonctions de forme et une paramétrisation globale reliant les différents espaces de paramètres. Il a été largement utilisé pour calculer des déformations de tissus mous sous l'effet de contraintes mécaniques. Même si les modèles masse-ressort ont été développés dans le domaine du graphisme pour leur simplicité et leur implémentation performante les modèles d'éléments finis sont plus utilisés dans le domaine de biomécanique étant donné qu'ils sont sensés atteindre une meilleure précision dans la simulation des déformations.

Une fonction $\Phi(X,t)$ associe une configuration de référence à une configuration courante qui peut s'exprimer comme une addition du déplacement à la position originale dans la configuration de référence. La mesure fondamentale de déformation est décrite

par le gradient de déformation $\nabla\Phi = I + \nabla u$ (I étant la matrice identité). Nous avons choisi la propriété élastique de Cauchy pour simuler la déformation du matériau car la déformation dépend uniquement de la valeur courante du gradient de déformation et non de toute l'information temporelle du mouvement.

Étant donné le vecteur normal unitaire n de la surface, la force de traction spatiale $t(x,n)$ peut être exprimée comme une fonction de $\sigma(x)$: $t(x,n) = \sigma(x)n$ qui est exprimée dans le système Eulérien de la configuration de référence. On peut alors transformer la relation entre la pression et le gradient de déplacement dans le système lagrangien et obtenir ainsi le premier tenseur de pression de Piola-Kirchhoff :

$$\sigma(X) = \det(\nabla\Phi(X))\sigma(x)\left(\nabla\Phi(X)^t\right)^{-1},\ x = \Phi(X)$$

Comme le tenseur de pression n'est pas symétrique là ou le tenseur de Cauchy est symétrique une transformation du premier tenseur de Piola-Kirchhoff en le multipliant par $\nabla\Phi(X)^{-1}$ nous permet d'obtenir le second tenseur symétrique de Piola-Kirchhoff

$$S = \nabla\Phi(X)^{-1}\sigma(X)$$

Notre algorithme utilise un modèle d'éléments finis avec des éléments tétraédriques à quatre nœuds avec des fonctions de forme linéaires et suit la procédure d'éléments finis décrite ci-dessous.

(a) Diviser le milieu continu représentant le matériau en un nombre fini d'éléments. Dans chaque élément construire le champ de déformation par interpolation à partir de certains sommets en utilisant des fonctions de base qui décrivent pour chaque sommet comment les variables qu'il contient influencent la fonction continue de déformation du matériau.

(b) Pour chaque élément, exprimer la composante de l'équation d'équilibre en terme de fonctions d'interpolation et de déplacements des éléments noeuds.

(c) Résoudre le système complet comme un assemblage de ses éléments pour obtenir les déplacements des noeuds à travers tout l'objet modélisé.

Nous avons assemblé la matrice locale de rigidité de l'équation d'équilibre dans chaque tétraèdre dans une matrice de rigidité globale creuse. Les forces appliquées sur chaque

noeud P consistent en sa propre force d'inertie et la somme des forces provenant de noeuds adjacents dénotés par :

$$F_p^l = \sum_{T\in v(P_p)} F_p^l(T) = \sum_{T\in v(P_p)} \left(\left[B_T^{pp}\right]u_p + \sum_{\substack{j=0\\ j\neq p}}^{3} \left[B_T^{pj}\right]u_j \right) = \left[B_T^{pp}\right]u_p + \sum_{A\in v(P_p)}^{3} \left[B_T^{pj}\right]u_j$$

Où :

$T \in v(P_p)$: est la somme sur tous les tétraèdres appartenant au voisinage du sommet P_p.

Ces expressions définissent la relation entre la force appliquée sur un nœud et le déplacement des nœuds adjacents.

En général, cette loi d'élasticité linéaire n'est valide que pour les déplacements inférieurs à 10% de la taille totale du champ de déformation. Pour simuler de larges déformations, nous avons utilisé des éléments de Saint Venant-Kirchhoff, qui peuvent simuler des matériaux hyper-élastiques isotropiques. La formulation de sa fonction d'énergie potentielle est donnée par :

$$W = \frac{1}{2} E : C : E = \frac{1}{2} E_{ij} C_{ijkl} E_{kl}$$

En dérivant la fonction d'énergie, le second tenseur de Piola-Kirchhoff peut être représenté en fonction du tenseur de Cauchy-Green :

$$S = \frac{\partial W}{\partial E} = \lambda tr(E) I + 2\mu E$$

où λ et μ sont les constantes Lame qui sont reliées aux valeurs mécaniques décrivant les propriétés élastiques du matériau c.à.d. le module de Young E_y et le ratio de Poisson v par la relation :

$\lambda = \dfrac{vE_y}{(1+v)(1-2v)}$, $\mu = \dfrac{E_y}{2(1+v)}$. Le module de Young E caractérise la rigidité du matériau alors que le ratio de Poisson v représente son incompressibilité. Étant donné que la relation entre la pression et la tension est linéaire, ce matériau est physiquement linéaire. D'un autre coté la relation non linéaire entre E_y et ∇u exprime une non linéarité géométrique c.à.d. une élasticité avec de grand déplacements. Ces relations sont

utilisées pour représenter le comportement biomécanique d'un matériau élastique qui obéit à la loi de Saint Venant-Kirchhoff.

Une équation générale du mouvement est obtenue en rajoutant une composante d'amortissement. Cette équation est aussi appelée l'équation Lagrangienne.

$$\rho \frac{d^2u}{dt^2} + c\frac{du}{dt} = f(X) + \nabla \cdot \sigma(X), \qquad X \in \Omega$$
$$t(X) = \sigma(X)n \qquad X \in \Gamma_1$$

$$\text{où} \begin{cases} \rho : \text{densité massque} \\ c : \text{coeficient d'amortissent du matériau} \\ f : \text{ force externe volumique} \\ t : \text{ force externe surfacique} \end{cases}$$

Le modèle d'éléments finis peut finalement être discrétisé en un ensemble de vecteurs noeuds X . Pour un calcul statique, la relation pression-tension implique $f(X) + \nabla \cdot \sigma = 0$. L'énergie potentielle de déformation d'un matériau élastique peut être calculée à partir de son tenseur de déformation et des coefficients Lame. Ainsi, le tenseur de pression interne déduit à partir de l'énergie potentielle de déformation du volume et la pression exercée sur la surface externe constitue l'équation dynamique de mouvement décrivant la déformation d'un matériau élastique. Dans la plupart des méthodes d'intégration implicites nous avons choisi l'algorithme de Newmark. Pour résoudre le système algébrique non linéaire nous avons utilisé la méthode de Newton-Raphson combiné avec l'algorithme de recherche linéaire.

Méthodologie

Acquisition des données

Nous avons utilisé des caméras 3D de la compagnie InSpeck pour numériser la surface externe du tronc de patients scoliotiques. Ce système fournit en sortie un modèle géométrique 3D de la surface représentée à l'aide d'un ensemble de facettes triangulaires. Un modèle de la surface complète du tronc d'un patient est compose de 49,470 sommets et 98,401 triangles. Les images radiographiques postéro antérieur (PA0)

et latérale (LAT) des patients sont obtenues dans un système de positionnement qui comporte un objet de calibrage. Suite à la procédure de calibrage, des repères anatomiques sont identifiés sur les images de vertèbres et de côtes et appariés sur la paire de vues PA0 et LAT. Un modèle 3D personnalisé d'un ensemble de six points par vertèbre et un modèle filaire de la cage thoracique sont ainsi reconstruits par stéréo-radiographie. Enfin, un modèle surfacique plus complet est obtenu en déformant un dictionnaire de vertèbres de spécimens cadavériques obtenu par 'CT scans' en utilisant comme points de contrôle les repères anatomiques reconstruits. Un maillage tétraédrique a été ensuite généré en respectant la surface externe obtenue.

Modèle d'éléments finis du tronc

Pour simuler l'effet d'une chirurgie correctrice de la colonne vertébrale sur la surface externe du tronc on fait propager le résultat de la chirurgie sur la colonne jusqu'à la surface externe du tronc en déformant le maillage tétraédrique généré entre la surface externe du tronc et la surface des structures osseuses sous jacentes. Comme les forces appliquées sur la colonne lors d'une chirurgie ne sont pas connues on se sert des déplacements effectués sur un ensemble de repères anatomiques suite à une chirurgie. Ainsi, nous avons implémenté deux types de conditions aux frontières. Ces conditions aux frontières sont définies par la courbe de déplacement, l'amplitude de la force et sa direction. Elles sont déterminées en comparant la position d'un ensemble de repères anatomiques avant et après chirurgie et les valeurs intermédiaires sont obtenues par une méthode d'interpolation.

La configuration initiale du maillage a été d'abord prétraité afin d'éviter des éléments invalides. De même les déplacements ont été effectués de façon graduelle jusqu'à atteindre la position d'équilibre. Étant donné la position finale des points aux frontières, une force de traction sur chaque point doit être évaluée. Pour chaque force, on doit calculer dynamiquement son amplitude et sa direction à chaque incrément de temps. Une force ressort a été appliquée sur les points aux frontières.

Pour éviter les problèmes de divergence, tout comme les déplacements l'amplitude de la force est incrémentée graduellement. Nous avons utilisé l'algorithme d'intégration de Newmark qui est bien décrit dans l'annexe.

Pour résoudre l'équation d'équilibre pour des matériaux élastiques de nature non linéaire une méthode numérique robuste a été utilisée. La méthode de Newton a été utilisée pour minimiser la fonction d'énergie de déformation en approximant l'énergie totale W à l'aide de fonctions quadriques. Cependant, la méthode standard de Newton n'étant pas appropriée nous avons amélioré la stabilité numérique de notre méthode en calculant l'incrément de chargement de façon adaptative.

Pour effectuer une validation quantitative de l'approche proposée la déformation d'un objet synthétique a été simulée par notre méthode et le logiciel commercial ANSYS. Enfin, une évaluation du modèle proposé a été effectuée à partir de données réelles d'un patient. Les configurations préopératoires et postopératoires des structures osseuses ont été utilisées pour simuler la déformation appropriée sur la surface externe du tronc avant la chirurgie. Le résultat de la simulation est ensuite comparé à la surface externe réelle du tronc acquise après la chirurgie.

Résultats et discussion

Pour comparer les résultats des simulations dans différentes conditions d'implémentation nous avons calculé la distance bidirectionnelle entre la surface simulée et la surface réelle du tronc du patient acquise après la chirurgie. L'analyse de ces résultats a démontré que le modèle d'éléments finis basé sur une propriété d'élasticité linéaire avec des déplacements purs permet d'atteindre une meilleure précision de simulation. La distance moyenne est seulement de 10.2607 (mm). Le modèle basé sur un schéma linéaire d'application de force offre une moins bonne précision et enfin le modèle le moins intéressant est celui basé sur un schéma non linéaire d'application de force.

Le modèle non linéaire est probablement moins intéressant dans l'expérience que nous avons conduite car la déformation obtenue sur la surface externe du tronc suite à la chirurgie ne semble pas comporter une composante de rotation de grande amplitude.

La qualité du maillage que nous avons utilisé n'était pas adéquate. En effet, certains tétraèdres avaient une forme allongée et la taille des différents tétraèdres varie de façon importante. Cette variabilité affecte considérablement nos résultats puisque ça implique des matrices de rigidité mal conditionnées lorsque le volume de certains tétraèdres est presque nul.

Une génération d'un maillage précis intégrant les différentes structures anatomiques du tronc humain n'est toujours pas disponible; le maillage que nous avons utilisé a certainement besoin d'être raffiné afin de représenter les différentes structures anatomiques avec une meilleure résolution.

Conclusion et travaux futurs

Ce projet porte sur la simulation de l'effet d'une chirurgie correctrice de la colonne vertébrale sur la surface externe de patients scoliotiques. Nous avons utilisé le modèle d'éléments finis pour représenter les différentes structures anatomiques du tronc. Après avoir construit une équation différentielle dynamique pour décrire la procédure de déformation nous avons testé différentes méthodes de résolution du système d'équations non linéaires et nous avons considéré différentes propriétés de matériaux. Nous avons d'abord construit une structure déformable pour représenter le tronc à l'aide de plusieurs sortes de tissus avec des propriétés différentes. Ensuite nous avons considéré deux types de conditions aux frontières en se basant sur les modèles 3D préopératoire et postopératoire des structures osseuses d'un patient scoliotique. Enfin, nous avons implémenté la déformation dynamique pour des modèles élastiques linéaire et non linéaire et nous avons évalué quantitativement la différence entre la surface du tronc simulé et la surface réelle du tronc du patient acquise après la chirurgie.

Nous avons construit le modèle dynamique à partir du modèle statique. Après avoir acquis la relation statique entre les sommets de chaque élément et les forces internes et externes exercées sur lui nous avons rajouté deux composantes (l'accélération et la vitesse) et deux paramètres (la masse du matériau et l'amortissement) dans l'équation statique. Nous avons ainsi obtenu une équation dynamique qui permet de simuler les

mouvements successifs d'une déformation à l'aide d'une équation différentielle ordinaire d'ordre deux. Finalement, nous avons réussi à développer un solveur numérique stable qui combine différentes techniques numériques comme la méthode itérative de Newton, le chargement incrémental adaptatif et la recherche linéaire. Cependant, pour gérer la non linéarité d'un matériau qui obéit à la loi de Saint Venant-Kirchhoff la simulation doit être conduite de façon complète afin d'éviter des bifurcations et des problèmes de singularité de la matrice de rigidité.

Dans le futur, on devrait améliorer la qualité du maillage et utiliser des algorithmes automatiques pour prévenir les tétraèdres invalides afin d'améliorer la robustesse du modèle. Les mesures des propriétés mécaniques des organes devraient être effectuées in vivo afin de fournir des paramètres qui refléteraient mieux la réalité physique.

D'autre part, comme le modèle d'éléments finis non linéaire consomme des ressources considérables de calcul et de mémoire une parallélisation de l'algorithme serait d'une grande utilité. En effet, une meilleure précision devrait être atteinte puisque une meilleure résolution d'éléments finis pourra être considérée.

TABLE OF CONTENTS

ACKNOWLEDGEMENTS iv

RÉSUMÉ v

ABSTRACT ix

CONDENSÉ xii

TABLE OF CONTENTS xxii

LIST OF TABLES xxvi

LIST OF FIGURES xxvii

LIST OF APPENDIXES xxxi

LIST OF ABBREVIATIONS AND SYMBOLS xxxii

CHAPTER : 1 INTRODUCTION 1

CHAPTER : 2 STATE OF THE ART 5

2.1 Anatomy and biomechanics of spine 5

2.1.1 Anatomy of vertebrae 5

2.1.2 Intervertebral discs 7

2.1.3 Ligaments 9

2.1.4 Thoracic rib cage 12

2.1.5 Abdomen 13

2.1.6 Pelvis 15

2.2 Scoliosis 16

2.2.1 Idiopathic scoliosis 16

2.2.2 Deformation of vertebra 17

2.2.3 Clinical treatment 17

2.2.3.1 Observation and repeated examinations 18

2.2.3.2 Bracing treatment 19

2.2.3.3 Surgical treatment 19
2.3 Modeling techniques 23
2.3.1 Deformation of geometric surface 24
2.3.1.1 Free-form deformation 24
2.3.1.2 Deformations of space 25
2.3.1.3 Implicit surface 26
2.3.2 Mass-spring model 27
2.3.3 Finite element model 30
2.3.3.1 Finite element physical model 35
2.3.3.2 Linear model 39
2.3.3.3 Limits of the linear elastic model 42
2.3.3.4 Nonlinear finite element model 44
2.3.3.5 Hyperelastic material 45
2.3.3.6 Equilibrium equations 47
2.3.3.7 Solution of dynamic system 49
2.4 Choice of materials and mechanical properties 50
2.5 Objective 55
CHAPTER : 3 METHODOLOGY 57
3.1 Acquired data 57
3.1.1 External surface from InSpeck system 57
3.1.2 Internal surface 59
3.2 Finite element model of trunk 61
3.2.1 Derivation of boundary conditions 62
3.2.2 Derivation of displacement 65
3.2.3 Selection of displacement step 68
3.2.4 Application of force 69
3.3 Solution and construction of dynamic equation 72
3.3.1 Integration algorithm 73
3.3.2 Numerical methods for minimization 74

3.3.3 Adaptive time step 75
3.3.4 Selecting search direction and length 76
3.3.5 Linear system solution 78
3.4 Mechanical properties of tissue 79
3.5 Validation method 80
3.5.1 Metric of error 82
CHAPTER : 4 SIMULATION RESULTS 84
4.1 Introduction 84
4.2 Validation of model 85
4.2.1 Linear force application 86
4.2.2 Nonlinear force application 90
4.2.3 Conclusion 93
4.3 Patient's model 96
4.3.1 Patient's real surface after surgery 97
4.3.2 Patient's 3D model before surgery 97
4.3.3 Mesh quality analysis 99
4.4 Linear elastic model 101
4.4.1 Pure displacement 102
4.4.2 Distance error analysis 103
4.5 Linear application of force 105
4.5.1 Distance error analysis 107
4.5.2 Residual of spring distance 109
4.6 Non-linear application of force 110
4.6.1 Distance error analysis 112
4.6.2 Residual of spring distance 114
CHAPTER : 5 DISCUSSION 116
CHAPTER : 6 CONCLUSION AND FUTURE WORK 123
6.1 Conclusion 123

6.2 Future work 124

REFERENCES 128

APPENDIXES 145

LIST OF TABLES

Table 2.1: Primary spinal ligaments 11
Table 2.2: Adolescent idiopathic scoliosis treatment 18
Table 2.3: Comparison of mass-spring and finite element method 35
Table 2.4: Vertebral material properties used in the finite element model 52
Table 2.5: Material biomechanical parameters of rib cage and vertebra 53
Table 2.6: Mechanic properties of soft tissue used in the literature 54
Table 3.1: Deviation of key points 67
Table 3.2: Mechanical properties of trunk model 80
Table 3.3: Parameters of deformed beam 82
Table 4.1: Comparison of linear deflection simulation between ANSYS and our model 94
Table 4.2: Comparison of nonlinear deflection simulation between ANSYS and our model 95
Table 4.3: Comparison of maximal displacement of deflection simulation between theory and our model 96
Table 4.4: Tolerance error at final balance 110
Table 4.5: Tolerance error at final balance 115
Table 5.1: Analysis of simulation of three FEM 117
Table 5.2: Computation analysis 119

LIST OF FIGURES

Figure 2.1: Element of spine column (www.espine.com) 5
Figure 2.2: Anatomy of lumbar vertebra (taken from www.espine.com) 6
Figure 2.3: Lateral view of thoracic vertebra (White 1990) 6
Figure 2.4: Constitution of intervertebral disc (White 1990) 7
Figure 2.5: Compression of intervertebral disc (taken from www.mayfieldclinic.com/PE/PE-AnatSpine.htm) 8
Figure 2.6: Internal constraint (White 1990) 8
Figure 2.7: Main ligaments involved in thoracic spine (taken from www.spineuniverse.com) 9
Figure 2.8: Thoracic rib cage (taken from www.pdh-odp.co.uk) 12
Figure 2.9: One rib (taken from www.pdh-odp.co.uk) 12
Figure 2.10: Lateral view of abdominal muscles (taken from Basmajian 1977)..... 14
Figure 2.11: Posterior view of pelvis (taken from www.mgh.org)..... 15
Figure 2.12: Coxal bones (taken from nsd.k12.mi.us/nwhs/staff/departments/science) 15
Figure 2.13: Deformed vertebra (Aubin 1997) 17
Figure 2.14: Scoliosis progression over several years (Stagnara 1988) 18
Figure 2.15: Example of instrumentation CD (Lonstein 1995) 20
Figure 2.16: Four control points, their defined curve of Bézier and tangents at the beginning and end of the control polygon. 25
Figure 2.17: Deformation of space illustrated on a model of the giraffe: the original grid (a) and the deformed one obtained after a local deformation (b)..... 25
Figure 2.18: Undeformed (initial) and deformed (current configuration) of a body 36
Figure 2.19: Components of the deformation of a cubic (Picinbono 2001) 37
Figure 2.20: Finite element of tetrahedron type..... 41
Figure 2.21: Deformations of a linear elastic cylinder (a) original (b) linear elasticity and (c) nonlinear elasticity 43

Figure 2.22: Transformation relationship between parameters (Picinbono 2001)..... 49
Figure 3.1: InSpeck Digitizer with four cameras 58
Figure 3.2: Patient's external surface reconstructed by InSpeck..... 58
Figure 3.3: Acquisition of X-ray image 59
Figure 3.4: Deformable personalized rib cage 60
Figure 3.5: Points on preoperative and postoperative vertebrae 63
Figure 3.6: A vertebra defined by six points..... 63
Figure 3.7: Rib cage and points of radiograph..... 64
Figure 3.8: Spatial points (red) are mapped to vertices (blue) of mesh 65
Figure 3.9: Definition of displacement 66
Figure 3.10: Evaluation of displacement 66
Figure 3.11: Trail of displacement of vertices of mesh and relevant points..... 67
Figure 3.12: Histogram of deviation of key points 67
Figure 3.13: Displacement function..... 68
Figure 3.14: (a) Normal tetrahedron (b) Reversed (illegal) tetrahedron..... 69
Figure 3.15: Construction of spring force..... 71
Figure 3.16: Spring moving configuration..... 72
Figure 3.17: Algorithm of Newmark implicit integration (Belytschko 2000, p. 324).. 74
Figure 3.18: Algorithm of nonlinear system solver 78
Figure 3.19: Straight cantilever beam problem sketch 82
Figure 4.1: Hexahedral mesh produced by ANSYS 85
Figure 4.2: Error distribution of undeformed model (a) Distance from our model to ANSYS deformed surface. (b) Distance form ANSYS deformed surface to our model 86
Figure 4.3: Error distribution and its histogram of X-axis deflection (a) Distance from our model to ANSYS deformed surface. (b) Distance from ANSYS deformed surface to our model..... 87

Figure 4.4: Error distribution and its histogram of Y-axis deflection (a) Distance from our model to ANSYS deformed surface. (b) Distance from ANSYS deformed surface to our model 88
Figure 4.5: Error distribution and its histogram of Z-axis deflection (a) Distance from our model to ANSYS deformed surface. (b) Distance from ANSYS deformed surface to our model 89
Figure 4.6: Error distribution and its histogram of X-axis deflection (a) Distance from our model to ANSYS deformed surface. (b) Distance from ANSYS deformed surface to our model 91
Figure 4.7: Error distribution and its histogram of Y-axis deflection (a) Distance from our model to ANSYS deformed surface. (b) Distance from ANSYS deformed surface to our model 92
Figure 4.8: Error distribution and its histogram of Z-axis deflection (a) Distance from our model to ANSYS deformed surface. (b) Distance from ANSYS deformed surface to our model 93
Figure 4.9: Rigid registration 97
Figure 4.10: Patient's 3D mesh model (a) Surface (b) Rib cage (c) Ligament 98
Figure 4.11: Distribution of mesh volume 100
Figure 4.12: Mesh quality analysis 101
Figure 4.13: Distribution of principal stresses on surface 102
Figure 4.14: Distribution of principal stresses on vertebrae 102
Figure 4.15: Distance distribution of the front error from deformed to reference model 103
Figure 4.16: Distance distribution of back from the deformed to reference model 104
Figure 4.17: Distance distribution of error from reference to deformed model 104
Figure 4.18: Histogram of error distance (blue on surface of our simulation, red on surface of reference) 105
Figure 4.19: Distribution of principal stresses on surface 106
Figure 4.20: Distribution of principal stresses on vertebrae 107

Figure 4.21: Distance distribution of front error from deformed to reference model. 108
Figure 4.22: Distance distribution of back from deformed to reference model..... 108
Figure 4.23: Distance distribution of error from reference to deformed model 108
Figure 4.24: Histogram of error distance (blue on surface of our simulation, red on surface of reference) 109
Figure 4.25: Histogram of tolerance error 110
Figure 4.26: Distribution of principal stresses on surface 111
Figure 4.27: Distribution of principal stresses on vertebrae 111
Figure 4.28: Distance distribution of front error from deformed to reference model. 113
Figure 4.29: Distance distribution of back from deformed to reference model..... 113
Figure 4.30: Distance distribution of error from reference to deformed model 113
Figure 4.31: Histogram of error distance (blue on surface of our simulation, red on surface of reference) 114
Figure 4.32: Histogram of tolerance error 115

LIST OF APPENDIXES

APPENDIX A: FORMULATION OF DYNAMIC EQUATION 145

LIST OF ABBREVIATIONS AND SYMBOLS

FE	Finite Element
FEM	Finite Element Method
PDE	Partial Differential Equation
3D	Three-dimension
$:$ as in $A:B$	Double contraction of inner indices: $A:B$ is given by $A_{ij}:B_{ij}$; if A or B is symmetric $A_{ij}:B_{ji}$
$\otimes$	As in $a \otimes b$ indicates vector product; in indicial notation, $a \otimes b \rightarrow a_i b_j$
F, F_{ij}	Deformation gradient, $F_{ij} = \dfrac{\partial x_i}{\partial X_j}$
C	Cauchy Green tensor, $C = F^T \cdot F$
E, E_{ij}	Green strain tensor, $E = \frac{1}{2}\left(F^T \cdot F - 1\right)$

CHAPTER : 1 INTRODUCTION

Biomechanics has studied complex mathematical models and produced a large amount of experimental data for representing the deformation of the human trunk. Computer graphics has proposed many algorithms for the fast computation of deformable bodies, but often at the cost of ignoring physics principles. During the past five years, there has been growing interest in the medical and computer science field, in the simulation of medical procedures. Under the terminology "medical virtual reality" proposed by Satava (Satava 1996), the first generation of medical simulators applied the concept of navigation and immersion to three-dimensional anatomical datasets. Most of today's medical simulation systems have a tendency to represent physical phenomena and, more specifically the realistic modeling of tissue. This will not only improve current medical simulation systems, but will considerably enlarge the set of applications and the credibility of medical simulation such as virtual surgery simulation, which requires the combination of many disciplines.

Since each organ of the human trunk is special, present medical simulations are proposed within their special medical research field and the physical models are constructed according to different requirements. Cotin (Cotin 1997) proposes a real-time simulator to represent the deformation of the liver by using the linear finite element method. But for most materials, the linear elastic model is only valid for small displacements. For large displacements, more complex non-linear models have been introduced, such as the Mooney-Rivlin model (Bro-Nielsen 1995, Sagar 1994) or the Saint Venant Kirchhoff (Terzopoulos 1988, Bro-Nielsen 1995, Kaiss 1996) where the stress/strain relationships are no longer linear. Additional physical constraints may be considered, such as incompressibility. Picinbono (Picinbono 2001) introduces a nonlinear finite element model to improve the accuracy of liver simulation.

Some finite element biomechanical models applied to the treatment of scoliosis were developed to simulate the mechanism of spinal deformation on a typical geometry of a scoliotic patient (Patwardan 1990, Wynarsky1991, Aubin 1993). These studies showed

how a better correction could be obtained, but the mechanically complex spinal action was still not described clearly. In them, certain simulation models are used to study the mechanism of brace treatment of scoliosis and seek more effective treatment of the brace. One of them is a biomechanical finite element model for scoliotic deformities which has been developed on a personalized finite element model of the scoliotic rib cage (Aubin 1995). This model of spine and rib cage was constructed very accurately from medical data, and contains about 3000 elements representing the osseo-ligamentous components of the trunk. The parameters of the model come from in-vitro morphometric measures and were validated by the comparison with the deformation of various orthopedic treatments. The pressure from the brace is converted into nodal forces to be exerted on the finite element model. The simulations apply loads laterally on the convex side and on the anterior thorax opposite to the rib hump, with a system that mechanically constrains the posterior rib hump to move backward. It was used to simulate deformation in fifteen scoliotic adolescents presenting thoracic curves (Cobb: 22°-36°) treated by the Boston brace.

Although the model of spine and brace is a very exciting breakthrough in predicting the spine deformation under loads, this work does not consider the influence of the soft tissue which exists around the bones and spine. Since the human trunk is mainly made up of soft tissue, the medical consequences of soft tissue modeling are very important. Soft tissue modeling, i.e., the modeling of soft tissue mechanics and deformation, has been identified as a key technology for the development of advanced medical simulation (RCAMI 1996). To achieve such advanced simulations, it is essential to model the phenomena occurring at the geometrical, physical and physiological levels. Although the 3D recovery technology of anatomical structures from medical images is relatively mature, a lot of research effort is still needed for the physical modeling of human tissue. This kind of model should contain not only the skeletal factors, but also some soft organs which are very important to predict the form of the final deformed skeleton and the external surface of the trunk, which is the primary concern of the patient.

This research project is interested in the problems encountered by orthopedists who correct the deformations of the scoliotic trunk by surgery. The results of simulation can predict the postoperative external surface of the trunk model, and allow the scoliotic patient to receive optimal treatment by the design of personalized surgery. Doctors can also get some information about the effect of treatment and the patient can see her postoperative trunk shape before surgery.

To create the geometric description of the human trunk, we first acquire a set of discrete data which produces an integral 3D human trunk model. It is difficult to analytically handle the discrete data as a 2-D entity. So, in our project, we choose a volume expression method to approximate the 3D model. Because in space the tetrahedron is the simplest geometric element, yet sufficient when combined with other tetrahedra to form any complex shape, we choose it as our geometric description of each finite element. Although we construct a human trunk, the deformation of the trunk is not only decided by the interaction between it and exterior forces, but also by the many other factors that constrain its final shape, such as muscle and skeletal structure, which play an important role in human trunk activities. Our model is reconstructed based on knowledge of anatomy and biomechanics, which provide us a great deal of valuable information to construct human model. Based on these theories, we will finally create an integral trunk model consisting of many connected organs.

A finite element model of the deformable musculo-skeletal system is developed to evaluate the scoliotic patient's external shape after the spinal surgery. This mathematical geometric model will be capable of analyzing external shape in response to surgical loading and will be validated from the patient's postoperative external surface. The model can allow the simulation of the external surface of the trunk according to the variation of orthotic design parameters. Further, the model will be based on estimates of the mechanical properties of human tissue, although no active neuromuscular involvement is considered. Finally, the results of this analysis can provide a biomechanical rationale for clinical observations regarding the external outcome of surgical treatment for scoliosis.

The remainder of the thesis is organized as follows:

Chapter 2 —STATE OF THE ART. First we review the state of art of the anatomy of the spine and describe the main biomechanics of some organs of the human trunk. Second, we discuss the vertebral deformity of a scoliotic patient and clinical treatment. Third, we review some current modeling techniques and describe the finite element method that we use. Finally, to obtain accurate biomechanical properties of human tissues, we examine some publications and models that contain some relevant data. Then we describe our research objectives in the last section.

Chapter 3—METHODOLOGY. In section 1, we describe the clinical external and internal mesh models of one scoliotic patient. In sections 2 and 3, we design and implement the boundary conditions on the patient's finite element model to deform the patient's vertebra, and solve a dynamic equation to acquire patient's postoperative external surface. In sections 4 and 5, we define the biomechanical properties of different tissues and validate our model with the definition of a metric.

Chapter 4—SIMULATION RESULTS. In this chapter, we present our validation and simulation results.

Chapter 5—DISCUSSION. Our experimental results and some issues occurring in the experiments are analyzed in this chapter.

Chapter 6—CONCLUSION AND FUTURE WORK.

CHAPTER : 2 STATE OF THE ART

2.1 Anatomy and biomechanics of spine

The human trunk consists of a complex structure of bones and ligaments which protects the internal organs and sustains the external membranes. Its skeleton comprises three parts: vertebrae, rib cage and pelvis.

2.1.1 Anatomy of vertebrae

The spinal column, the medial osteo-articular axis of the human body, performs three principal biomechanical functions (White 1990): dynamic (transmission of load between upper and lower parts of body), cinematic (permitting physical motion) and protective (medullar cordon). It consists of multi-articulate connection of from 32 to 34 vertebrae which can be divided into five parts based on geometry: cervix (C1 to C7), thorax (T1 to T12), lumbar (L1 to L5), sacrum (S1 to S5 fused together) and coccyx (3 to 5 all fused together). From the front side, the healthy spine is rectilinear and symmetric but in the sagittal plane, the vertebral column forms four curves, anterior convex for cervical and lumbar region and posterior convex for the sacrum and thorax. In general, the natural posture increases the flexibility and capability of absorption of shock and maintains the rigidity and stability of the spinal column.

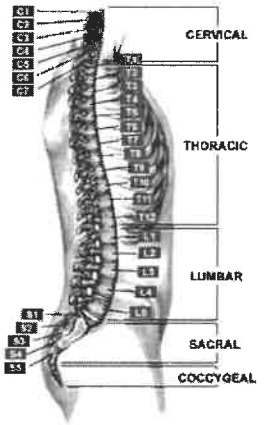

Figure 2.1: Element of spine column (www.espine.com)

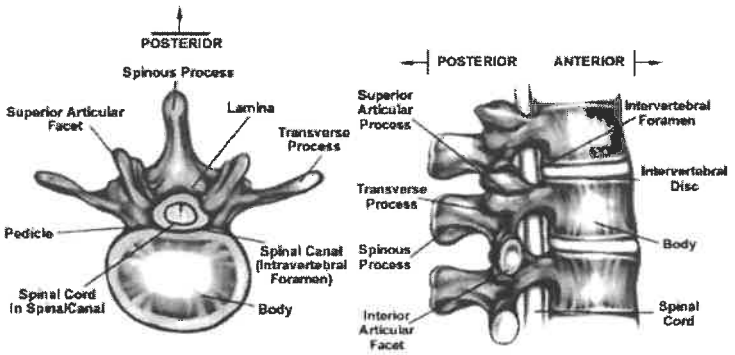

Figure 2.2: Anatomy of lumbar vertebra (taken from www.espine.com)

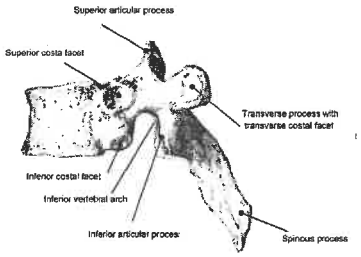

Figure 2.3: Lateral view of thoracic vertebra (White 1990)

A vertebra is composed of two distinct parts (figure 2.2, 2.3): an anterior osseous block called the body, and a posterior osseous ring or neural arch.

The cortical structure of the vertebral body encloses the sponge bone cell: the inferior and superior facets are concave and represent the vertebral plateaus. The intervertebral discs transmit the forces of compression between two vertebrae and the existence of the nucleus assures the mechanical properties of vertebral plateaus.

The neural arch, formed by cortical bones, has two pedicles and two laminas: the marrow is protected by the medullar canal. Four articular facets are situated on the articular apophysis (two superior and two inferior). Their orientation, which goes from the three great parts (cervical, thoracic and lumbar), defines the possible motion of the spinal column. The articular facets especially affect rigidity with vertebral torsion, which augments between T7-T8 (thoracic seventh and eighth vertebrae) and L3-L4 (third and forth vertebrae) with a peak between T12-L1. The costo-vertebral and costo-transversal facets, which are supported by transversal apophysis, connect with the ribs. A number of

ligaments and muscles also join transversal apophysis to which the other end, the thorny apophysis, joins two laminas. The vertebral mass continuously increases between the first cervical and the fifth lumbar vertebra, which allows the mechanical adaptability of the forces applied on each vertebra.

2.1.2 Intervertebral discs

When submitted to forces and moments, the intervertebral discs represent 20-30% of the length of the whole spine. The anisotropic disc is composed of three parts: the central portion with a gelatin-like consistency named "nucleus pulposus" and a fibrous fold to hold it tightly in place, called "annulus fibrosis" or “fibrous ring" as shown in the following figure. The annulus is attached to the center of the cartilaginous plateau and to the osseous vertebral body around it.

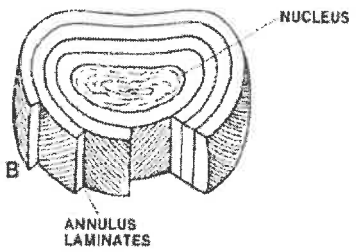

Figure 2.4: Constitution of intervertebral disc (White 1990)

Under compression, pressure appears at the center of nucleus and drives away the adjacent structure (see figure below). Without the internal pressure, the compression acting on the vertebra is concentrated on the periphery of the adjacent plateau and can cause the rupture of vertebral body.

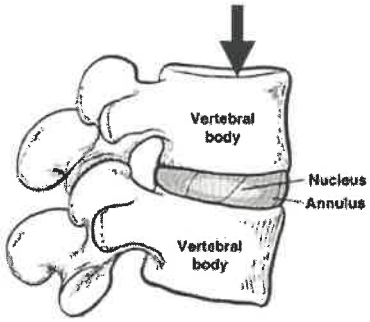

Figure 2.5: Compression of intervertebral disc (taken from www.mayfieldclinic.com/PE/PE-AnatSpine.htm)

The discs are submitted to tension forces in the physiologic motion of frontal and sagittal flexion. The shearing constraint comes from the axial rotation of the trunk relative to the pelvis. When a person is in normal position, the discs are submitted to compressive forces equal to three times the weight on them, while in dynamic charge, the forces are double.

The loading forces are of two distinct types: short and intense application or small amplitude during a long period. Also, the properties of the discs vary over time due to wear. So, they could irremediably degenerate under the action of much constraint, or break because of wear.

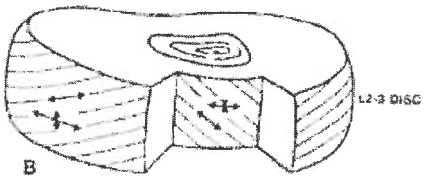

Figure 2.6: Internal constraint (White 1990)

The constraint reaction on the annulus is more complex (figure 2.6). Its exterior layer supports the constraint of tension in the tangent direction and in the fibrous direction. For the interior layer, the layout is the same with less amplitude and the axial tension forces are replaced by compression forces.

Under tension load, the shearing constraint (perpendicular to the fiber) is much increased and cannot be canceled by the annular structure, so that the risk of rupture is higher with tension force than with compression.

The flexion causes traction of the convex side of the vertebra, and compression of the concave side, and the intervetebral discs support the tension and compression. The effect of the flexion moment exerted on the discs produces two obvious states, as mentioned above.

The shearing constraint causes the load of torsion in the axial as well as the horizontal plane, and the magnitude depends on the distance to the axis of the applied constraint. If the fibrous orientation is consistent with the constraint normal, the shearing load may cause rupture of the intervertebral disc.

2.1.3 Ligaments

In addition to the intervertebral discs joining the centra and the synovial joints between the facets, a series of ligaments bind together adjacent vertebrae. The spinous processes are connected by interspinous ligaments and the arches have thin elastic sheets between them. These interarculate ligaments are called ligamenta flava (yellow ligaments). Running along the tips of the spinous processes is the superspinous ligament. Caudally it is continued morphologically and functionally with and by the coalesced tendons of vertebral muscles and thoracolumbar fascia. Even this fibrous tissue is very weak or entirely absent between the spinous processes of the last lumbar and the sacral vertebrae.

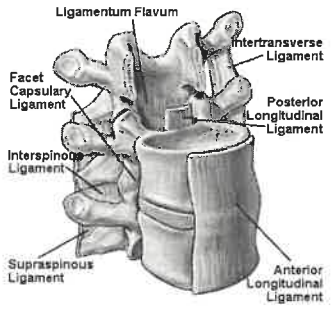

Figure 2.7: Main ligaments involved in thoracic spine (taken from www.spineuniverse.com)

Three of the more important ligaments in the spine are the ligamentum flavum, anterior longitudinal ligament and the Posterior Longitudinal Ligament (figure 2.7). The following table lists all ligaments around the spine and their limits (Bridwell 2004).

The Ligamentum Flava forms a cover over the dura mater, a layer of tissue that protects the spinal cord. This ligament connects under the facet joints to create a small curtain over the posterior openings between the vertebrae. The ligaments retain a certain tension when the column is in neutral position so that some compression is introduced to increase spinal stability. They possess a larger proportion of elastic fiber which permits support of large loads without deformation and minimizes the chance of pinch of spinous marrow between two adjacent osseous structures when an abrupt variation is introduced.

The Anterior Longitudinal Ligament attaches to the front (anterior) of each vertebra. This ligament runs up and down the spine (vertical or longitudinal).

The Posterior Longitudinal Ligament runs up and down behind (posterior) the spine and inside the spinal canal (Bridwell 2004).

The biomechanical properties of Longitudinal Ligaments are similar to those of the ligament flavum and some pre-constraint exists in them. Its value is ten times smaller than that of yellow ligament.

Besides the intervertebral ligaments, thoracic vertebrae have ribs associated with them. The heads of the ribs articulate with vertebral bodies, and the tubercles of the ribs articulate with transverse processes. The head of the first rib fits snugly into a depression formed by the costal fovea on the caudal edge of the last cervical vertebra, the edge of the intervertebral disc, and the costal fovea on the cranial edge of the first thoracic vertebra. Local ligaments hold the head of the rib closely to the vertebrae.

The head of the second rib fits into corresponding fovea between the first and second thoracic vertebrae. In addition to local ligaments similar to those of the first rib, a strong intercapital ligament (also called the conjugal ligament) runs dorsal to the intervertebral disc between the heads of the second ribs. A similar arrangement is found on subsequent ribs except the most caudal ones. (These articulate with the centrum of only one vertebra and not at the intervertebral space.)

Each intercapital ligament running over an intervertebral disc also has cranial and caudal branches as it leaves the rib head. These attach to the dorsal surfaces of corresponding adjacent vertebrae. The intercapital ligaments do not cause an elevation in the floor of the vertebral canal. They arise developmentally from the same tissue as the intervertebral discs and take the place of part of that structure.

Table 2.1: Primary spinal ligaments

Ligament	Spinal Region	Limits
Alar	Axis–skull	Head rotation & lateral flexion
Anterior Atlantoaxial	Axis & Atlas	Extension
Posterior Atlantoaxial	Axis & Atlas	Flexion
Ligamentum Nuchae	Cervical	Flexion
Anterior Longitudinal	Axis–Sacrum	Extension & reinforces front of annulus fibrosis
Posterior Longitudinal	Axis–Sacrum	Flexion & reinforces back of annulus fibrosis
Ligamentum Flavum	Axis–Sacrum	Flexion
Supraspinous	Thoracic & Lumbar	Flexion
Interspinous	Lumbar	Flexion
Intertransverse	Lumbar	Lateral flexion
Iliolumbar	Sacroiliac joints	Stability & some motion
Sacroiliac	Sacroiliac joints	Stability & some motion
Sacrospinous	Sacroiliac joints	Stability & some motion
Sacrotuberous	Sacroiliac joints	Stability & some motion

2.1.4 Thoracic rib cage

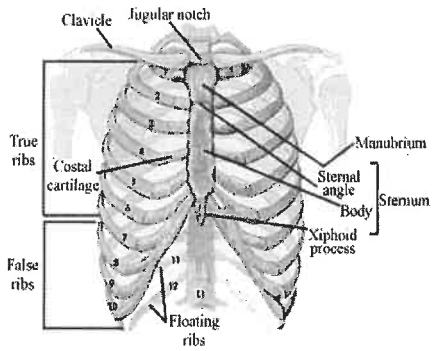

Figure 2.8: Thoracic rib cage (taken from www.pdh-odp.co.uk)

The thoracic rib cage (figure 2.8) shelters the vital organs of the human body and protects the spine from front and lateral impact: The frontal rigidity against load is bigger than the posterior. In the motion of flexion, extension, lateral flexion and torsion, the thoracic cage carries two and a half times rigidity which can be measured only in the ligamental presence. Under compression, the spinal rigidity has only a quarter of the value without rib cage; under traction, the thorax increases the axial rigidity by 40% and the normal column has two and a half times more rigidity than the scoliotic column. The osseous and cartilaginous structure of the thoracic cage joins together to absorb the energy of stress.

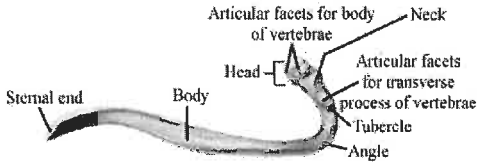

Figure 2.9: One rib (taken from www.pdh-odp.co.uk)

The thorax, a closed cylindric cave, is composed of twelve pairs of ribs which are divided into three categories and close on the sternum. The first seven ribs are respectively attached on the sternum by the cartilaginous joints. The next three are fused at the junction with the cartilage of the sternum. The last two float but support the

abdominal muscles. The space and position of thoracic cage relative to the spinal column increase the inert moment for the loading of the torsion or flexion. Moreover, the thoracic cage can rigidify the vertebral column through the costo-vertebral and costo-transversal joints with many ligaments: the costo-vertebral articulation joins the costal head at the sub-adjacent and upper-adjacent vertebrae through ligaments of the costal facet (superior and inferior costal articular facets). The costal facets of transversal apophysis support the three ligaments attached at costal tuberosity (costo-transversal joints). The synovial joints (articular capsule) connect the rib heads with intervertebral discs.

Rotation only occurs in certain loadings, because of the geometric curve of rib. The connection between ribs reduces the flexibility relative to each costal element (25 mm of deformation/10N) and produces the accompanying displacement (a superior loading produces a superior displacement and medial and posterior displacement).

Rigidity of the lateral costo-vertebral joint is high, especially in the medial ribs. The joints appear less rigid in superior or interior loading but the behaviors are completely contrary to the sterno-costal joint.

2.1.5 Abdomen

The interior abdominal wall is composed of muscles which protect the internal organs (Figure 2.10). The contraction of rectus abdominis, internal external obliques and transversus abdominis involves the variation of pressure in the abdomen: peritoneal liquid and viscera have a closed and deformable volume. The volume change of the thoracic cage is accompanied by a volume change of the abdominal cavity (Deschamps et al. 1988).

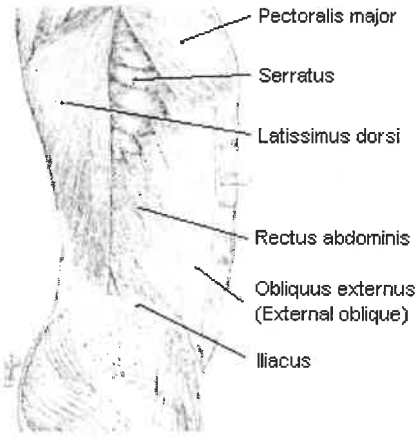

Figure 2.10: Lateral view of abdominal muscles (taken from Basmajian 1977)

Muscles exist between two layers of adipose and their disposition can be seen from outside or inside. The compressible part in the abdomen allows the load transfer between the abdominal external wall and the lumbar part of vertebral column. The abdomen appears as an oval ball on the quasi-vertical points, and it is surrounded by an elastic membrane and connected to the thoracic cage and the vertebral column.

The rectus abdominis descends from each rib at the medial line and sternum to the anterior part of the pubis. The external oblique begins from the costal edge of the eighth back rib and inserts on the anterior middle of the iliac crest until the pubis. The internal oblique is attached on the costal cartilage of the four back ribs and the pubis, and occupies the space surrounded by the rectus abdominis and the external oblique. The transversus abdominis joins the abdomen at its periphery. Its strong contraction during expiration increases the abdominal pressure and pushes the diaphragm up. It inserts at the level of the lumbar vertebra and the iliac crest and overlaps with the costal origin of diaphragm.

2.1.6 Pelvis

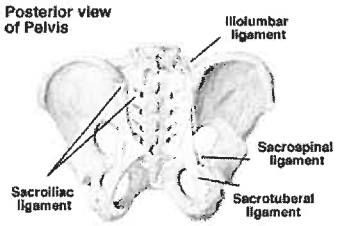

Figure 2.11: Posterior view of pelvis (taken from www.mgh.org)

The pelvis (figure 2:11) is divided into three parts: hip bone, sacrum and coccyx, while the pubic symphysis joins the hip bone together.

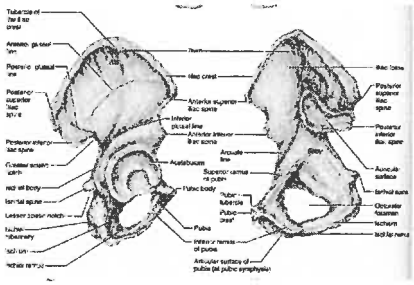

Figure 2.12: Coxal bones (taken from nsd.k12.mi.us/nwhs/staff/departments/science)

The hip bone or coxal bone (figure 2.12) holds the hemispheric cavity (acetabulum) and joins the crest of the femur. It consists of three joint bones: ilium, pubis and ischium; and the pubis is combined at the level of the cotyloid cavity. The iliac bone protects the low part of the abdomen and the iliac crest, the thick contour on the upper border, and supports the muscles. Sacro-iliac articulation constitutes the union of two bones and realizes the transfer of body weight, and the solid ligaments limit the relative motion. In fact, the weight is transferred to the superior end of the sacrum so that its inferior end and coccyx rise.

Five vertebrae are united by four intervertebral ossified bodies to form the sacrum, which is joined to the fifth lumbar vertebra through one thick disc. The sacral wings form the lateral part of the first sacral vertebra. The coccyx, four atrophic joint vertebrae, extends

the sacrum through cartilaginous articulation. A woman's pelvis is more spacious than a man's: the hip bones are more separated, the sacrum is larger and less curvy, the pubic branch is longer and the distance between the ischial tuberositys is longer.

2.2 Scoliosis

This section discusses some concepts about idiopathic scoliosis, which is our main experimental object, and the origin of our data. The main characteristics of this disease appear geometrically in the déformation of trunk.

2.2.1 Idiopathic scoliosis

Scoliosis is defined as three-dimensional deformation of the spine in the coronal (front view) plane which implies the deformation of the vertebrae of the thoracic cage (an asymmetry called gibbosity) and the pelvis (Senet 1984, Deacon 1987, Stokes 1987). It occurs in approximately 2% of women and in less than 0.5% of men, and usually starts in the early teens or pre-teens and may gradually progress as rapid growth occurs. Idiopathic scoliosis should also be conceptualized as a three dimensional deformity, however; twisting of the spine is coupled with curvature producing deformity in both coronal and sagittal (side view) planes. Idiopathic scoliosis (without evident cause) is more usual (i.e. 85% to 90% cases) and mainly appears in the course of growing up. The exact etiology of idiopathic scoliosis is not yet determined, but it is thought to be due to multiple factors. Although the exact genetics is unclear, the observation that idiopathic scoliosis is more common within families suggests the presence of an inherited trait. A number of hypotheses about its pathogenesis can be found: hereditary trait (Machida 1999), asymmetry of muscular force (Bagnall 2000, Burwell 2000, Roaf 1966), asymmetric growth of vertebrae (Burwell 1992, Roaf 1966) or ribs (Sevastik 1997) and hormonal origins. The pathomechanics of scoliosis also evokes many hypotheses, but like its origin, the difference between the cause, and its result of the rupture of spinal equilibrium, is difficult to specify.

2.2.2 Deformation of vertebra

Besides the global spinal deformation, scoliosis also causes the local deformation of vertebral geometry. The cuneiform deformation (figure 2.13) of the vertebral body on the apical zone promotes the process of scoliotic deformation (Burwell 1992). The neural arch makes an important morphological adaptation to react to the enforced dissymmetric loading by atrophy of the concave side (under pressure) and hypertrophy of the convex side. Finally, the pedicles and apophysis are orientated towards the concave side of curve (Perdrioller 1979).

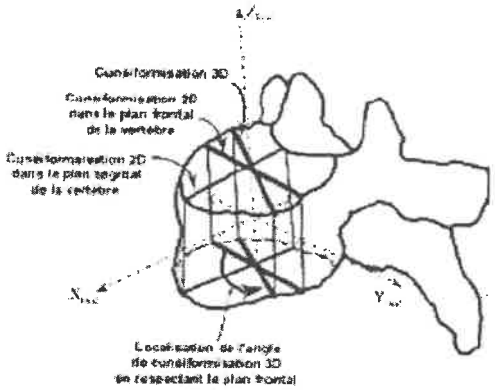

Figure 2.13: Deformed vertebra (Aubin 1997)

2.2.3 Clinical treatment

Although most scoliosis is of unknown cause, there does appear to be a developmental connection in many cases. Most cases of scoliosis occur just before and during adolescence, when children are going through a growth spurt. The progression continues at a slowed rate of about 0.4° per year (Ascani 1986) after skeletal maturity, increasing if the patient has a Cobb angle greater than 50° or a highly rotated curve apex (Weinstein 1981, 1983). In general, the higher the curve apex location is, the greater the expected curve progression (Ascani 1986, Peterson 1995, Weinstein 1981). Usually, the spine and skeleton would continue deforming with time without suitable treatment. Figure 2.14 shows the progression of spinal deformation of scoliotic patient with time.

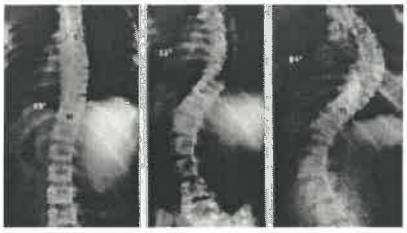

Figure 2.14: Scoliosis progression over several years (Stagnara 1988)

Treatment choice in adolescent idiopathic scoliosis is determined by a complex process which includes consideration of the patient's physiologic (not chronologic) maturity, curve magnitude and location, and potential for progression. The goal of treatment is to stop the progression of the curve and prevent deformity. The following table gives a basic reference for which treatment the patient should take according to his spinal curve.

Table 2.2: Adolescent idiopathic scoliosis treatment

Curve (degrees)	Treatment
<20°	Observation
>20° < 25°	4 month x-rays
25°-30°, 5° documented progression	Brace
30°-40°	Brace
>40°	Consider surgery

2.2.3.1 Observation and repeated examinations

Small curves measuring less than 20-25 degrees that do not require brace treatment should be observed during periodic examinations of four to six months or 1 year intervals based on their size. Observation remains a form of treatment because any 5 degree increase in the size of the curve may change the course of treatment.

2.2.3.2 Bracing treatment

Bracing may be used when the curve measures between 25 to 40 degrees on an X-ray, and during skeletal growth. The type of brace and the amount of time spent in the brace will depend on the severity of the condition. It is a form of nonoperational treatment to prevent scoliosis progression. Several types of braces have been developed with an aim to apply the correct forces at strategic places on the trunk. Its treatment is adopted to prevent further deformation of the spine and trunk. Bracing has been shown to be an effective method to prevent curves from getting worse. Meantime, some radiographic techniques make it possible to follow the evolution of curves and to validate or dispute the use of brace equipment in the treatment of scoliotic deformations. But biomechanics of orthotic treatments is a relatively new field and traditionally the treatment is based on the empiricism and the expertise of doctor.

2.2.3.3 Surgical treatment

Non-surgical treatments are usually prescribed when the Cobb angle scoliotic deformity is less than 40 degree). When the deformity is very severe (Cobb angle>40 degrees) and keeps progressing and other non-surgical treatments are invalid, a surgical correction is required (Bradford 1987). The popular technique is the fusion of some vertebral levels to hold the correction until the spine is solid (approximately one year). The surgical principal objectives are:

1. reducing the deformity (straighten the spine as much as possible),
2. assuring the maintenance of operating segmentation so as to fuse the spine bone,
3. stopping the progression of the deformity,
4. protecting the nerves and spinal cord from further damage,
5. improving the patient's appearance.

When corrective surgery of scoliosis is undertaken, two types of approaches can be chosen: anterior and posterior. For idiopathic scoliosis, the posterior approach (posterior exposure of vertebral column) is more frequently adopted. The principal types of posterior instrumentation are: Harrington, Luque, CD (Cotrel-Dubosset), TSRH (Texas

Scottish Rite Hospital) and Colorado. The correction of spinal curve can also be gotten by the combination of the mechanical behaviors of vertebrae when the objects (screws and hooks) connected with metal stalk are implanted, as the following figure shows:

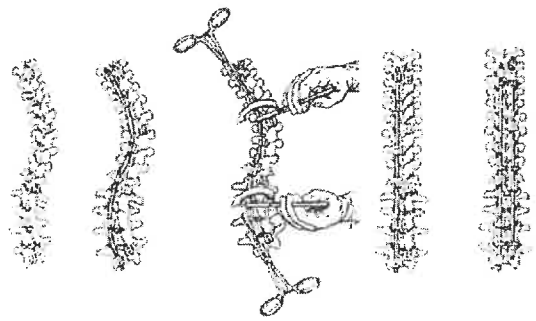

Figure 2.15: Example of instrumentation CD (Lonstein 1995)

Posterior surgical approach

This approach to scoliosis surgery is done through a long incision on the back of the spine (the incision goes the entire length of the thoracic spine).

- After making the incision, the muscles are then stripped up off the spine to allow the surgeon access to the bony elements in the spine.
- The spine is then instrumented (screws are inserted) and the rods are used to reduce the amount of the curvature.
- Bone is then added (either the patient's own bone, taken from the patient's hip, or artificial bone), which in turn incites a reaction that results in the spine fusing together.
- This fusion process usually takes about 3 to 6 months, and can continue for up to 12 months.

For patients who have a severe deformity and/or those who have a very rigid curvature, an anterior release of the disc space (removal of the disc from the front) may first be required. This involves approaching the front of the spine either through an open incision or with a scope (thoracoscopic technique) and releasing the disc space. After the discs at

the appropriate levels of the spine have been removed, bone (either the patient's own bone and/or artificial bone) is added to the disc space to allow it to fuse together. After the disc has been released and fused, the posterior portion of the scoliosis surgery described above is performed.

Anterior surgical approach

For curves that are mainly at the thoracolumbar junction (T12-L1), scoliosis surgery can be done entirely as an anterior approach.

- This approach to scoliosis surgery requires an open incision and the removal of a rib (usually on the left side). Through this approach the diaphragm can be released from the chest wall and spine, and excellent exposure can be obtained for the thoracic and lumbar spinal vertebral bodies.
- The discs are removed and this loosens up the spine.
- Screws can then be placed in the vertebral bodies and a reduction of the curvature obtained and held with a rod.
- Bone is added to the disc space (either the patient's own bone, taken from the patient's hip, or artificial bone), to allow the spine to fuse together.
- This fusion process usually takes about 3 to 6 months, and can continue for up to 12 months.

Because of the non visibility of the trajectory of screws in the vicinity of spinal marrow, nerve ends and blood vessels, the most delicate phase of whole approach is the perforation which permits placement of the pedicle hook-screw in the vertebrae for instrumentation. Before a patient receives the perforation and placement of screws, the doctor must define his strategy: to decide the entrance points in the vertebra, the direction of perforation and the diameter and length of screws. Then, the operation scheme and data is carefully laid out, generally in 2D form (radiographic projection of studied scenes). Then, the doctor transforms mentally all the visible elements related to the operation zone, and uses anatomical knowledge so that the images can reasonably produce a 3D anatomical and pathologic impression (Bainvill 1998). However, in 9 to

45% of errors of placement of screws (Merloz 1999); the simple 2D images seem sub-optimal when they are used as the plan to implement the placement of pedicle screws. Costoplasties (rib shortening or lengthening) may correct scoliotic deformity. But, one does not completely understand the correction's effect on the human spine. To study the mechanisms between them, Gréalou (Géalou 2000) used the finite element model of human rib cage and spine, which has been built at Ste. Justine Hospital, to develop a biomechanical modeling method of rib surgeries. He built a three-dimensional geometric model of each patient's spine and rib cage to investigate the correction mechanisms. His simulation shows that the costoplasties produce slight geometric modification in rib and vertebrae, which indicates the internal loads are transmitted from the ribs to the vertebrae in rib surgeries, as well as from the vertebrae to the ribs in spine instrumentation. However, the definition of mechanical properties and boundary conditions of the model, which decides the biomechanical behavior of the model during the simulation, limits the accuracy of the results and the effect of the rib and vertebral growth was not taken into consideration. To further study the effect that rib surgeries could reestablish the force balance transmitted to the spine, to slow down the scoliotic deformation progression, Carrier (Carrier 2002) also adopted the Ste. Justine finite element model to simulate the influence of rib surgeries on the correction of the scoliotic deformities. First, she employed six patients' personalized FE models to examine the rib surgery parameters' influence and to attain their optimal configuration. An approach based on experimental designs and interpolation techniques was applied to solve the optimization problem of FE modeling. Second, she integrated the bone growth modeling into the rib shortening or lengthening model. A modeling of the ligaments' stress relaxation is used to represent the influence of the loads of rib surgeries over time so that the model can simulate the evolution of the trunk geometry after 24 months. Her simulation shows that the elements representing the rib hump and the axial rotation of vertebrae vary greatly and the loads induced on the vertebral end-plates can reduce the progression of scoliotic deformation. The biomechanical FE model is also used to confirm the long-term correction effect of

rib surgeries. However, her model does not consider the influence of loads due to gravity and muscle forces.

On the other hand, to directly examine the effect of scoliotic spine surgical instrumentation on spinal correction, Petit (Petit 2004) used multi-body modeling to simulate spinal instrumentation procedures on 82 patients undergoing spinal correction. Their vertebrae are modeled as rigid bodies whose transformation describes the vertebral rotation from preoperative to postoperative geometry. His simulation confirms that the average centers of vertebral rotation are adequate to describe the intervertebral joints of a biomechanical model and can be used to predict the short-term effect of spinal surgery.

2.3 Modeling techniques

Research on deformation simulation of the human trunk and virtual surgery covers a number of themes which range from medical imaging to robotics. In spite of its complexity, recently a lot of experimental results have been presented, and many problems in the domain discussed.

A deformable model represents a trunk or an anatomical structure, i.e., a certain volume with soft biological tissue which one will want to touch, deform and cross. Thus it should guarantee a certain biomechanical reality. This is why one calls deformable models "physical" i.e., they are models from which the deformations are derived from the laws of the mechanics of the continuum medium. Although such models have been used for the structural analysis and modeling of interactions between fluids and solids for a long time, their use for animation or time-reality applications like simulation, is more recent, in particular under the impulse of work of D. Terzopoulos (Terzopoulos 1987, 1988). The deformable models can represent the geometrical and physical approximation of the object. The degree and nature of the realized approximations give the condition to achieve realism in the obtained model.

In general it is impossible to solve the equations of mechanics in the analytical method. Therefore, one must have recourse to numerical analysis to find a solution. However any numerical calculation is restricted on a discretized field on which one works and the

geometrical approximation of the field is applied. There are several ways to represent the object in a discrete field. The first stage is to divide it into elementary subfields. For example in two dimensions, an object can be represented by a collection of points, spheres, or polygons. Thus this stage makes it possible to define the basic forms on which the equations of the problem will be approximated, which corresponds to fixing the number of degrees of freedom. The quality of the discretization depends, of course, on the number of subfields which one uses to describe the object. Then one can differentiate the structured geometrical models, i.e., those where the subfields have a topological relation with their neighbors, and the non-structured models where the elements can move freely amongst one another. Here, we will give some typical methods which are essential to approach physical simulation, although they are not exhaustive. We classify them into different categories.

2.3.1 Deformation of geometric surface

This class of algorithms is only an initial first step because they do not consider the intrinsic physical properties of deformable objects, but only consider the surfaces of objects to determine their forms. Some of them also apply partial physical properties in deforming the surface.

2.3.1.1 Free-form deformation

Historically, computer-assisted geometrical design (CAD) was one of the first fields to use techniques of deformation of objects. The designers wanted to be able to handle and refine the digital representation of their object. From then, the curves of Bézier and the family of splines were produced, including curves of interpolation, B-splines, rational splines, non-uniforms (NURBS). They all define a smooth curve with a few values in 1, 2 or 3 dimensions (see Bartels 1987, Farin 1990 for a more complete reference). These curves and associated surfaces will generally be defined by control points whose displacement will modify the aspect of the curve in an intuitive way (see figure 2.16). A direct manipulation technique, allowing the B-spline curve or surface to be manipulated

with points that lie on the curve itself, also offers an alternative to control vertex manipulation (Bartels 1989).

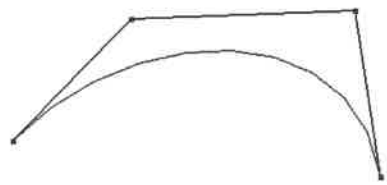

Figure 2.16: Four control points, their defined curve of Bézier and tangents at the beginning and end of the control polygon.

2.3.1.2 Deformations of space

Another way of modifying overall the shape of an object is to deform the space in which it resides. One can for example replace coordinate x by - x to carry out a symmetrical transformation. The transformations can be much more complex and have the advantage, by deforming all space, to be applied as well to polygonal surfaces, splines, and parametric implicit surfaces. Figure 2.17 illustrates this idea.

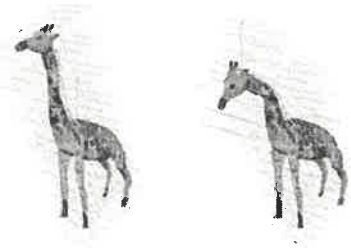

(a) (b)

Figure 2.17: Deformation of space illustrated on a model of the giraffe: the original grid (a) and the deformed one obtained after a local deformation (b).

This work began with Barr (Barr 1984) and consisted of metric functions of $\mathbb{R}^3$ into $\mathbb{R}^3$ (causing rigid deformations, folding, tapering) which could be combined to give complex effects. Sederberg and Parry generalized this approach (Sedeberg 1986) by the introduction of the FFD, or Free-Form Deformation. The object is imbedded in a grid which could be deformed, each cell of the grid involving with it the points which it

contains by means of interpolations using Bernstein polynomials. Extensions, involving the separation into several sub-areas of the deforming grid (Coquillart 1990) or using multiresolution (MacCracken 1996) (grids capable of arbitrary topology due to use of algorithms of subdivision) are presented. We mention also a method which infers, by the use of least squares, the direct modification of the grid to what one wants, subject to the position of points of the surface (Hsu 1992).

2.3.1.3 Implicit surface

The surface of an object can also be represented implicitly, rather than explicitly, using polygons or splines. One creates a scalar field in all of space, and the surface is defined as the place where this field has a given value. These fields generally derive from potential and equipotential surfaces or iso-surfaces. This potential is often a monotone function of the distance to a skeleton, which can be a point, a segment or any other more complex form (Nicholas 1990).

This formulation has many interesting properties: according to whether the value of field at a point in space has a lower or higher value than the iso-value, one can judge if it is inside or outside the object, which allows in particular a very fast detection of collisions. The combination of several implicit objects can be very simple by applying the various potentials which generate them, which also allows the management of objects with variable topology. The iso-surface is divided naturally when the two components separate.

On the other hand, the visualization of such surfaces is more complex since their polygonalisation is difficult. One will be able to use the algorithms of the cubic marching (Wyvill 1986; Bloomenthal 1987, 1988), the local grids (Desbrun 1996) or the method based on particles (Witkin 1994) to render them.

The overall approach, then, is to define the surface of an object using the potential method. Its animation will consist in animating the skeletons which generate it, changing the surface consequently, maintaining continuity or changes of topology. One will

modify manually only the few positions of these skeletons, which are generally precise masses, leaving this task to generating models.

These geometrical methods were especially presented as an introduction because some will be referred to again later. They have the advantage of being generally very fast and offering a great control on the deformation produced. On the other hand, they cannot be applied directly to the case where the movement is directly created by the user since the user's skill will decide the result. One will thus use rather generating models, which will simulate laws of behavior, more or less physical, and will thus generate automatically the movement of the object. There exist many generating methods and we will describe the principal families of them in what follows.

2.3.2 Mass-spring model

When one endeavors to represent a soft object, the simplest and most intuitive model is undoubtedly the mass-spring network. It consists in modeling the object by a collection of points connected to each other by line. The points represent specific masses, and the lines are regarded as springs. With each iteration, one calculates the forces exerted by each spring on both its ends. These forces are expressed according to the variation of length of the spring and its stiffness. One can then calculate the new positions of the masses by integrating their motion equations. There are several reasons for the success of this model. First of all, it is very effective because calculations are very simple. In particular it is possible to use several mass-spring models to simulate a complex scene. For example, Nedel models the muscles of a virtual human with surface networks of a mass-spring (Nedel 1998a, 1998b). Moreover, this intuitive model makes it possible to add many improvements. For example, one can change the behavior of the springs and their stiffness to build non-linear and non-homogeneous models (D'aulignac 1999a, Boux 1999) or anisotropic (Bourguignon 2000). On the other hand, the principal defect of this model is the necessity to discretize the directions along which the forces are exerted inside material. Indeed, the forces are completely directed following the edges which make up the geometrical grid. The implication of this property is that the total

behavior of the simulated object will depend on the geometry of the grid, and more particularly of the distribution of the directions of the edges. Many works involve the improvement of the behavior of this model. For example, Y. Chen proposes a relatively sophisticated mass-spring network including various types of springs (structural springs, shearing springs and flexion springs) in order to simulate the deformation of a muscle at the time of its contraction (Chen 1998). It is also possible to improve the realism the of mass-spring model by imposing on the springs a behavior derived from experimental measurements (Bourguignon 2000), or by adjusting the stiffness of the springs so that the model reaches the desired behavior (D'aulignac 1999b). O. Deussen proposes methods to improve a mass-spring model in several ways (Deussen 1995). He starts by optimizing the distribution of the vertices of the grid using an iterative decomposition of the field in diagrams of Voronoi. Then he calculates the value of the masses distributed to each vertex so as to preserve the moments of inertia of orders 1 and 2 inside the model. Lastly, he deduces the stiffness from the springs by identifying his model with a linear elastic model. Similarly, A. Gelder proposes a formula making it possible to calculate the stiffness of the springs so that the mass-spring model approaches as much as possible its linear elastic counterpart discretized by the finite element method (Gelder 1997). Lastly, one can quote work of Desbrun, who proposes an algorithm of integration allowing to stabilize and to accelerate the calculation of the deformations of a mass-spring model (Desbrun 1999). Some of its properties and limits are summarized as follows, so as to provide us some reference to decide which physical model is more suitable for our purpose.

- The mass-spring model as a physically-based model is ideal to form a dynamic and deformable object and its parameters have obvious physical connotations so as to be easy to understand and to specify in accordance with different needs. Its rate of animation can change with the specification of the length of each step time so as to reach a real-time and interactive simulation under certain non-rigid conditions. Since the mass-spring model reflects interaction between a node and

its neighbor nodes which are relatively independent of other nodes, i.e. its local nature, parallel algorithms may be applied to accelerate rendering.

- An object which has the character of a continuum is approximated using a discrete model which is obtained by the computation and control of some discrete elements. The number of extracted points depends on the requirements of accuracy to approximate a geometric surface and corresponding expense of computation time. Although it solves the numeric computation problem on the computer, the error of approximation is also attained. The final result of the approach is always stated as a set of points in space and the original continuity of the solution has been lost.
- The basic mass-spring elastic model does not allow enforcing certain global properties, such as the incompressibility of some tissues. One way is to compute tissue volume when we solve the motion equation and to add pressure forces to mesh nodes located in the tissue surface in order to maintain constant volume.
- The lattice is tuned through its spring constants, and proper values for these constants are not always easy to derive from measured material properties. The adjustment of these parameters (mass, damping and stiffness) will be extremely time-consuming because the parameters influence each other and the anisotropy of our modeled object, human trunk.
- In addition, certain constraints are not naturally expressed in the model. For example, incompressible volumetric objects or thin surfaces that are resistant to bending are difficult to model in a mass-spring system. But these phenomena can sometimes be modeled using additional springs, with an increase in computational cost.
- Mass-spring systems sometimes exhibit a problem referred to as "stiffness" which can occur when spring constants are large, such as modeling a nearly rigid object, or hard constraints due to physical interactions, such as a non-penetration constraint between a deformable object and a rigid object. In modeling, when instability occurs due to the high rigidity and unfit time step of integration, we

have to adopt small time step to reach numerically stable integration, which slows the process of simulation.

- Mass-spring modeling can directly represent an object's local properties and thus facilitate the rendering of anisotropic, nonlinear and non-homogeneous tissue structure.

2.3.3 Finite element model

The finite element method is a method which takes account of the physical properties of material to simulate a deformable material. In industry, the finite element method in mechanics and mathematics has been applied for several decades. They mainly use the continuous model. The literature on the subject often discusses methods that are too accurate and too expensive, whereas the required visual result in animation does not require such a precise model. It is somewhat difficult to understand, but the general method can be explained more simply. This technique can be used to study not only the static positions of balance but also the dynamic evolution of objects in the course of time. Calculation is often very long. Although it also has a lot of disadvantages, preventing its broad application, it also has obvious advantages.

The following description is much simplified and the reader should refer to (Segerlind 1984, Bathe 1996, Kass 1997 and Zienkiewicz 2000) for more details.

The surface and volume representation of the finite element model are the most widely used in engineering. The approach describes a shape as a set of basic elements (triangles, quadrilaterals, tetrahedrons), where shape functions with limited support are defined (Zienkiewicz 2000a). This leads to continuous representations with varying levels of continuity. A finite element model is fully defined by the choice of its elements, its shape function and its global parameterization between parameter spaces Ω and R^3 (for $\Omega \in R^2$ surfaces and $\Omega \in R^3$ for volumes). For surfaces that are neither topologically planar nor cylindrical, the parameterization can be problematic. Finite elements with C^0 continuity, where the shape node consists of a vertex position are similar to finite

difference methods. Similarly, Bézier splines, B-splines or Hermite splines can be seen as finite elements with specific shape functions.

The first application of finite element method to animation was done by Gourret et al in a simulation of contact between a deformable hand and a ball (Gourret 1989). The response to collisions is somewhat empirical and the modeling of the fingers is simple, but the simulation allows a complex deformation. The matrices are recalculated when the knuckles move more than ten degrees. Simulation takes a long time to calculate and dynamics was removed in order not to slow down it more.

Later Collier et al produced a fabric modeler using square elements in two dimensions (Collier 1991). Chen and Zeltzer tried using them to animate human muscles (Chen 1992). Their elements are very complex (20 nodes each) and they use only 2 per muscle. The muscles are seen imposing forces by the medium of the tendons which connect them to the bones. Although using the principles of formal dynamics, their simulation of a few tens of nodes is very slow.

Bro-Nielsen and Cotin used an interesting idea in 1996 by noticing simply that only the displacement of the nodes of the surface is relevant visually (Bro-Nielsen 1996). The matrix system can be rewritten by separating these nodes from those of the interior. This method, called condensation by the authors, leads to a matrix system which now relates only to the surface nodes which are much less numerous, but which on the other hand lost the structure of the middle of the matrix. This process, traditionally in physics, had already been applied in (Gourret 1989).

James and Pai (James 1999) proposed a method based on the same principle, but in which they updated the inverse of the tangent matrix. When the user handles a virtual tool to deform the object, few nodes pass from moving state to rest state, and conversely. The authors pointed out that the matrix inverse was modified only little in fact in these cases. The influence of a point is limited to a column of the matrix and a mathematical trick makes it possible to quickly update the matrix using pre-calculations to reach real-time animation.

In his thesis (Cotin 1997), Cotin proposed a method imposing constraint once on the displacement of the object. He uses the interesting property of superposition of the finite elements in linear elasticity, which says that the deformation of object resulting from displacement of a point is the sum of those which would be produced by displacements. x y and z separately applied in each direction X, Y and Z. A double displacement will simply create a double deformation due to the linear character of the system of equations. The problem is that one cannot know the created deformation when one at the same time handles more than one point. Summing each deformation created by the moved points will lead to an exaggerated deformation. Cotin, however, does not apply any part and only represents the mutual influence of the moved nodes. The inverse of the tangent matrix will determine displacements of different nodes. One can thus move several vertices, but at the price of calculating the inverse of a matrix.

One of the defects of these three methods (Bro-Nielsen 1996, James 1999, Cotin 1997) is that all the precalculated matrices could no longer be used when any modification of the topology of the object (a simple notch or a major cutting) occurs. Another disadvantage is that their model is static so that it is very sensitive to external loading. When the loading leaves the object abruptly, the object returns immediately to its original equilibrium position without any dynamic oscillation.

Finite element models have been used widely to compute soft tissue deformations under mechanical constraints. In the past few years, real-time finite element models have been developed as an alternative to spring models. Sagar (Sagar 1994) developed a virtual environment for eye surgery simulation where the cornea deformation is modeled as a non-linear elastic material (Mooney-Rivlin material). The finite element solver computed the cornea deformation every second while the graphics module was able to provide a 10Hz refresh rate. In (Cotin 1996), Cotin et al. describe a hepatic surgery simulator where the liver is represented as a linear elastic volumetric model with static constraints. By pre-computing the response of surface vertices to position constraints, the liver model can be deformed in real-time. Furthermore, the force-feedback computation and the liver deformation computation can be decoupled to achieve optimal haptic display (500Hz)

and visual display (30Hz). Similarly, Bro-Nielsen (Bro-Nielsen 1996) decreased the computation time of a linear elastic model with a semi-implicit scheme, by condensing and explicitly inverting the reduced stiffness matrix in a preprocessing stage. Video frame-rates of 15-20 frames/second were obtained with this method. By taking advantage of the linear nature of the static or dynamic equation, the methods of Cotin (Cotin 1996, 1997) and Bro-Nielsen (Bro-Nielsen 1996) decrease the computation time of finite element models by at least factor of 100. However, such optimizations are not compatible with the topological change entailed by suturing or cutting, where the stiffness matrix must be updated.

In conclusion, finite element models are well suited to compute accurate and complex deformation of soft tissue. However, it is extremely time-consuming on a moderately powerful workstation using finite element models. But for linear elastic models, only valid for small displacements, it is possible to reduce computation time. Unlike spring models, there is no restriction on the stiffness value of the model with respect to the time step when using semi-implicit or static schemes. We list its series of properties below compared with mass-spring to help us to choose correct model related to deformation of spine and soft tissue.

- Finite element method provides us a more realistic simulation to real world and human models with fewer nodes which reduce the computation and complexity of the system. Because mass and stiffness matrices are derived by numerical integration over the elements, pre-processing the matrices leads to significant reduction of computation time during actual simulation.
- The finite element method is well suited to interactive definition of objects with free-form surfaces and numerical methods to process continuous objects.
- FEM methods have been extensively studied in numerical analysis. They are often regarded as a more rigorous representation of tissue physics than mass-spring models, because they do not discretize the equations of motion and they produce a solution over the entire domain. However, their computational cost

tends to be greater than mass-spring models, especially when nonlinear elastic models and dynamic simulation, as in our research, are considered.

- The method is built on physical mechanism which is used to deduce the behavior by minimizing the energy of a system which consists of a solution of dynamic equation of Lagrange. The integration of local discretized nodes which forms the local depiction of motion of the deformed object requires a matrix calculation at each time step, which may prevent interactivity and cause the impossibility of real-time animation.
- On the other hand, the behavior of each material, such as elastic, inelastic or plastic, holding different characteristics, is described by a special equation which can be solved in selecting the proper method and implementation routine. Based on having no general equation to embody a universal substance, our choice of the equation and method to simulate dynamic deformed object must be corresponding to its proprieties.
- Similarly, no general software can be applied in all deformable materials and every parameter designated to modify the object intuitively must lie in special situation. Attaining the more intuitive, more universal and simpler model to manipulate a variety of materials is a major research field in computer graphics.
- In application, forces enforced on object must be converted to their equivalent discrete force vectors, which requires numerically integrating distributed forces on the volume at each time step and increases computation time.
- If the topology of the object changes during simulation, or the object shape changes beyond small deformation limits, the mass and stiffness matrices must be re-evaluated at the time of simulation. The great cost of this in time prevents real-time and interactive performance.
- When a human tissue domain is treated by finite element method, its change is very great after deformation since human tissue can stretch greatly. This violates the basic assumption of the method that is originally developed to compute functions or a vector field over a fixed domain. For a similar reason, the method

has difficulty dealing with change on tissue topology, barring a prohibitive computational cost.

The performance of current soft tissue models are summarized in Table 2.3. Mass-spring models have been developed in computer graphics for their simple and efficient implementation. But finite element models are mostly used in biomechanics because they aim at modeling accurate deformations as in our project. We select the finite element model also because our model demands very high accuracy, in order to be comparable with real deformable anatomical tissue. On the other hand, its disadvantage (slowness of computation) does not greatly prohibit the implementation of deformation since our model is not required to work in a real time environment. Finally, visualization of finite elements is well suited for graphics hardware since it consists in rendering visible elements. As a conclusion, finite element models are well suited to compute accurate and complex deformation of soft tissue which arises in our trunk model.

Table 2.3: Comparison of mass-spring and finite element method

	Deformation Accuracy	Computation Time	Visualization
Finite Element Model	Excellent	Slow	Excellent
Spring Model	Good	Fast	Good

2.3.3.1 Finite element physical model

Consider a body in an initial state at time $t = 0$ which is shown in figure (2.18). Its domain in the initial state is called the reference configuration which is referred to by various equations in describing the motion of the body and deformation. The domain of current configuration which is also called deformed configuration is denoted by Ω, and its boundary is denoted Γ. The vector X for a given material point in the initial domain does not change with time and is called material coordinates or Lagrangian coordinates.

x is the position vector in the current configuration and it gives the spatial position which is also called Eulerian coordinates. The function $\Phi(X,t)$ maps the reference configuration to the current configuration and can be given by the addition between its original position and its displacement as illustrated by figure 2.18:

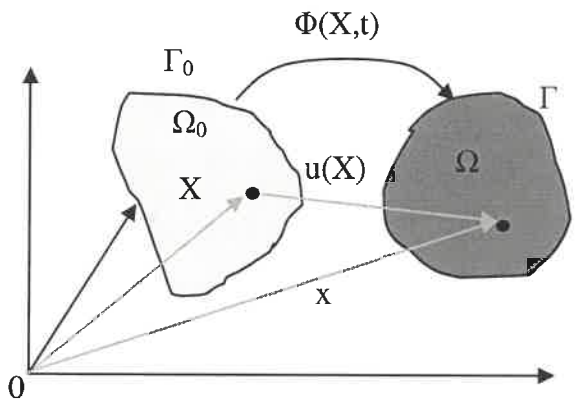

Figure 2.18: Undeformed (initial) and deformed (current configuration) of a body

$$\Phi(X,t) = X + u(X,t) \tag{2.1}$$

A fundamental measure of deformation is described by the deformation gradient $\nabla\Phi = I + \nabla u$ (I matrix identity) which must be subject to the constraint $J = \det(\nabla\Phi) > 0$ to ensure that material volume elements remain positive. The deformation gradient is a direct measure which maps a differential line element in the reference configuration into one in the current configuration.

We choose the Cauchy elastic material to simulate deformable material because the deformation only depends on the current value of the deformation gradient and not on the history of the motion. In a Lagrangien reference configuration, the deformation tensor can be described as a symmetrical 3x3 matrix which is denoted by:

$$C = \nabla\Phi^{t}\nabla\Phi \tag{2.2}$$

(Picinbono 2001, eq. 1.2). It is invariant in rigid transformation, i.e. translation and rotation. One usually uses the right Cauchy Green deformation tensor C to compute the second Piola-Kirchhoff stress and work. However, the work done may depend on the

deformation history or load path. This tensor also comprises the part of the non-rigid deformation. In this variation, there are two types of variables.

As the following figure (figure 2.19(b)), the deformation of a cube is divided into two types. One type of variables makes the deformation stretch respectively along three axes and these three variables separately are put in the diagonal in the Cauchy Green tensor C. For example, the variable which makes the cube stretch along the Z axis can be denoted by

$$C_{22} = \left(\frac{\partial \phi}{\partial z}\right)^2 + \left(\frac{\partial \psi}{\partial z}\right)^2 + \left(\frac{\partial \varsigma}{\partial z}\right)^2 = \left(\frac{\partial \Phi}{\partial z}\right) \cdot \left(\frac{\partial \Phi}{\partial z}\right) = \left\| \frac{\partial \Phi}{\partial z} \right\|^2 \qquad (2.3)$$

(Picinbono 2001, eq. 1.5). The three other elements of the Cauchy Green tensor (symmetrical matrix) represent the shearing of the surface on which they act with respect to the neighboring surface (figure 2.19(c)).

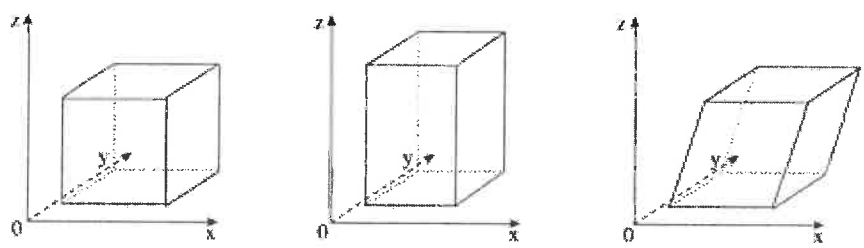

(a) Status at rest (b) stretching (c) Shearing

Figure 2.19: Components of the deformation of a cubic (Picinbono 2001)

For instance, the shearing between the XOY and YOZ planes is denoted by

$$C_{02} = \frac{\partial \varphi}{\partial x}\frac{\partial \varphi}{\partial z} + \frac{\partial \psi}{\partial x}\frac{\partial \psi}{\partial z} + \frac{\partial \zeta}{\partial x}\frac{\partial \zeta}{\partial z} = \left(\frac{\partial \Phi}{\partial x}\right) \cdot \left(\frac{\partial \Phi}{\partial z}\right) \qquad (2.4)$$

(Picinbono 2001, eq. 1.6). Green strain tensor E measures the difference of the square of the length of an infinitesimal segment in the current (deformed) configuration and the reference (undeformed) configuration. It can be expressed in terms of Cauchy Green and displacement gradients by

$$E = \frac{1}{2}(C - I) = \frac{1}{2}\left(\nabla u^t + \nabla u + \nabla u^t \nabla u\right) \qquad (2.5)$$

(Picinbono 2001, eq. 1.7). It also retains the invariance of Cauchy Green tensor in rigid body motion.

Like the Cauchy Green tensor, the three diagonal elements $(\varepsilon_x, \varepsilon_y, \varepsilon_z)$ of E represent the stretching of the volume element in three directions of space. The three other elements $\gamma_{xy}, \gamma_{xz}, \gamma_{yz}$, represent shearing in the volume element. The tensor E is expressed in terms of these six components of deformation as follows:

$$E = \frac{1}{2}\begin{bmatrix} 2\varepsilon_x & \gamma_{xy} & \gamma_{xz} \\ \gamma_{xy} & 2\varepsilon_y & \gamma_{yz} \\ \gamma_{xz} & \gamma_{yz} & 2\varepsilon_z \end{bmatrix} \text{ where } \begin{aligned} \varepsilon_x &= u_x + \frac{1}{2}\left(u_x^2 + v_x^2 + w_x^2\right) \\ \varepsilon_y &= u_y + \frac{1}{2}\left(u_y^2 + v_y^2 + w_y^2\right) \\ \varepsilon_z &= u_z + \frac{1}{2}\left(u_z^2 + v_z^2 + w_z^2\right) \\ \gamma_{xy} &= \left(u_y + v_x\right) + \left(u_x u_y + v_x v_y + w_x w_y\right) \\ \gamma_{xz} &= \left(u_z + v_x\right) + \left(u_x u_z + v_x v_z + w_x w_z\right) \\ \gamma_{yz} &= \left(u_z + v_y\right) + \left(u_y u_z + v_y v_z + w_y w_z\right) \end{aligned} \qquad (2.6)$$

(Picinbono 2001, eq. 1.8). If one only retains the linear part of the tensor E, one can directly deduce the linear mechanics of elastic deformation of the continuous mediums, which is represented by:

$$E = \frac{1}{2}\left(\nabla u^t + \nabla u\right) \qquad (2.7)$$

(Picinbono 2001, eq. 1.9). Usually, the deformation of material is driven by two types of forces which act on the deformation domain. The voluminal force can be applied to the whole or partial domain of the object, as in the case of gravity. However, the surface force can only be exerted on the object's boundary.

In a continuous medium, adjacent parts push or pull each other via certain surface areas. Such a force, called the traction force, should be measured per unit area. After the theorem of conservation of linear momentum and angular momentum, and the Cauchy theorem are applied to the volume element inside the relevant body, the traction force $t(x,n)$ depends on the Cauchy stress tensor $\sigma(x)$. Given the spatial normal unit vector n of the surface, the spatial traction force $t(x,n)$ can be expressed as a function of $\sigma(x)$:

$t(x,n) = \sigma(x)n$ which is expressed in the Eulerien reference configuration. One transforms the relationship between the stress and displacement gradient into Lagrangien reference configuration and obtains the first Piola-Kirchhoff stress tensor:

$$\sigma(X) = \det(\nabla\Phi(X))\sigma(x)\left(\nabla\Phi(X)^t\right)^{-1},\ x = \Phi(X) \qquad (2.8)$$

(Picinbono 2001, eq. 1.2). Because the stress is not symmetrical whereas the Cauchy tensor is symmetric, one transforms the first Piola-Kirchhoff by multiplying $\nabla\Phi(X)^{-1}$ to obtain the second symmetric Piola-Kirchhoff tensor

$$S = \nabla\Phi(X)^{-1}\sigma(X) \qquad (2.9)$$

(Picinbono 2001, eq. 1.2). It is often used to compute the work by multiplying the rate of Green strain tensor, which is denoted by the gradient of the velocity field in the reference configuration of the material coordinate system. Thus they are called the conjugate pair in the sense of work. The conjugate relationship is used to develop the weak forms of the momentum equation: measurement of stress and strain rate which are conjugate in work can be used to construct principles of virtual work.

2.3.3.2 Linear model

Linear elastic volumetric finite element models have been widely used to model the deformation of soft tissue. In such cases, the stress/strain relationship is represented by a linear equation: $F = KX$. The stiffness matrix K depends on the rest shape geometry, the Young modulus E and the Poisson ratio parameters. In most cases, only C^0 elements are used, leading to simple shape functions. Owing to the fast speed and simplicity of the linear finite element, it has been broadly applied to the simulation of human tissue in the medical field in spite of its limited ability to validate the change of material. We initially present a deformable model founded on linear elasticity and the finite element method. Our algorithm uses a FEM with 4-node tetrahedral elements with linear shape functions. We have chosen this element because:

- In a mesh composed of 4-node tetrahedral elements, each node has a relatively small number of neighbors. This results in fewer non-zero elements in the

stiffness matrix and less expensive computation. Higher order elements such as 6-node hexahedral elements, on the other hand, produce denser stiffness matrices.

- 4-node tetrahedral elements simplify the integration of the derivatives of the potential energy. This integration is essential for computing the stiffness matrix. Precise integrations for higher order elements are expensive, and usually require numerical integration techniques such as Gaussian quadrature with more Gauss points.
- A tetrahedron does not self-penetrate. As a result, the penetration problem is reduced to pairwise element-element problem. A higher order element can deform and result in self-intersection, which makes the penetration problem much more complicated.

A finite element procedure is usually divided into three parts:

(a) Divide the continuum into a finite number of parts (elements). In each element, construct the continuum field by interpolating on certain points using a certain simple function which describes how quantities vary continuously within elements; its behavior is specified by a finite number of parameters.

(b) For each element, express the component of the equilibrium equation in terms of the interpolation functions and the element's node displacements.

(c) Solve the complete system as an assembly of its elements to obtain the node displacements over the whole object.

In our project, we adopt the finite element of type P_1 (polynomial of degree one) as the interpolation function. Because the approximation of using this shape function belongs to the Hilbert space H_1 (Sobolev space with L_2 norm), it is sufficiently smooth to solve the second order differential equations, which include all PDEs used in this work. One discretizes the elastic energy of deformation and the displacements u inside each tetrahedron is expressed as the interpolation function of its four vertices:

$$u(X) = \sum_{j=0}^{3} N_j(X) u_j \,. \tag{2.10}$$

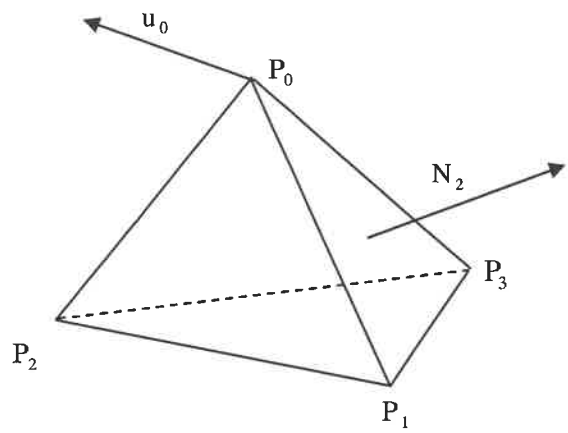

Figure 2.20: Finite element of tetrahedron type

The displacement gradient can also be denoted by:

$$\nabla u = \sum_{j=0}^{3} u_j \otimes \nabla N_j \qquad (2.11)$$

(Picinbono 2001, eq. 2.5), where '$\otimes$' indicates tensor product i.e. $u \otimes v \equiv u_i v_j$. Because the displacement gradient is constant inside each tetrahedron, on the entire grid, it is represented by a piecewise constant function.

Now, the linear potential energy inside one tetrahedron can be represented as the function of displacement:

$$W^l(T) = \frac{1}{2}\sum_{j=0}^{3} u_j^t \left[B_T^{jk}\right] u_k \text{ with } B_T^{jk} = \lambda\left(N_k \otimes N_j\right) + \mu\left(N_j \cdot N_k\right) \mathrm{I_d} \qquad (2.12)$$

(Picinbono 2001 eq. 2.9). The $\left\{\mathrm{B_T^{jk}}; \mathrm{j,k} = 1\ldots3\right\}$ are symmetric (3x3) matrices which represent the local stiffness matrix in the tetrahedron.

This potential energy also describes the current energy contained in the tetrahedron. When it is separately differentiated by four tetrahedral vertices P_p, we can obtain the forces acting on each vertex and the force inside the tetrahedron which is approximated by the interpolation function. One can divide the force on each vertex into two parts, which is denoted by

$$F_p^l(T) = \sum_{j=0}^{3} \left[B_T^{pj}\right] u_j = \left[B_T^{pp}\right] u_p + \sum_{\substack{j=0 \\ j \neq p}}^{3} \left[B_T^{pj}\right] u_j \qquad (2.13)$$

(Picinbono 2001 eq. 2.11). The forces of the first part return the vertex to its rest position and the forces of the second part make the vertex move toward its neighbor which produces the force on it. This mechanism allows the external force to spread to the whole domain and produce deformation through the nodal displacement.

Now, we assemble the small local stiffness matrix of the equilibrium equation in each tetrahedron into a global, large but sparse stiffness matrix. The forces on each node P consist of its own inertia force and the sum of forces coming from its adjacent nodes connecting it by an edge and are denoted by

$$F_p^l = \sum_{T \in v(P_p)} F_p^l(T) = \sum_{T \in v(P_p)} \left(\left[B_T^{pp}\right] u_p + \sum_{\substack{j=0 \\ j \neq p}}^{3} \left[B_T^{pj}\right] u_j \right) = \left[B^{pp}\right] u_p + \sum_{A \in v(P_p)}^{3} \left[B^{pj}\right] u_j \quad (2.14)$$

where

$T \in v(P_p)$: sum on all tetrahedrons pertaining to the vicinity of vertex P_p and A is in the set of tetrahedrons: sum on all edges pertaining to the vicinity of vertex P_p (Picinbono 2001 eq. 2.12). The expressions define the relationship between the force formed on a node and its and its adjacent nodes' displacements.

2.3.3.3 Limits of the linear elastic model

Although linear elasticity has many advantages due to the simplicity of the equations and possibilities of optimization, it nevertheless presents a strong restriction, namely, that it is limited to small displacements. The linear relation between strain and stress is not appropriate because it does not model large deformations exactly. The linearity is derived from the assumption of small deformations. It is admitted in general that this law of linear elasticity is valid only for displacements lower than the 10% of the total size of the deformed field (Fun 1993, Maurel 1998). Actually, that means that it is necessary to restrict displacements to be small enough so that the rotations generated by these

displacements can be approximated by translations, because due to using the linearized tensor of deformation, the model is no longer invariant w.r.t. rotation. When a volume element undergoes a rotation, it is interpreted as an increase in the elastic energy, which results in a distortion. First of all, we highlight the limitations of the elastic linear model, in particular the problems raised by the absence of invariance w.r.t. rotation.

When a linear elastic model takes a total rotation, one could imagine solving the problem by a change of suitable reference mark. But in the majority of cases, there is only part of simulated object which undergoes a rotation compared to the other part of field. It is in particular the case where a part of the object is fixed and that the rest is subjected to local rotation. Figure 2.21 shows a cylinder whose lower part is fixed. The higher part is subjected to a force directed along the right line. (b) Represents the deformations done by several successive forces. A dilation of the model is observed at the places where it undergoes a rotation. The cause is, during the deformation, a linear trajectory which is the reason for dilation. This dilation is unrealistic, since it occurs only in the plane of rotation. The same cylinder model of nonlinear Saint Venant-Kirchhoff elasticity is deformed under the same successive force whose direction is towards the right, like nonlinear model (Figure 2.21(c)) but the dilation does not occur on its top.

(a) Original (b) Linear (c) Nonlinear

Figure 2.21: Deformations of a linear elastic cylinder (a) original (b) linear elasticity and (c) nonlinear elasticity

For large global deformations of soft tissue in human body, the limits show the elastic linear model is not suitable when the model undergoes large displacements. The spinal deformation correction executed in Ste. Justine Hospital implies the material and

geometric non-linearity must be taken into account in simulating the deformation of human soft tissue (Périé2004). So, nonlinear models have to be considered to enhance the accuracy of simulation.

2.3.3.4 Nonlinear finite element model

Although the law of linear elastic strain has been used in small deformations in the elastic material, we can also improve their biomechanical behavior by adding the possibility of modeling anisotropic materials. However, even if these deformable models enable us to simulate the anatomical structural deformations which we require for medical deformation prediction, the limit is their linear elastic behavior. Because of the use of a linear relation between the deformation tensor E and the gradient of displacement ∇u , the models are no longer invariant by rotation. This results in distortions far from reality as soon as the assumption of small displacements is not valid any more. This is why we will be interested in a non-linear model. Non-linear elasticity is in general used when the principal objectives are precision and the biomechanical reality of the deformation. Vidrascu uses an incompressible model of Mooney-Rivlin to simulate the deformations of the liver (Vidrascu 1999). By using decomposition of field, calculations only require several minutes. Vuskovic and Kauer use non-linear liver models (neo-Hooke law and Veronda-Westmann model) to evaluate the constants of elasticity by identifying the simulated deformations and measured data *in vivo* (Vuskovic 1999a, 1999b, 2000, Kauer 1999). Non-linear elastic models are used to simulate the deformations of other bodies, such as the brain, in order to predict the deformations generated by the brain shift or the appearance (or the ablation) of a tumor (Kyriacou 1998, 1999), or skin with the aim of studying elasticity (Tsap 1998). Picinbono introduces nonlinear Saint Venant-Kirchhoff elastic finite elements to simulate the deformation of human soft tissue (liver), which overcomes the shortcoming of linear finite elements, which only allows a displacement of less than 10% of mesh size. Moreover, with the introduction of impressibility constraints, the model displays the more real deformation of living tissue of human body (Picinbono 2001). For the

simulation of gynecological surgery, Szekely et al use a model of Mooney-Rivlin (Székely 1998, 2000a and 2000b) which presents the deformation in real time by the means of a large scale parallelization (Rhomberg 1999). Zhuang uses an elastic model with large displacements to simulate the manipulation of objects in a virtual environment (Zhuang et al 1999, 2000). In addition, Hirota use three different types of nonlinear hyperelastic materials to simulate the bending motion of the human leg. The finite element method is employed to discretize the continuum model of non-rigid objects and the fast marching level set method is used to pre-compute a distance field for each undeformed body. He applies the penalty finite element formulation based on the concept of material depth to make the contact force a continuous function and analytically integrate the forces over contact surfaces. In the solution of the algebraic equations, he combines quasi-viscous Newton's iteration and adaptive-step size incremental loading with a predictor-corrector scheme. Finally, a quasi-static implicit finite element method is implemented to show a realistic contact effect of human soft tissue (Hirota 2002).

2.3.3.5 Hyperelastic material

The relation between stress and strain is determined by a constitutive equation. Several types of constitutive equations have been formulated (Marsden 1983). Since the problem addressed by our project involves biomechanical behavior of human organic tissues whose properties have not completely been understood, we choose the category of hyperelastic materials to describe the deformation of a human organ which exhibits a kind property of conservation of energy like hyperelastic material. A material is called elastic if the first Piola-Kirchhoff stress tensor at a point in material can be described only as a function of deformation gradient at that point (Marsden 1983). Whereas a material is called hyperelastic if there exists an elastic potential function W, also called the strain energy function per unit volume of the undeformed configuration and can be represented by a scalar function of strain of deformation tensors, whose derivatives with respect to a strain component determines the corresponding stress component.

$$S = 2\frac{\partial W}{\partial C} = \frac{\partial W}{\partial E} \tag{2.15}$$

(Belytschko 2000, p. 235). The total deformation energy in domain Ω is denoted by

$$\varepsilon = \int_{\Omega} W dX \tag{2.16}$$

If the material is isotropic and homogeneous, the function of potential energy W is completely characterized by the principal invariants of the Cauchy-Green deformation tensor C. These invariants are the coefficients of the eigen polynomial $\det(C\text{-}\lambda I)$ and are written with respect to C:

$$\begin{cases} I_1(C) = tr(C) = C_{ii} \\ I_2(C) = \frac{1}{2}\left\{(tr(C))^2 - tr(C^2)\right\} = \frac{1}{2}\left\{(C_{ii})^2 - C_{ij}C_{ji}\right\} \\ I_3(C) = \det(C) = \varepsilon_{ijk}C_{i1}C_{j2}C_{k3} \end{cases} \tag{2.17}$$

(Belytschko 2000, p. 238). The potential energy function of any hyperelastic material can be described as a polynomial function of the three invariants:

$$W = W(I_1, I_2, I_3). \tag{2.18}$$

Since the third invariant describes the local variation of volume, the deformation of incompressible materials can be constrained, such as $I_3 = 1$. One way of reinforcing the incompressibility is to introduce a multiplier of Lagrange or a constrained penalty function to ensure $I_3 = 1$. When $I_3 \neq 1$, an internal pressure is produced to oblige the material to find a balance guaranteeing its incompressibility.

Saint Venant-Kirchhoff element, which can simulate isotropic hyperelastic materials, is applied to our nonlinear finite element simulation. Its potential energy formulation can be defined as:

$$W = \frac{1}{2}E : C : E = \frac{1}{2}E_{ij}C_{ijkl}E_{kl} \tag{2.19}$$

(Belytschko 2000, p. 226) where the symbol ':' denotes the contraction of a pair if repeated indices which appear in the same order. By differentiating the potential with respect to the Green strain, the second Piola-Kirchhoff tensor can be represented as the function of the principal invariants of Cauchy-Green tensor:

$$S = \frac{\partial W}{\partial E} = \lambda tr(E)I + 2\mu E \qquad (2.20)$$

where λ and μ are the Lame constants which are related to the classic mechanic values describing the properties of elastic materials, i.e. the Young modulus E_y and the Poisson ratio v by the relationship:

$\lambda = \frac{vE_y}{(1+v)(1-2v)}$, $\mu = \frac{E_y}{2(1+v)}$ (Belytschko 2000, p.228). The Young modulus E_y characterizes the stiffness of material, while the Poisson ratio v represents its incompressibility. Since the relation between stress and strain is linear, this material is physically linear. On the other hand, the nonlinear relation between E and ∇u expresses a geometrical nonlinearity, i.e. elasticity in large displacements. These relations are used to completely represent the biomechanical behavior of elastic material which obeys the Saint Venant-Kirchhoff material characteristics.

2.3.3.6 Equilibrium equations

The total force acting on an elementary volume is the summation of the off-balance internal force (the divergence of the stress) and the external volumetric force. In the equilibrium state, the residual of force, vanishes.

$$R = \frac{\partial \sigma_{ji}}{\partial x_j} + \rho f_i - \rho \dot{v}_i = 0 \qquad \text{in } \Omega \qquad (2.21)$$

(Belytschko 2000, p. 146), where $\sigma(X,t)$ is Cauchy stress, $f(X,t)$ force per unit mass, $\dot{v}(X,t)$ the velocity, $\rho(X,t)$ the density.

The equation is, in general, not easy to satisfy. The difficulty stems from the fact that the equation, often referred to as a strong form, is a condition for every elementary volume in the material. The weak form or the principle of virtual work is obtained by converting the strong form into a condition for the entire region made of the material. The weak form enables the derivation of the finite element method that provides approximate solution of the equation. Here the principle of virtual work is derived.

Suppose the object is moving with an arbitrary or virtual velocity δv. At the equilibrium state, the residual force R does not do any work. The total virtual work δW done in the volume Ω is also zero

$$\delta W = \int_{\Omega} \delta v_i \left(\frac{\partial \sigma_{ji}}{\partial x_j} + \rho f_i - \rho \dot{v}_i \right) d\Omega = 0 \tag{2.22}$$

Using the chain rule and the Gauss theorem, we obtain the equilibrium as following

$$\delta W = \int_{\Omega} \frac{\partial(\delta v_i)}{\partial x_j} \sigma_{ij} d\Omega - \int_{\Omega} \delta v_i \rho f_i d\Omega + \int_{\Omega} \rho f_i \dot{v} d\Omega - \sum_{i=1}^{n_{SD}} \int_{\Gamma_{ti}} \delta v_i t_i d\Gamma = 0 \tag{2.23}$$

(Belytschko 2000, p. 147-148) where t is traction force which depends on the orientation of the surface and 'n_{SD}' denotes the number of space dimensions. Given the spatial normal vector n of the surface, the spatial traction force t is $t_i = \sigma_{ij} n_j$.

Note that qualifier "virtual" is used to make physical quantities hypothetical ones. Virtual velocity is not the actual velocity of the object; hence virtual work is not an actual energy increase, either. They are mathematical instruments to derive nodal forces in finite element methods. In the final algorithm, there are no virtual quantities. As a result, a general motion equation is derived with an added damping item which is also called Lagrangian motion equation:

$$\begin{aligned} \rho \frac{d^2 u}{dt^2} + c \frac{du}{dt} &= f(X) + \nabla \cdot \sigma(X), \qquad && X \in \Omega \\ t(X) &= \sigma(X) n && X \in \Gamma_1 \end{aligned} \tag{2.24}$$

$$\text{where} \begin{cases} \rho : \text{mass density} \\ c : \text{damping coefficient of material} \\ f : \text{density of volumic force} \\ t : \text{density of surface force} \end{cases}$$

(Picinbono 2001, eq.1.17). The finite element model can finally be discretized as a set of node vectors X. For static computation, the stress-strain relationship leads to $f(X) + \nabla \cdot \sigma = 0$. The following figure summarizes the reciprocal relationship between different variables. The deformation potential energy of elastic material can be

calculated by its deformation tensor and Lame coefficients. Then, the internal stress tensor deduced from the deformation potential and the voluminal and external surface stress form the dynamic motion equation to describe the deformation procedure of elastic material.

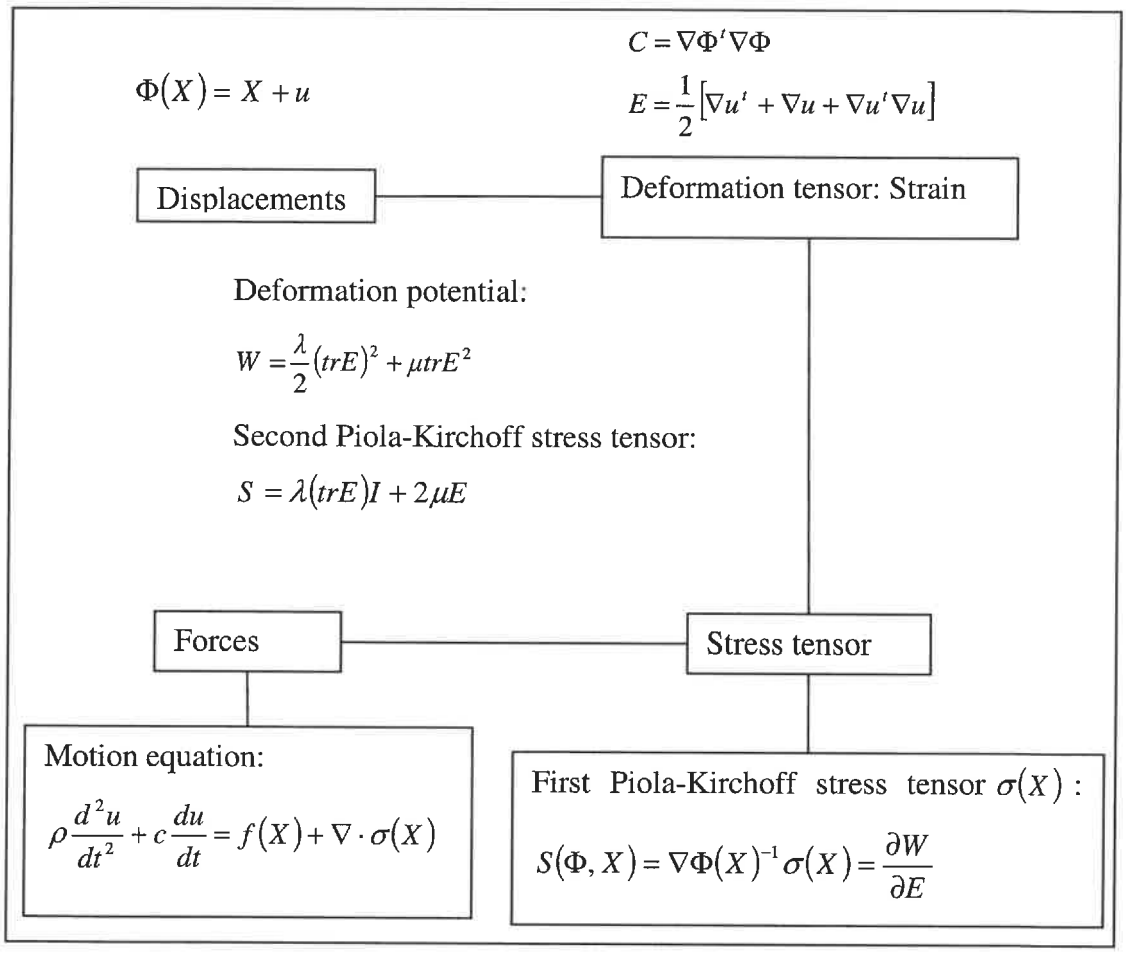

Figure 2.22: Transformation relationship between parameters (Picinbono 2001)

2.3.3.7 Solution of dynamic system

The most general approach for the solution of dynamic response of structural systems is the direct numerical integration of dynamic equilibrium equations. This involves, after the solution is defined at time zero, the attempt to satisfy dynamic equilibrium at discrete points in time. Most methods use equal time intervals at $\Delta t, 2\Delta t, 3\Delta t, \cdots, N\Delta t$. All

approaches can fundamentally be classified as either explicit or implicit integration methods.

The explicit finite elements are more often applied in systems of particles and benefit from its flexibility. The principle is as follows: when one writes the equilibrium equations on each element of the system, one is able to express the force which each vertex produces according to displacements of the neighbor vertices. One simply integrates these forces for each point, rather than seeking to find the position of equilibrium that these forces create by solving the matrix system. Thus, explicit schemes are simpler to compute and may not require matrix inversion.

Most finite element methods make use of implicit finite elements and attempt to satisfy the differential equation at time t, after the solution at time $t - \Delta t$ is found. The global solution of a system guarantees that the final positions are all compatible, satisfying all the equations overall. Although the method requires the solution of a set of equations at each time step, larger time steps may be used. Implicit schemes are unconditionally stable whereas explicit schemes are only conditionally stable.

In most implicit integration methods, we mainly used the Newmark algorithm (Zienkiewicz 2000b, Reddy 1993) in our work. To solve the nonlinear algebraic system, we used a Newton-Raphson method with linear search algorithm (see Appendix A).

2.4 Choice of materials and mechanical properties

The existing literature on the mechanical properties of human tissues is abundant, but relatively scarce when one looks for exact, comprehensive and representative data. There is a large scatter and uncertainty in the material properties of human tissue, according to sex, age, body size, etc. Furthermore, there may be large differences found in tissue properties within an individual at different parts of the body (Haug 1995).

The properties of organic tissues are being actively studied in biomechanics, and several models have been proposed based on stress-strain data obtained from in-vitro experiments. However, due to the limitations of measurement technology, those models have not been rigorously validated (Miller 2000). Some general important properties are

known about most biological tissues. These properties include 1) infinite energy with zero volume, 2) highly nonlinear stress strain relationship, and 3) anisotropy.

However, complex material properties such as plastic and viscoelastic phenomena generally observed in soft tissue experiments may be neglected if the deformation is small or if it is performed over a period of time that suffices for recovery processes in living organism. For the long term prediction of body tissue, a simplified constitutive model based on piecewise, isotropic, quasi-incompressible, linear elastic and non-linear hyperelastic material description is assumed.

A model of elasticity is considered as a large displacement model if it derives from a strain tensor that is a quadratic function of the deformation gradient. The Saint Venant-Kirchhoff model is a generalization of the linear model for large displacements, and it is a particular case of hyperelastic materials. Its basic energy equation is the same as the hyperelastic energy equation, but now E stands for the complete Green strain tensor: the material is applied to represent the deformation of all tissues which can be specified by different mechanic properties.

A trunk is principally composed of the spine, rib cage, lungs, diaphragm and many organs which are situated in abdominal cavity (stomach, intestine…). Many muscular layers cover the organs and play an important role in the adjustment of position of the organ and motion of trunk. Our model does not represent the muscular reaction and an isotropic linear and nonlinear elastic material is used to form muscle and soft tissue.

The model is mainly composed of three distinct parts, soft tissue, vertebra and ligament. The mechanical properties of the spine are selected from (Aubin 1995, Shirazi-Adl 1984, Teo 2003). A spine is composed of very complex different materials which have different biomechanical parameters. Their property values have been listed in table 2.4, which are used to simulate the finite element model of the thoracic vertebrae T10–T11 and have different value at different parts of a single vertebra.

Table 2.4: Vertebral material properties used in the finite element model

Component Name	Young's Modulus (MPa)	Poisson's Ratio	Reference
Cortical Bone	10000	0.30	(Shirazi-Adl 1984)
Cancellous Bone	100	0.2	(Shirazi-Adl 1984)
End plate	500	0.25	(Frymoyer 1991, Shirazi-Adl 1984)
Bony Posterior Element	3500	0.25	(Shirazi-Adl 1984, Teo 2001)
Disc–Annulus	4.2	0.45	(Shirazi-Adl 1984, Teo 2001)
Disc–Nucleus	1	0.499	(Shirazi-Adl 1984, Teo 2001)
Annulus Fiber	500		(Shirazi-Adl 1984)
Intertransverse Ligaments	58.7		(Teo 2003)
Capsular Ligaments	32.9		(Teo 2003)
Supraspinous Ligaments	15.0		(Teo 2003)
Interspinous Ligaments	11.6		(Qiu 2003, White 1990)
Ligamentum Flavum	19.5		(Teo 2003)
Anterior Longitudinal Ligaments	20.0		(Teo 2003)
Posterior Longitudinal Ligaments	20.0		(Teo 2003)

In our model, which simplifies the structure of vertebra, only two types of materials are used to describe the whole spine, namely the vertebra and the ligament between them. The soft tissue is also simplified as one material. In (Aubin 1995, Périé 2004), some different material properties listed below (table 2.5) are used to construct a personalized finite element model including the spine, rib cage or abdomen for each scoliotic patient in the LIS3D Laboratory of Ste. Justine Hospital of Montreal. But their mechanical properties are still not personalized and are only measured from the extrapolation of cadaveric data. We have investigated much of the literature and collected some mechanical properties about abdominal, fat and skin soft tissue (table 2.6) which is adopted as a reference to specify the properties of soft tissue in our model.

Table 2.5: Material biomechanical parameters of rib cage and vertebra

Tissue	Young's Modulus (MPa)	Poisson's Ratio	Reference
Cortical bone	5000	0.30	(Aubin 1995, Périé 2004)
Cortical bone (sternum)	10000	0.1	(Aubin 1995, Périé 2004)
Cancellous bone	1000	0.3	(Aubin 1995, Périé 2004)
Rib bone	5000	0.1	(Aubin 1995, Périé 2004)

Table 2.6: Mechanic properties of soft tissue used in the literature

Tissues	Young's Modulus (MPa)	Poisson's Ratio	Reference
Skin	100kPa		Bischoff et al 2000
Lung	2.5gm/cm	0.3	Matthews et al 1972
Abdomen	Spring		Macklem et al 1983
Abdomen	Incompressible body 4.7kPa		Dietrich et al 1990
Abdomen	Brick element 1.7kPa		Sundaram et Feng 1977
Abdomen			Belytschko et al 1978
Abdomen	0-20kPa		Marras et al 1991
Abdomen	0-30kPa		Ueyoshi et al 1985
Abdomen			Erdman et al 1997
Abdominal wall	1M	0.2	Delphine Périé
Abdominal cavity	0.01M	0.45	Delphine Périé
Elastin	0.6		Fung 1993
Collagen	1×10^{3}		Fung 1993
Thoracic aorta	0.62		Duck 1991
Abdominal aorta	1.2		Duck 1991
Muscle, along fibers	0.5		Duck 1991
Muscle, across fibers	0.79		Duck 1991
Fat	5×10^{-3}		Samani 1999
Skin	0.5		Samani 1999
Fat	1×10^{-3}		Schnabel 2001
Skin	0.09		Schnabel 2001

The material properties in our model are fundamentally described by the Young's modulus and the Poisson ratio. The Poisson ratio is used to characterize the incompressibility of material. It will be chosen near to 0.5 to improve the stability of the solution. On the other hand, although the Young's modulus really characterizes the elasticity of material, it is very difficult to measure on the trunk *in vivo*. Indeed, human organs being filled with blood, they will no longer have the same behavior *ex-vivo* where a part of the blood has run out, or has coagulated. Many works are undertaken to measure the biomechanical characteristics of bodies, of humans or animals (Davies 1999, Maass 1999). An interesting method is proposed by Vuskovic to determine in a noninvasive way the values of the elastic coefficients used in the laws of behavior (Vuskovic 1999a, 1999b, Vuskovic 2000, Kauer 1999). They apply an instrument at a point, which appears as a prolonged tube of a handle, which can be used as well in open surgery, in laparoscopy, or at the time of ex-vivo experiments. The principle is to place the end of the tube on the surface of the trunk, and to exert a suction force there. Then a part of the trunk is absorbed towards the interior of the tube, and a camera records the profile of the deformation. Their results will be followed to see if they can be used for our further modeling.

Deformable models, based on the elastic laws Neo-Hook and Veronda-Westmann (Veronda 1970, Fung 1993), are used to simulate the same experiment. Then the coefficients of these models are adjusted so as to find the same deformation exactly. Unfortunately, the latest publications state only preliminary experiments carried out on the kidney. However, they obtain values of the Young's modulus between 500 and 800 MPa, which corresponds rather well to the values suggested by other teams.

2.5 Objective

The first objective of our project was to predict the long term effect of brace treatment on the patient's trunk, which required building a system to show a consecutively dynamic procedure of deformation. The external force from the brace is also a variable over time. This first motivation was the principal reason for considering a dynamic system.

We did not use an existing FEM software package, such as ANSYS, because our algorithm permits us more flexibility in the adjustment of time, force and the displacement of constraint points during deformation. Furthermore, we can add the constitutive model of a new material to more appropriately simulate the behavior of biological tissue.

Our global objective is to develop an integral deformable model to build a physical model of the human trunk, integrating soft tissue with the bone structure to simulate the effect of surgery on the external shape of the trunk. This would provide doctors a visible environment of surgical simulation before surgery and simulate the effect of different surgical schemes, and also help the doctor to devise a better treatment strategy. The overall goal is divided into the following detailed objectives:

1. Analyze and enhance manually the quality of the acquired 3D mesh of the integral trunk to avoid bad elements and improve the simulated result.
2. Develop and validate a dynamic finite element algorithm to simulate the procedure of deformation of the patient's external surface over time.
3. Compute the boundary conditions based on anatomical landmarks on the vertebrae before and after surgery.
4. Validate our algorithms and error accuracy by comparing our simulated results with theoretic values and ANSYS software simulated results.
5. Define and measure the error distance metric which is used to evaluate the model from real data for one patient.

CHAPTER : 3 METHODOLOGY

This chapter gives detailed implementation schemes. At first, acquisition of data is described and three types of data, internal spine and rib cage, external surface before surgery and some key points on the spine after surgery are presented. Finite element construction discusses the discretization problem and its basic assemblage.

One type of nonlinear hyperelastic material with different properties is used to construct different parts of the human trunk which includes three types of materials: bone, ligament and soft tissue in our model. The hyperelastic Saint Venant-kirchhoff finite element model is used to construct different parts of human trunk. The main reason is that its biomechanical parameters directly come from Young's modulus and Poisson's ratio which are popularly used in mechanics so that we can acquire the accurate parametric value of bone, soft tissue. In the solution of dynamic equation, there are two types of integration methods (explicit and implicit). Implicit method is adopted for its accuracy and stability. Finally, we describe the validation methods which are implemented to estimate the error compared with the deformation of clinic scoliosis patient.

3.1 Acquired data

3.1.1 External surface from InSpeck system

A recent development allowing acquisition of the human trunk surface is the 3D Capturer equipment of InSpeck. This system is compact, portable and easy to use. Conceived for the digitalization of objects of free form, the 3D Capturer acquires geometrical information in 3D as well as texture color of surface, with volume of 1100x800x800 mm (Figure 3.1). This optical non-contact digitizer without contact can carry out an acquisition in 0.3 seconds. The reconstruction of the surface uses the principles of interferometry (Moiré projection and triangulation). In fact, a halogenous lamp emits white light through fringes on the surface to be measured. A CCD camera

acquires the information and the co-ordinates of points on surface are obtained by triangulation. The following figure shows a basic InSpeck set-up which comprises three cameras in different directions connected to a control computer.

Figure 3.1: InSpeck Digitizer with four cameras

We use InSpeck cameras to obtain the external surfaces of a scoliotic patient's trunk which modeled using polygons. Figure 3.2 shows the external surface of a specific scoliotic patient's trunk which has been constructed and triangulated by InSpeck system. The patient's external triangularized surface model comprises 49,470 points and 98,401 triangles.

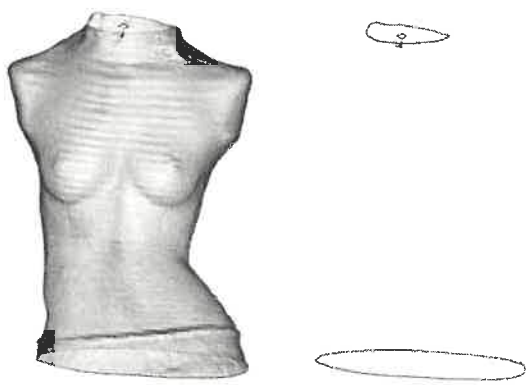

Figure 3.2: Patient's external surface reconstructed by InSpeck

There are some defects on the surface, for example, it is not a closed surface, and there are two large holes on two ends and some small holes, which come from the surface reconstruction technique of InSpeck.

3.1.2 Internal surface

Since an external surface only is not sufficient, further meshing which contains some internal organs will be implemented to obtain a whole trunk which only includes one form of tetrahedron finite element. For that, we must acquire the structural information of certain internal organs and combine internal and external meshes to form a more realistic deformable trunk model.

The X-ray apparatus below is used to attain a patient's PA0 and LAT radiographic images, on which anatomical landmarks are manually identified. Finally, anatomical primitive free-form deformation is performed based on these control points to reconstruct the 3D spine and rib cage model (Figure 3.4).

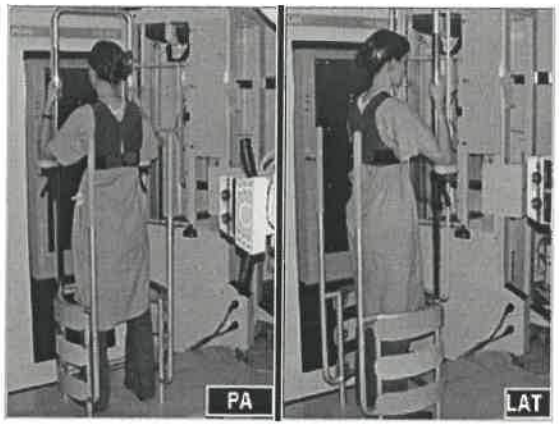

Figure 3.3: Acquisition of X-ray image

Figure 3.4: Deformable personalized rib cage

But since the data, which only represents the object's surface, is not of the type we need, the remeshing procedure has been done to transform the surface polygon mesh into a tetrahedral mesh, maintaining the external shape. At the same time, the experimental parameters which are used in the Ste. Justine model, representing mechanical properties of bone, are also retained.

In the context of the finite element method, the more vertices and elements that are applied, the more accurate is the approximation. But too many vertex and elements increase the computation time and memory use of the computer, so that the vertices can not increase without limitation. Because our project is built on single 32 bit architecture machine and the memory is 640M, we can not process meshes with too many vertices and elements. After some tests, the number of vertices of the meshed object was reduced to less than 30,000 so that the method could run in a reasonable amount of time. 30,000 points are accurate enough for our current trunk mesh and running time is several hours with ten iterations in the nonlinear dynamic integration solution. In summary, our final mesh should have less than 30,000 vertices, i.e. 90,000 variables.

3.2 Finite element model of trunk

The following stage consists of discretizing the elastic problem in order to allow the calculation of a numerical solution. At the time of this discretization, it should be possible to apply to the model a set of constraints on the boundary. In our case, the boundary condition is defined on the internal points which move along specified paths by displacement or applying forces to them, so that external surface can correspondingly change under the interaction of internal forces during deformation.

When we exert forces on some special internal points, the forces will propagate inward and outward until they reach the external boundary and form a dynamic equilibrium on boundary. We can also obtain the distribution of all forces on the whole trunk mesh.

The first thing to be done is to assemble the global stiffness matrix of the system starting from the elementary stiffness matrices of the vertices and the edges. Once this matrix is assembled, the problem can be written in the form $[K]u = F$. This matrix K is of dimension $(3N \times 3N)$ where N is the number of vertices of the mesh. The whole system contains 3N unknowns and 3N equations, which express the internal elastic forces exerted on each vertex of the mesh according to the local field of displacements. The displacement u of the vertices of the grid is then obtained by solving the system using the direct factorization or iterative method. It should be noticed that the matrix K is sparse since the elementary matrix is non zero only when there is an edge connecting the vertex. The sparsity of the matrix generated by the integrator is best represented in block-fashion: for the system with N vertices, we deal with a $3N \times 3N$ matrix, whose non-zero entries are represented as dense 3×3 matrices of scalars. The matrix is represented as an array of $3N$ rows; each row is a linked list of the non-zero elements of that row, to accommodate possible run-time changes in the sparsity pattern. The (dense) vectors that are multiplied by this matrix are stored simply as n element arrays of three component vectors.

Generally, in a regular tetrahedral mesh, each vertex is only connected to ten edges. It is important to consider this property, in order to optimize computing times, by using data structures adapted to sparse systems.

Finally, the data necessary to calculate the forces are directly stored in a data structure related to the grid. In our case, we have built a data structure containing vertices, edges and tetrahedrons. For each tetrahedron, we store the list of its vertices and edges, each vertex with its current position, and the elasticity constants E and υ. We also have a triangle concept to represent the surface of the grid. In this case, each external face knows the tetrahedron to which it belongs, as well as its three vertices. This concept of triangulation of the surface makes it possible to calculate the normal more efficiently, which will be useful for rendering the object and for calculating the integration of external forces on the surface. They will also be useful to model contact with other surfaces and external objects.

We use the laws of deformation deriving from the mechanics of continuous media to exhibit the biomechanical behavior of the human trunk in order to guarantee the physical realism of its behavior. The linear elasticity produces a good efficiency and makes it possible to apply several methods of acceleration and optimization. Moreover, the relative simplicity of the equations that it generates allows an intuitive interpretation of different behaviors, which makes it possible to make many improvements there. In linear elastic deformation, since the stiffness matrix, the inversion of which costs most of computation time, remains invariable, we only compute it one time at the beginning of the deformation. Furthermore, the boundary condition is easily added to the linear stiffness matrix.

3.2.1 Derivation of boundary conditions

In order to obtain non-trivial solutions of the dynamic equation, some special boundary conditions which are described as displacement and external forces are included in our project. In scoliotic surgery simulations, the forces during the surgical impact are usually unknown but the vertebral moving position in surgery can be recorded. Thus, in this

work, two kinds of boundary conditions are implemented. These boundary conditions are exclusively given by the prescribed displacement curve and force value and direction. They are determined by the comparison of many key points on the spine between pre-surgery and post-surgery and the intermediate values are obtained by interpolation method.

To begin, a series of points which are located on preoperative and postoperative vertebrae are got by radiography as in following figure. The red points are related to preoperative and the green points are postoperative points. Each point among them is accurately computed and matched as the same point on the undeformed and deformed spine. The points are used to deform the pre-constructed spine model to match the particular patient's spine. Six anatomical landmarks are used to define one vertebra, one on the center of the superior endplate, one on the center of inferior endplate of vertebra, and four on the superior and inferior tips of the left and right pedicles, as in the following figure, where two points define the superior and inferior centers of plate of the vertebra.

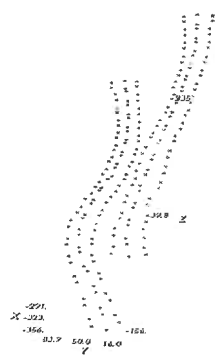

Figure 3.5: Points on preoperative and postoperative vertebrae

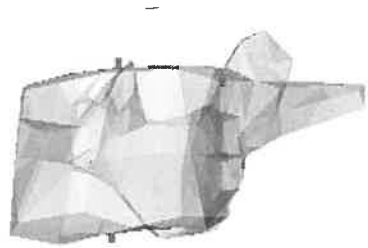

Figure 3.6: A vertebra defined by six points

The points of the tetrahedral mesh are matched with points of radiograph. From radiography, we acquire a dataset which describes the whole internal rib cage and the spine of patient with each six points per vertebra, sixty points per a rib, and four points per sternum. The points are used to construct the patient's internal surface structure. But unfortunately, the constructed patient does not have the preoperative points on the pelvis, so that the model does not contain the pelvis. The following figure displays the patient's tetrahedralized rib cage mesh and the points which are used to locate the position of each vertebra and rib.

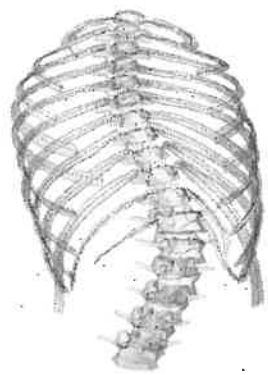

Figure 3.7: Rib cage and points of radiograph

The tetrahedral mesh of the spine and the rib cannot map any spatial point to its vertex because it has been attained by deforming the high-resolution surface model and reducing the number of its vertices to 9,464, to reduce computation time and memory. However, in implementing the FEM, all displacement and force application must be appropriately switched to operations on vertices of the mesh. So we associate each red point to the point of the tetrahedral mesh closest to it.

In scoliotic surgery, the doctor corrects the deformed spine by instrumentation and fusion which are not operations on rib. Second, we do not have the postoperative points on rib cage so that we have no information about the postoperative position of rib cage. Consequently, we do not implement any force and displacement on the rib, but only on the spine. So, the following procedures are performed:

- Remove all red points which are used to define the rib and sternum, except the red points relative to the spine which have 102, six per vertebra;

- Locate the vertices on spinal mesh most closing to each red point.

As the figure follows, each red point is mapped to a vertex (blue) of the mesh to which the displacement or force is applied.

Figure 3.8: Spatial points (red) are mapped to vertices (blue) of mesh

In searching for the closest points, owing to the resolution of the tetrahedral mesh, some spatial points may have the same closest point on the mesh. In our experiment, we find there are two points having the same close vertex. We apply the algorithm that when a spatial point (red) finds a closest point which has been matched to a previous one, the point is mapped to the next closest vertex.

3.2.2 Derivation of displacement

Although two preoperative and postoperative point datasets have been acquired, they are not the vertices on the spinal mesh. We need to define the displacement of points on the spinal mesh. To begin, we compute the vector of each pair of points between pre- and post-surgery and display those on the following figure, where the red points define the preoperative points, and the green define the postoperative points. The green lines describe the moving curve of points. But, because the red points are not vertices on the mesh, we need to reevaluate another set of points and the displacement track.

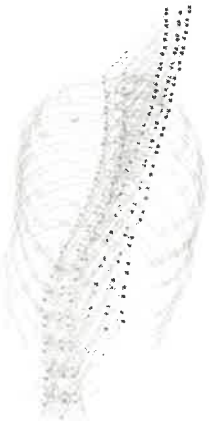

Figure 3.9: Definition of displacement

The vectors which are estimated through the preoperative and postoperative spatial points are used to compute the displacement of vertices on the mesh. As illustrated in the following figure, A and B are the accurate preoperative and postoperative points from a radiograph and the point C is the vertex closest to A on the mesh. The actual displacement vector AB is applied to the point C and makes C moving the same relative vector CD to point D.

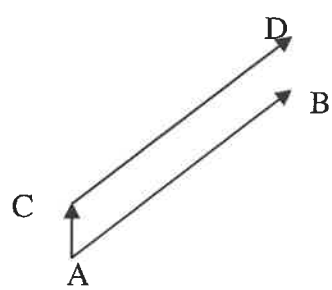

Figure 3.10: Evaluation of displacement

The actual displacement points on the tetrahedral mesh are different from the measured data on the radiograph. The following figure shows the displacement (yellow) of the vertices of the mesh and the moving trail (green) of their associated points.

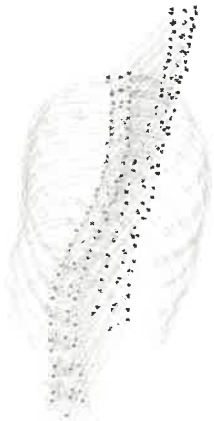

Figure 3.11: Trail of displacement of vertices of mesh and relevant points

The deviation distance between each pair has been computed and is shown on the following histogram, and some statistical properties are listed in table 3.1.

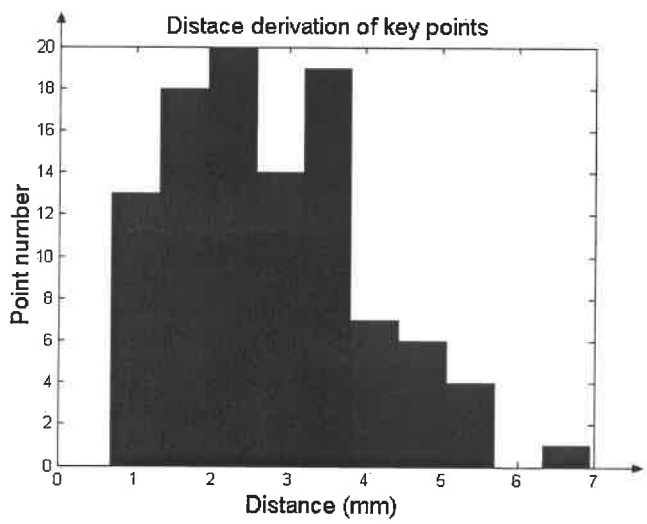

Figure 3.12: Histogram of deviation of key points

Table 3.1: Deviation of key points

Number of points	Maximal distance (mm)	Average distance (mm)	Standard deviation of distance (mm)
102	6.95	2.7872	1.2528

3.2.3 Selection of displacement step

There are still two questions that remain to be answered: how to obtain the initial guess and how far to proceed in a selected displacement direction. In our first case, we define the displacement boundary conditions which completely determine the deformation of the surface of the human trunk. At first, the initial configuration x=0 is given so as to avoid an illegal configuration where a special tetrahedral element whose orientation is reversed may be contained in mesh. For the same reason, the displacements of constrained components are not suddenly applied to reach the final balance status. They are gradually incremented based on a linear time function schedule, as shown in the following figure:

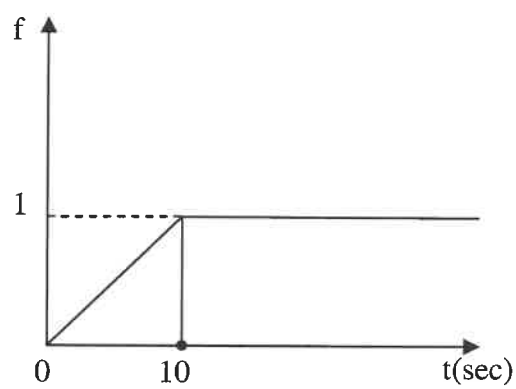

Figure 3.13: Displacement function

At time zero, the object has static balance status without any constraint condition and then the displacements of all constraint vertices (102 points) are gradually changed to reach the final position at the tenth second in time. In the time schedule, we choose one second as a time step and iterate twenty time steps so as to guarantee that the dynamic equation can attain the final static equilibrium.

3.2.4 Application of force

For some points, instead of displacement, we apply forces on the boundary points on the spine to deform the soft tissue. The implementation of force application is based on the following considerations which relate to situations observed in the nonlinear solution:

- Illegal configuration: in the solution of pure displacement of boundary points, when the displacement of equal distance is applied at each iteration, the configuration in the solution of nonlinear finite element often leads to an illegal configuration in some intermediate time steps because the equal displacement of each point is unrealistic. As shown in the following figure, in (a), ABCD configuration satisfies the right-hand rule which does not produce a negative gradient, but at next step, since the A point moves faster than other three points and goes to the other side of the BCD plane, the tetrahedron is reversed and its negative gradient prevents the assembling of the gradient matrix.

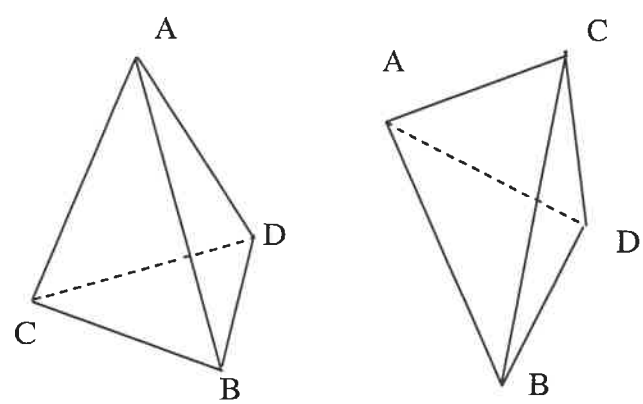

Figure 3.14: (a) Normal tetrahedron (b) Reversed (illegal) tetrahedron

This phenomenon persists even when the time step is reduced and the displacement curve is adjusted. The main cause derives from the unreasonable definition of the displacement path. However, the illegal configuration does not occur in linear finite element system, because of the linear motion of all points. So in linear deformation, the pure displacement and force application on each particular point can be implemented,

but in the nonlinear system, only force application is given because the illegal configuration of tetrahedron which happens in solving procedure, prevents reaching the final stable status in the application of pure displacement.

- Realistic and robust: displacement constraint often makes a deformable object move in an artificial environment and the special points reach a particular position at each step which do not exist in reality. If the constrained point coordinate at each step can be determined by a specialist or acquired by actual measurement in surgery, the deformation procedure is reasonable and can be accomplished. Conversely, if the moving curve of constrained point is randomly defined, as in our experiment, to equally discretize the line between the beginning and the final position of each point, the deformation may exhibit a kind of artificial design, and may even go into an impossible state such as the intersection of two tissues during the deformation. However, application of force on each point does not enforce the point to move strictly to a special point at the next step and makes deformation smoother and realistic. During the deformation at each step, the position of each key point is adjusted by the dynamical spring force with different distance so as to avoid the inversion of the tetrahedron. When the incremental step continues, the solution is cascaded into the next step if some key points do not move to ideal position at the last step.

Given the final positions of the boundary points, a kind of traction force on each point must be designed to make the special points move toward its final position. For each force, we must dynamically compute its value and direction at each time step. Based on the characters that their positions are uncertain at each step, we apply the force of spring form on boundary points. As the following figure, one end of spring is fixed on the vertebral vertex and its another end moves along a straight line form A to C by B which is defined by the beginning and final positions of boundary points. Such scheme guarantees the vertices (A) on vertebra always move toward the final boundary points (C) wherever they are during deformation.

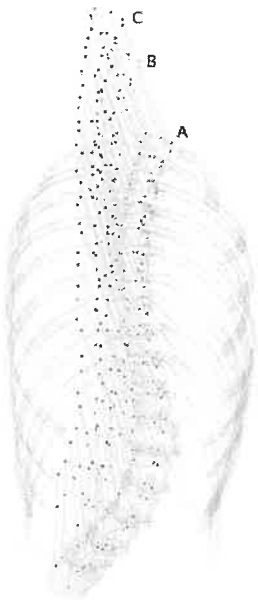

Figure 3.15: Construction of spring force

During deformation, spring constants must be carefully specified because this is a very sensitive factor in influencing the final accuracy. In principle, the bigger the spring constant, the closer to point (C) is the final position of point (A) and the more accurate is the result. But, two aspects must be considered in the numerical solution of the differential equation: if the forces produced by the spring are very large, the solution may be divergent and to make it convergent, the time step must be correspondingly reduced. In some reasonable range where the computing time is acceptable, we can reduce the time step and increase the spring constant to improve the solution accuracy. At the same time, the too strong spring force also causes the same illegal configuration as in the application of pure displacement.

In the application of forces on points, to reduce the probability of divergence which is caused by the abrupt and non-continuous force, we designed a scheme that makes the force gradually increase and be smoother. Like the application of displacement, we slowly move one end of the spring along line (AC) and adjust the speed of motion of point (C) to control the value of force on vertices (A) on vertebra. Considering the computation time and the accuracy which is influenced by the time step, especially in the

nonlinear case where one iteration takes about twenty minutes in our computer (1.4 G CPU 512M Memory), we choose ten iterations and equal linear interpolation on line (AC) in time interval of ten seconds to move point C, whose motion function is shown in following figure:

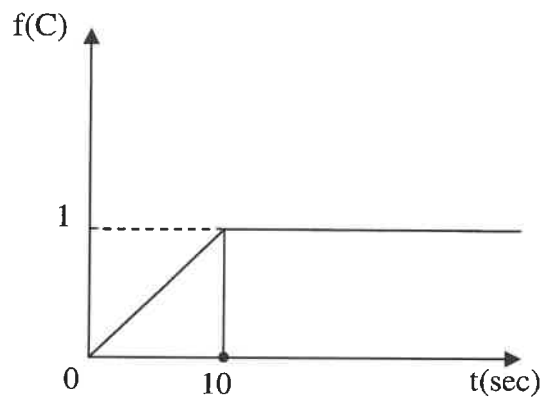

Figure 3.16: Spring moving configuration

Based on the above scheme of spring motion, we try to use spring constant as large as possible because increasing its value will reduce the error between the final position of point A and point C, which is in accordance with the actual physical position deriving from radiograph. Since the biggest Young's modulus in our project is associated with the vertebra, with the value 5000 (10^6 N/m^2), after testing and adjustment of time step under the convergence and comparing the accuracy of the final error, we chose 10 (106 N/m) as the spring constant so that its produced force was sufficient to cause the deformation of spine. The error between the final position of point (A) and the ideal position (C) is given in Chapter 4.

3.3 Solution and construction of dynamic equation

After obtaining the basic relationship between the displacement and the stress force, we must construct a dynamic equation to describe the dynamic procedure of deformation. In

the following section, we use the Newmark integration method to form the dynamic equation and describe some techniques to accelerate and enhance the convergence of solution.

3.3.1 Integration algorithm

We used the Newmark integration algorithm which is described in Appendix A. Since we are simulating biomedical tissues, the natural frequency is usually not large. Therefore we can use relatively large time steps to acquire stable simulations. (Zienkiewicz 2000a) shows that lumping can even improve accuracy for some problems, by error cancellation. It can be shown that in transient approximation the lumping process introduces additional dissipation of energy and it can help in canceling out numerical oscillation. Computation of mass comes from the calculation of volume of each tetrahedron and its density which is set as a fixed constant in our simulation. However, the density can also be acquired based on relevant anatomical study. The following scheme expresses the Newmark integration procedure we used:

1. Initial conditions and initialization of parameters:
2. Set $u^0, \dot{u}^0, \ddot{u}^0 = 0, n = 0, t = 0$; compute mass M matrix, specify integration parameters β and γ
3. Calculate integration constants:

$$b_1 = \frac{1}{\beta \Delta t^2}, \quad b_2 = \frac{1}{\beta \Delta t}, \quad b_3 = \beta - \frac{1}{2}, \quad b_4 = \gamma \Delta t b_1$$
$$b_5 = 1 + \gamma \Delta t b_2, \quad b_6 = \Delta t(1 + \gamma b_3 - \gamma)$$

4. For each time $t = \Delta t, 2\Delta t, 3\Delta t \cdots$
5. Compute dynamic stiffness K and damping C matrices
6. Form effective stiffness matrix $\overline{K} = K + b_1 M + b_4 C$
7. Calculate effective load vector:

$$\overline{F}^{n+1} = F^{n+1} + M\left(b_1 u^n - b_2 \dot{u}^n - b_3 \ddot{u}^n\right) + C\left(b_4 u^n - b_5 \dot{u}^n - b_6 \ddot{u}^n\right)$$

8. Compute Jacobian $J(u)$
9. Modify $J(u)$ for essential boundary conditions
10. Solve for node displacement vector $\Delta u = -J^{-1} R$
11. Calculate node velocities and accelerations:

$$\dot{u}^{n+1} = b_4\left(u^{n+1} - u^n\right) + b_5 \dot{u}^n + b_6 \ddot{u}^n$$
$$\ddot{u}^{n+1} = b_1\left(u^{n+1} - u^n\right) + b_2 \dot{u}^n + b_3 \ddot{u}^n$$

12. Update displacements, counter and time:

$$u^n = u^{n+1}, \dot{u}^n = \dot{u}^{n+1}, \ddot{u}^n = \ddot{u}^{n+1}, n \leftarrow n+1, t \leftarrow t + \Delta t$$

13. Check energy balance
14. Output; if simulation not complete, go to 3.

Figure 3.17: Algorithm of Newmark implicit integration (Belytschko 2000, p. 324)

3.3.2 Numerical methods for minimization

To solve the equilibrium equation with elastic materials of non-linear nature, a relatively robust numerical method called "algorithmically consistent tangent stiffness" is used Belytschko 2000, p. 337). To update the tangent stiffness, a continuum tangent scheme

which relates rates, or infinitesimal increments, of stress and strain, an algorithmic scheme is used to approximate finite increments of stress and strain. When the incremental stress-strain relation is obtained through consistent linearization of the stress update algorithm, the consistent algorithmic scheme can be used to update the tangent stiffness matrix.

Newton's method finds the minimum of the deformation energy function by repeatedly approximating the total energy W with quadratic functions. But, the standard Newton procedure is not suitable for the algorithmic scheme because the computation of the derivative is difficult and too time consuming. In our algorithm, we improve the stability of the numerical method by combining the secant Newton method and adaptive-stepsize incremental loading. In the secant Newton iterative method, all variables are updated from their values at the end of the previous time step, i.e., the last converged point, as opposed to at the last iteration. This avoids non-converged values of stress and internal variables from erroneously driving the constitutive equation.

3.3.3 Adaptive time step

When the constraint points on mesh gradually move, or the forces which are applied on boundary points increase, each incremental step performs a Newton iteration. Owing to the imprecision of linear approximation of the motion of constraint points and the unreasonable time configuration (ten time steps in ten seconds), some intermediate steps often go into an illegal configuration where some tetrahedral elements have reversed orientation. The illegal configuration obstructs the assembly of the stiffness matrix. A mechanism to ameliorate the situation is applied in our algorithm. During iteration, as soon as an illegal configuration is detected, the time step size is automatically reduced to half and the solution is cascaded into the next step. The detection mechanism of the negative gradient corresponding to a reversed element is repeatedly executed in each finite element assembling. As long as a reversed element appears, the time step size is automatically reduced to half until the assembling procedure is finished or the number of reduction reaches a specified value. We also apply another mechanism to accelerate the

computation: the time step is doubled when the iteration solution does not encounter an illegal element in three time steps or (a specified number of time steps).

Although the self-adaptive time step is applied to both the linear and nonlinear solver, illegal elements are not observed in the linear solution owing to the linearity of gradient assembly. It is only used in this case to improve the robustness of the nonlinear solver, to improve convergence, and to get rid of the artificial influence of the configuration in the control of the deformation path.

3.3.4 Selecting search direction and length

Nearly all solutions start with an initial guess and proceed in a given search direction in a step by step manner. Finding the proper direction in the high-dimension search space is critical for the algorithm's efficiency. Several different methods exist to determine the best direction.

The maximum gradient descent method chooses the direction of the forces (i.e. the negative of the residual for each step). This method is very slow because it takes many steps for a local force to propagate through the entire mesh. Furthermore, it is impossible for this method to predict rapid force changes caused by the deformation of soft tissue. Conversely, the Newton-Raphson method uses the derivative of the forces (i.e. the stiffness matrix), which provides information about how the forces vary as a function of deformation. Each Newton step consists of the computation of the residual, computation of the stiffness matrix, and solution of a linear system. The process continues until the residual drops below a given tolerance. The method is adopted as a basic algorithm and is associated with the line search method to improve the solution of nonlinear systems.

One must also define how far to go in a given search direction after computing the initial value. If the function is smooth, and the initial value is close to the solution, a full step towards the linear solution can safely be taken. However, the nonlinearity of the system often causes the divergence at a full step and brings the mesh into illegal configuration. Our nonlinear solution procedures iteratively search for the solution until some convergence tolerance is satisfied. The solution procedure thus involves determining the

two aspects of the search for the solution; the procedure must determine the "length" and the "direction" of the update to the current best guess of the solution.

Our nonlinear procedure uses Newton algorithm with the linear search factor $1/2$ to determine the length of the update vector. The maximum iteration number is also used to control the searching number along the update direction.

During each iteration solution, two criteria are both adopted for assessing convergence based on the norm of the residual forces. The first is an "absolute" tolerance while the second is a "relative" tolerance. The "absolute" tolerance is an indication of "small" in terms of the numerical precision displayed for a given calculation. Depending on the platform, the various formulations used throughout a calculation, and details of the implementation, the level of numerical "noise" in a calculation may limit how close to zero the solution procedure is able to make the norm of the residual. The second tolerance examines the "relative" error. This compares the norm of the residual at the end of the iteration with the norm of the residual at the first iteration. The solution procedure stops if either condition is satisfied.

In solving of nonlinear equations, divergence phenomena are universal, and their frequency is determined by various factors, of which an important one is the time step. Too large a time step leads to divergence, and too small a time step wastes too much computing time. A mechanism of automatic adjustment of time or load increment is used in the iterative solution procedure. A divergence limitation is set to determine if a time step should increase or decrease in the iterative solution procedure. When the residual exceeds the divergence limitation, which is set at 10,000 in nonlinear iteration, the solution is judged to have diverged, so, a half time step is taken before recomputing. The time step will also be increased by two if the residual is always less than the divergence limitation during the following five iterations. The algorithm is shown in the following figure:

Outer loop: Adaptive adjustment of time and load (increase or decrease time step by factor 2)

Middle loop: Newton iteration, $i = 0,1,2,\cdots$

Compute stiffness matrix K and residual R

If $\|R(u)\| < \varepsilon_{(abs)}$ or $\|R(u)\| < \varepsilon_{(rel)}$

Terminate Newton iteration

$\Delta u = -K(u_i)^{-1} R(u_i)$: Linear system solution

$u_{newton} = u_i + \Delta u$: Full Newton step

Inner loop: line search, $s = 1, 1/2, 1/4, \cdots$

If $\|R((1-s)u_i + su_{newton})\| < \|R(u)\|$

$u_{i+1} = (1-s)u_i + su_{newton}$

Terminate line search

Figure 3.18: Algorithm of nonlinear system solver

3.3.5 Linear system solution

No matter what system (linear or nonlinear) is implemented, a linear equation must be solved in the end. There are two kinds of linear system solvers (direct or iterative methods) which have their own advantages and disadvantages. The direct LU factorization with pivot solver has much higher precision than the iterative method at each solution. But it needs much computing time to decompose the matrix into LU form and solve the two triangular matrix equations. Because it is more accurate than iterative method, it is applied to our linear finite element system.

In the nonlinear finite element system, we use the Newton iteration method, which depends on the stable solution of the linear system, and the iterative method, which solves the final linear system. In the linear system solution, the accuracy of the solution is sacrificed in favor of speed. Since the degree of nonlinearity of the equation is high,

the residual is not greatly reduced by a single Newton iteration. Consequently, computing an exact solution for each linear system does not improve the convergence rate of the Newton iteration. Given a large error tolerance, iterative linear system solution methods converge more quickly than the direct method. For this reason, our linear solver in Newton iteration uses an iterative linear system solver.

The linear systems constructed in our finite element method are symmetric, sparse, and usually positive definite. Around a bifurcation point, however, the matrix of the system is sometimes not only indefinite but also nearly singular. The (bi)conjugate gradient method tends to behave in an erratic manner. An implementation of the generalized minimum residual method (GMRES) with diagonal preconditioning (Seager 1988) is both efficient and stable. The iteration is terminated when the residual has been reduced to one thousandth of the absolute value of the first computed residual. This strategy keeps the computation time for solving the linear system relatively low without slowing down the convergence of the Newton iteration.

3.4 Mechanical properties of tissue

An integral human trunk should consist of many materials with different properties which express the behavior of different tissue. To avoid the complexity of division of organs in mesh construction, and due to the unavailability of the mechanical properties of many tissues, we simplify the trunk model to three types of materials. Various parameters of material properties are assigned to tetrahedral elements in order to approximate the mechanical properties. The parameters are specified in the following table.

Table 3.2: Mechanical properties of trunk model

Component name	Young's modulus (MPa)	Poisson's ratio
Vertebra and rib bone	5000	0.30
Ligament	7.38	0.45
Soft tissue	0.55	0.30

3.5 Validation method

In our program, we have integrated many open source codes into our code to speed up our program and reduce the development time. In the solution of the linear system of linear finite element, we have used the spooles 2.2 library to solve linear systems of equations, including the direct factorization method with pivoting, which exhibits good stability.

The NOX and LOCA-object-oriented nonlinear solver package is used to construct the solving method of the nonlinear system, including Newton's method with some different linear search schemes. After linearization of the nonlinear system, the acquired matrix of the linear system is not always positive definite, and it is sometimes even singular. We used the iteration method of Generalized Minimum Residual method (GMRES) with diagonal preconditioning in the Atzec (a massively parallel iterative solver library for solving sparse linear systems) library to optimize the solution and improve the robustness of convergence of nonlinear system, but the program is only run on a single computer.

Finally, although we have obtained the simulated results in both linear and nonlinear finite element systems, the validation of the algorithm was not investigated. To validate our simulation, we carried out some experimental investigations to simulate the deformation of a real object. Some accurate and general aspects of finite element modeling of deformable objects can be gathered by studying simple objects under the impacts of predefined load.

We adopted the deformation case of a simple real beam, which is used to serve as the basis for additional evaluation and qualification of ANSYS capabilities by ANSYS incorporation. We can find the theoretical result and the result of ANSYS simulation about the deformation in the ANSYS manual. Thus, we compared our simulated result with the theoretical value, which only presents the maximal deformation displacement. We also used the ANSYS FEM commercial software to deform the object and compared the result with our deformed result under the same loading. Since ANSYS does not provide very good support for tetrahedral finite element with four vertices, we choose the ANSYS SOLID5 element which is a 3D hexahedral element with eight nodes.

The beam is designed with length l, height h, and thickness t as shown in the following figure and table. One of its ends is fixed to a wall and its other free end is loaded with an axial force, an in-plane shear force and an out-of-plane shear force, all of magnitude F. The problem is to determine the deflections ε_x, ε_y and ε_z at the free end due to these loads (ANSYS). A static deformation scheme is adopted in the three deformed models because only the final stable status is necessary to compare the results.

The geometry of the beam is described in the table below and its mechanical properties are considered as a linear material relevant to the ANSYS Solid5 element property. First we generated its mesh using hexahedral finite elements with 8 nodes that also use the linear interpolation function. Four vertices of the hexahedral finite element at the end of the beam are fixed during deformation. The other four vertices are loaded with 1 pound force separately along the X, Y and Z axes as the F's of following figure show. We applied a static scheme with one step time to our algorithm, and to the ANSYS algorithm, to respectively acquire their simulated results. Finally, we compared the difference of the deformed hexahedral mesh between our simulation and ANSYS based on maximum and average error distance.

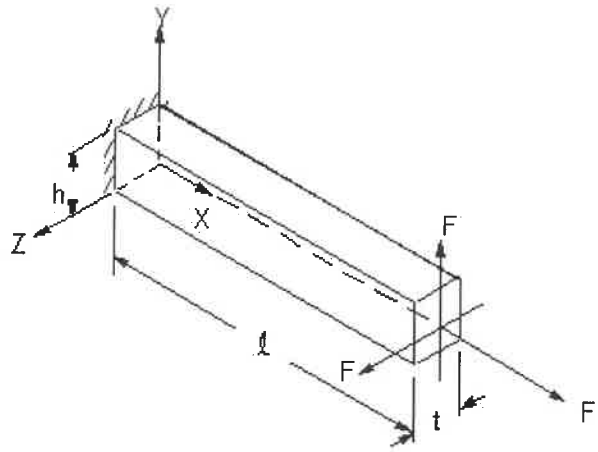

Figure 3.19: Straight cantilever beam problem sketch

Table 3.3: Parameters of deformed beam

Material properties	Geometric properties	Loading
$E = 10 \times 10^6$ (psi) $\upsilon = 0.3$	$l = 6(in)$ $h = 0.2(in)$ $t = 0.1(in)$	$F = 1(lb)$

3.5.1 Metric of error

To attain the quantitative error analysis, we computed some indices to present the difference between two surfaces: S_{posop} (surface of the trunk after surgery) and S_{sim} (deformed surface of the trunk using our model). The error evaluation is mainly based on the Euclidean distance (mm) from all the points on a surface to the other surface and is expressed in the following formulae:

Mean distance : $E_{average}\left(S_{sim},S_{posop}\right)=\dfrac{1}{N_{sim}+N_{posop}}\left(\sum_{x\in S_{Ssim}} d\left(x_{sim},S_{posop}\right)+\sum_{y\in S_{posop}} d\left(y_{posop},S_{sim}\right)\right)$

Hausdorff distance : $E_{\max}\left(S_{sim},S_{posop}\right)=\max\left(\max_{x\in S_{sim}} d\left(x,S_{posop}\right),\max_{y\in S_{posop}} d\left(y,S_{sim}\right)\right)$

Standard deviation : $S_{N_{posop}+N_{sim}-1}=\left(\dfrac{1}{N_{posop}+N_{sim}-1}\sum_{x\in S_{posop}\cup S_{sim}}\left(x-\bar{x}\right)^2\right)^{1/2}$

In our project, we have computed the nearest distance from a discrete point set to a polygonal surface, so we have used the maximum distance as metric instead of the Hausdorff distance.

CHAPTER : 4 SIMULATION RESULTS

4.1 Introduction

The aim of this chapter is to describe how to obtain an accurate simulation and to demonstrate the advantage of the proposed algorithm as a computational method in a setting reasonably close to what real data collection procedures will provide. In other words, the simulation results are meant to give a glimpse of what our computational method can offer, and to show that the final integrated model will enable the construction of accurate models of biological systems. At the same time, we have also selected one set of real data to simulate a physical deformation in order to validate our algorithm by comparing our results with results produced by ANSYS commercial FEM software and theoretical values. We also estimate how close to real deformation our algorithm and scheme are, on the real data set.

Some research on accurate values of mechanical parameters describing human tissue in the biomechanical field has been done. We selected some relatively accurate values such as Aubin's bone parameters, which have been confirmed as valid, to test and compare the effects of real deformation. By comparison of parameters in several papers, we can get some valid values.

In this section, we present the experimental results of soft tissue prediction within the spinal surgery plan. The experiments are carried out on the basis of geometrical models derived from a patient's radiographic data and her external surface, acquired before surgery. These data are approximately divided mainly into three parts to represent patient's vertebra, soft tissue and the ligaments between vertebrae, and are given different mechanical properties (this classification is very rough in comparison with the complex and delicate structure of the real human trunk). Since we have acquired the same patient's postoperative external geometric 3D surface model from the InSpeck 3D digitizer system, we concentrate our effort on the quantitative evaluation of the external geometry of the simulation. Because our model is constructed using different types of

material (linear elastic and hyperelastic) and different solution methods, we discuss them in a separate section.

4.2 Validation of model

To acquire precise error evaluation, we adopt the same real bean model which has been hexahedralized by ANSYS in the validation of our model with ANSYS software.

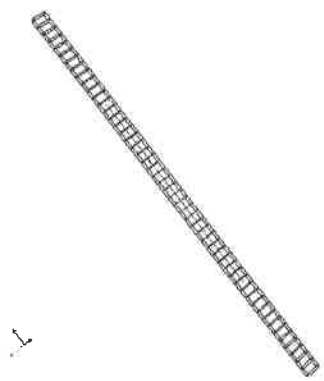

Figure 4.1: Hexahedral mesh produced by ANSYS

The above figure shows a 3D hexahedral solid mesh with Solid5 element property in ANSYS. We implemented the deformation on the mesh separately using our algorithm and ANSYS with the same loading, including application of axial and shear forces on the four nodes of the free end.

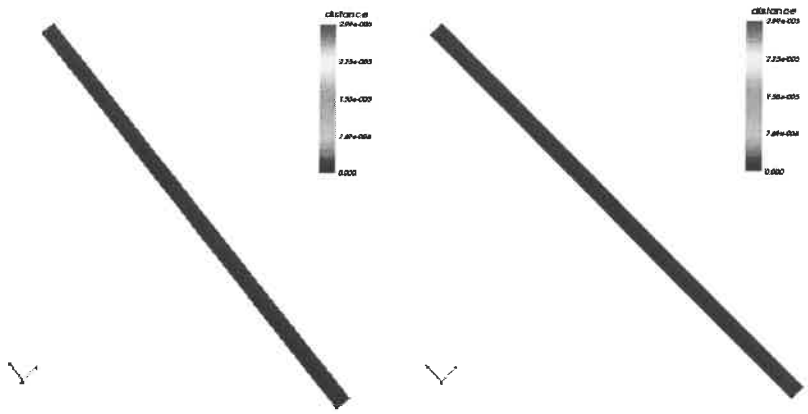

(a) (b)

Figure 4.2: Error distribution of undeformed model (a) Distance from our model to ANSYS deformed surface. (b) Distance form ANSYS deformed surface to our model

To accelerate the procedure of distance error computation and to avoid the complexity of an analytic solution and time-consuming searching algorithm, we applied numeric approximation, using the octree method to execute space searching and to approximate the distance from a point to a plane. We also set certain tolerances to control the final accuracy and computing time, which may cause some numerical error. After many experiments, we selected a tolerance value and computed the distance error between our undeformed mesh and the undeformed mesh used by ANSYS to confirm that the tolerance does not cause any error. We measure the distance error between two undeformed meshes, and we have shown their error distribution in the above figure. The results show that the error is zero on both undeformed meshes, which means the initial parameter setting has no influence on later deformed meshes.

4.2.1 Linear force application

We implemented three simulations based on the force application on the four nodes on the free end with the four nodes fixed at other end during deformation. We respectively applied different forces in each deformation, X-axis axial force, Y-axis and Z-axis shear

forces, and we show the three simulation results. The static one step implicit integration method is applied to obtain the final deformed beam. The error distance metric between two deformed objects is evaluated on each surface and their error analysis and histogram are shown in the following figure.

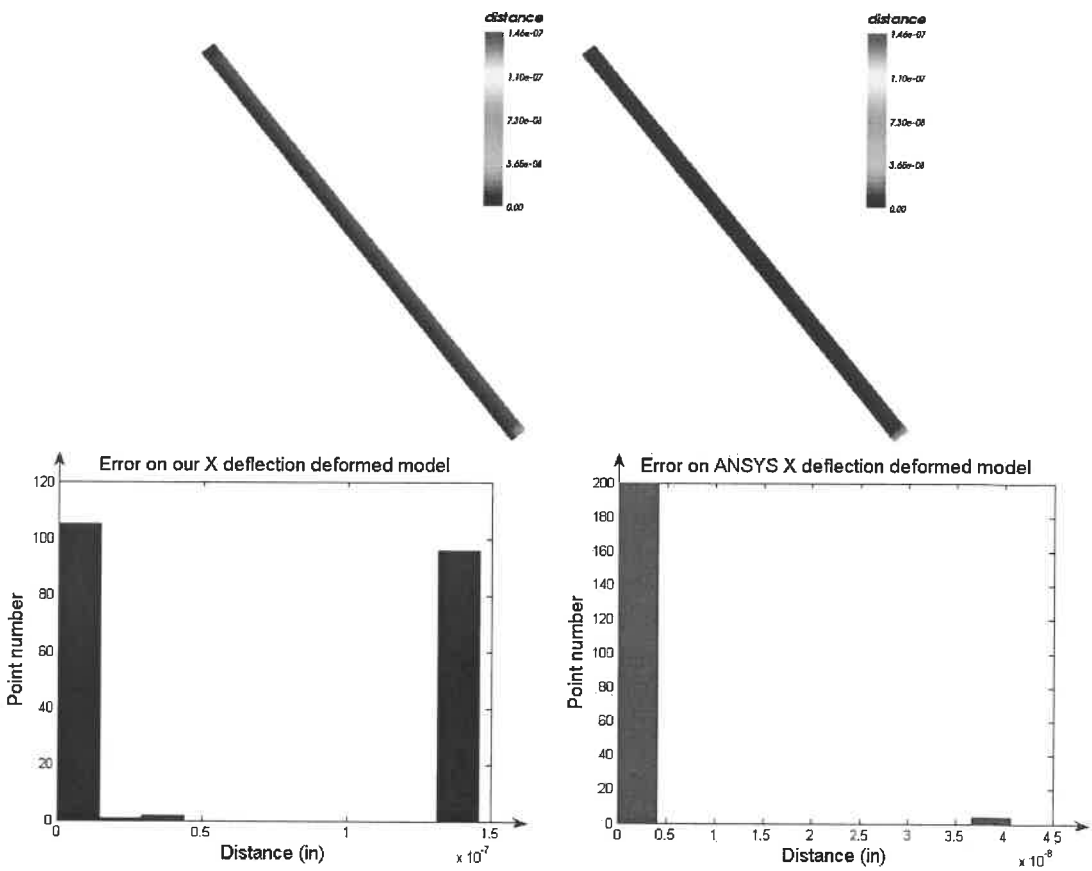

(a) (b)

Figure 4.3: Error distribution and its histogram of X-axis deflection (a) Distance from our model to ANSYS deformed surface. (b) Distance from ANSYS deformed surface to our model

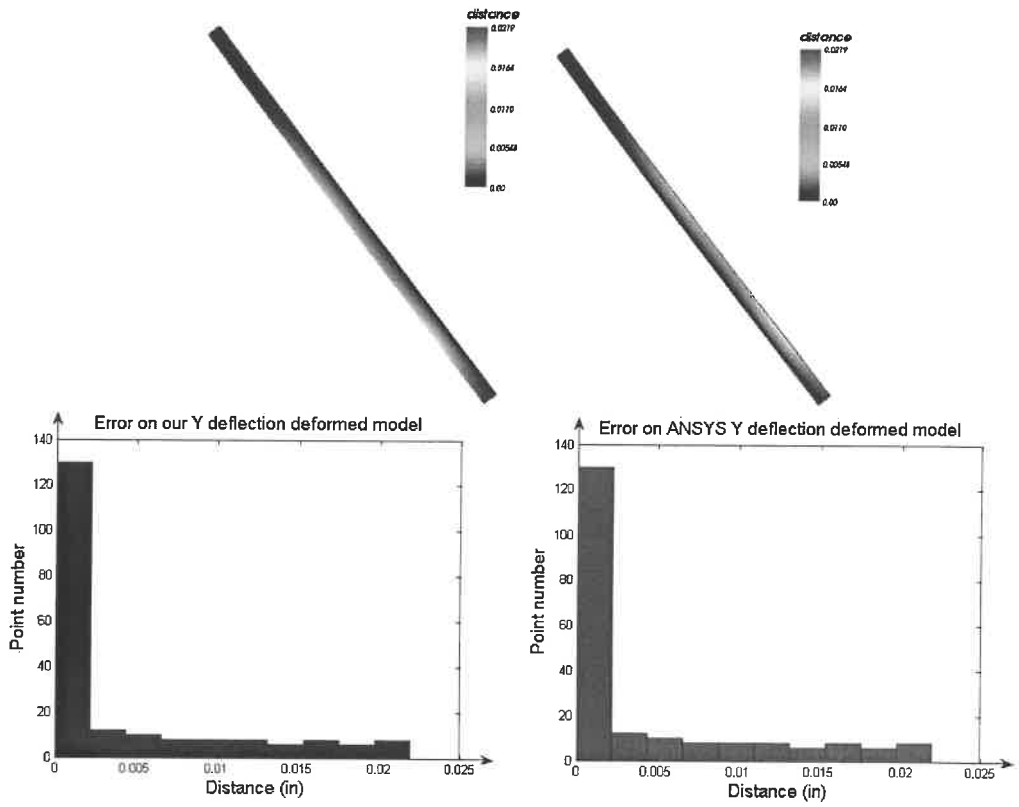

(a) (b)

Figure 4.4: Error distribution and its histogram of Y-axis deflection (a) Distance from our model to ANSYS deformed surface. (b) Distance from ANSYS deformed surface to our model

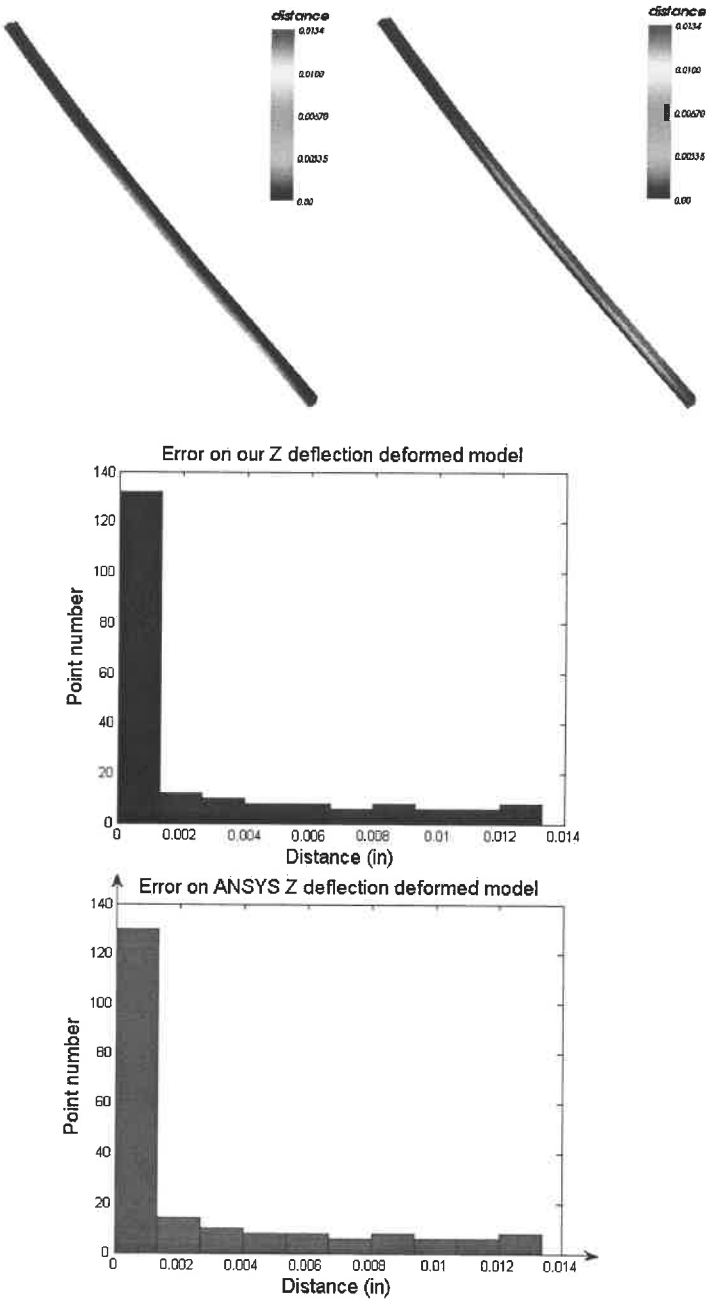

(a) (b)

Figure 4.5: Error distribution and its histogram of Z-axis deflection (a) Distance from our model to ANSYS deformed surface. (b) Distance from ANSYS deformed surface to our model

From the figure showing error distribution, we can conclude that the error is concentrated on the free end, on which the forces are applied. We will compare the quantitative error in the following section, to provide a reference to evaluate the accuracy of our system.

4.2.2 Nonlinear force application

In the nonlinear FEM application, we applied the Saint Venant Kirchhoff finite element, which is extension of linear FEM model for large displacement. In small displacement, it should approach the simulation of linear FEM model. We evaluate its deformation under the effect of external forces, which put 1 pound forces on the four nodes of the free end of the beam with the four nodes of its other end fixed. After the static one step iteration, we obtain the stable balance status and compute the error between our simulated deformed model and the ANSYS linear deformed model. The following figures show the error distribution on the surface of each deformed model and their histogram.

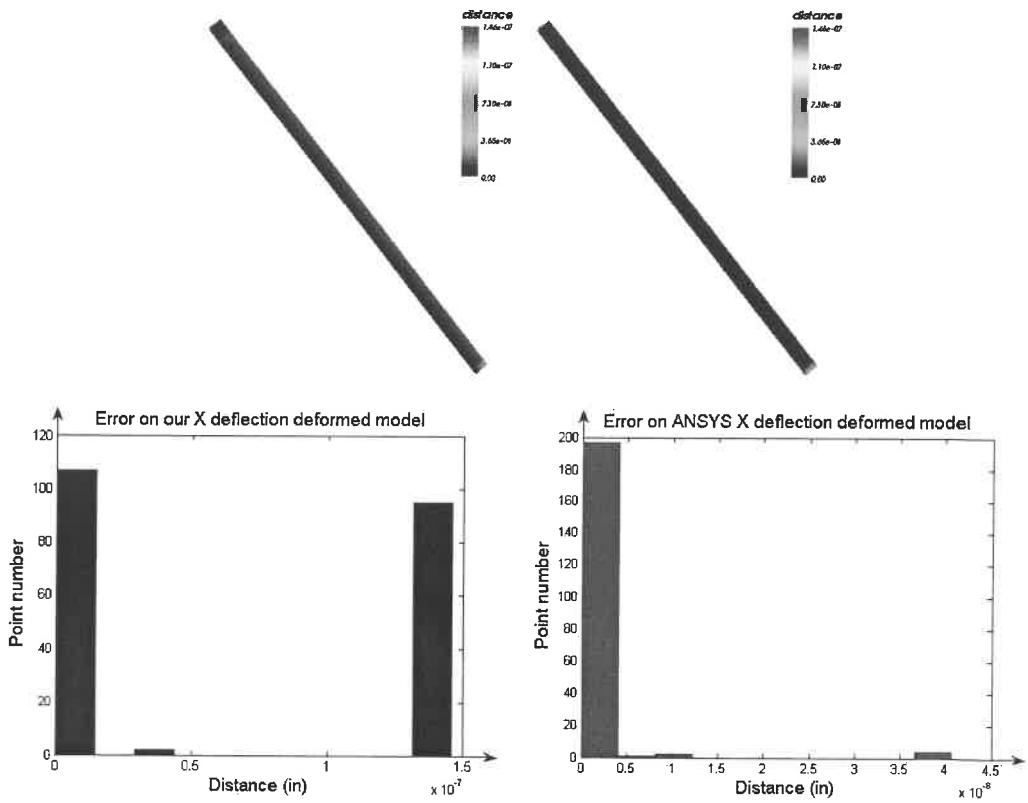

(a) (b)

Figure 4.6: Error distribution and its histogram of X-axis deflection (a) Distance from our model to ANSYS deformed surface. (b) Distance from ANSYS deformed surface to our model

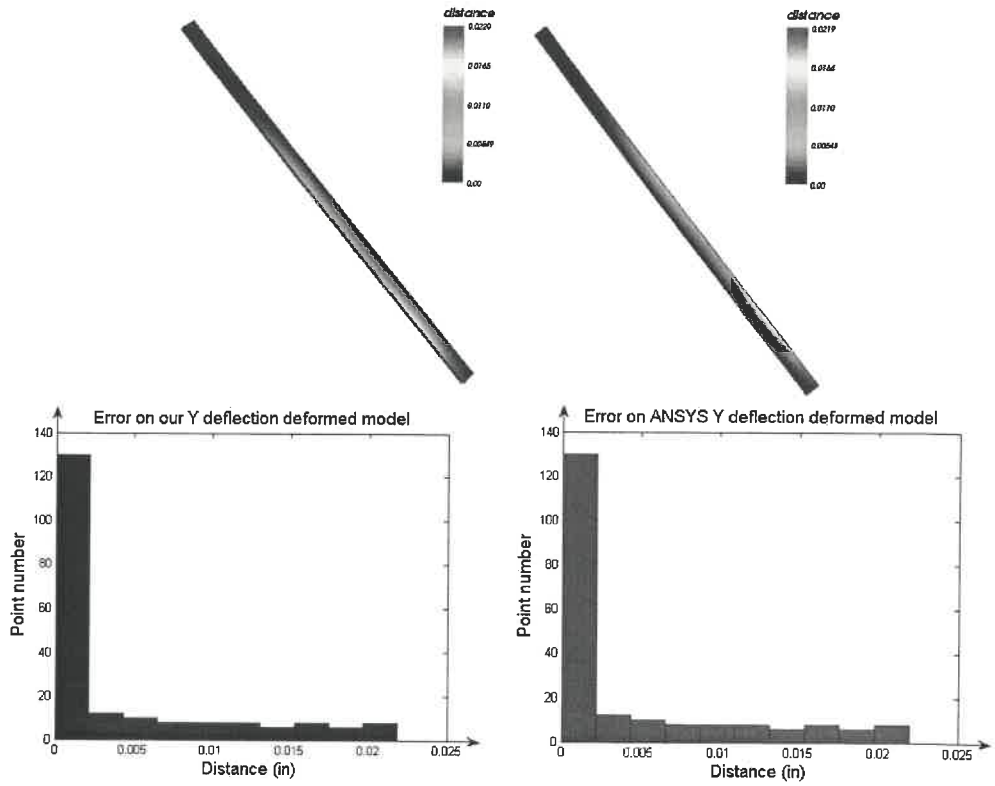

(a) (b)

Figure 4.7: Error distribution and its histogram of Y-axis deflection (a) Distance from our model to ANSYS deformed surface. (b) Distance from ANSYS deformed surface to our model

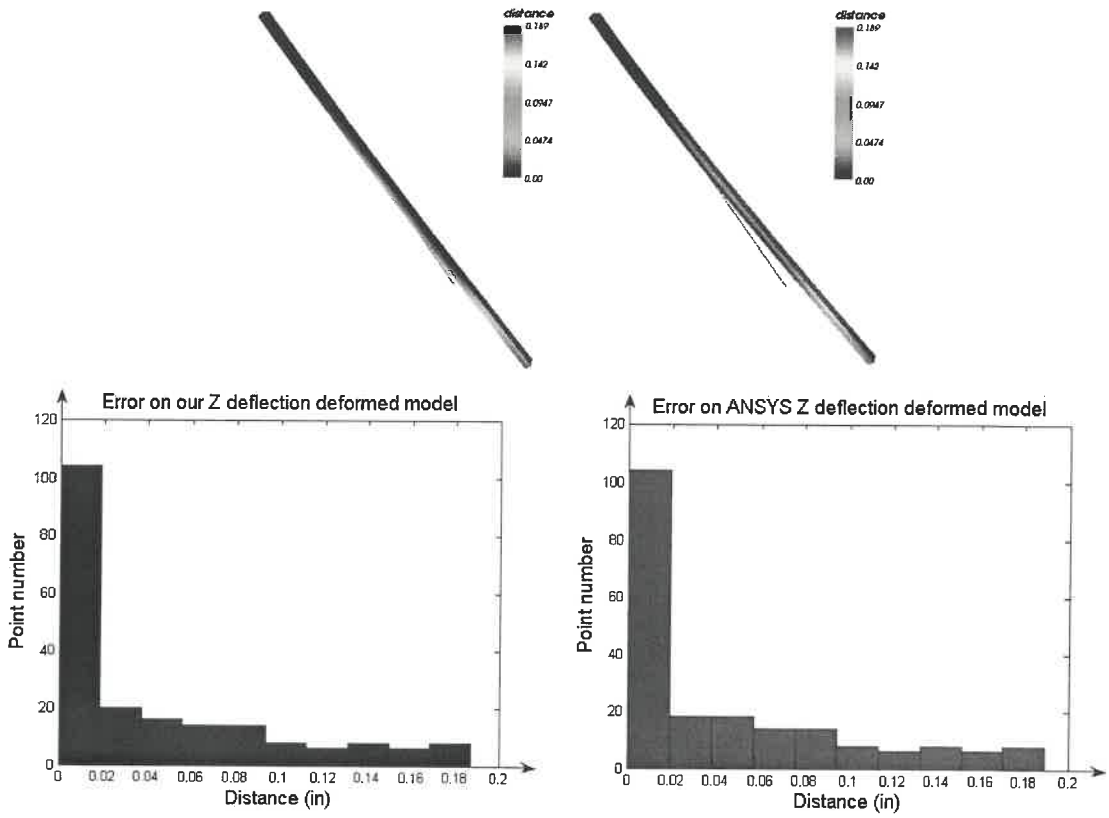

(a) (b)

Figure 4.8: Error distribution and its histogram of Z-axis deflection (a) Distance from our model to ANSYS deformed surface. (b) Distance from ANSYS deformed surface to our model

4.2.3 Conclusion

In the following tables, we present the simulated beam deflection separately along three axes using our linear and nonlinear FEM, and ANSYS linear FEM. We compute some statistical parameters to show the difference between them. In the third table, we also list the maximal distance error between our simulation and theory. Ratio refers to the simulation result divided by the theoretical result.

Table 4.1: Comparison of linear deflection simulation between ANSYS and our model

Parameters \ Method		$Deflection_x$	$Deflection_y$	$Deflection_z$
Point number	Ours	204		
	ANSYS	204		
Maximum error (in)	Ours	1.4603×10^{-7}	0.0219	0.0133
	ANSYS	4.0741×10^{-8}	0.0219	0.0133
Average error (in)	Ours	6.9327×10^{-8}	0.0041	0.0025
	ANSYS	2.3275×10^{-9}	0.0042	0.0025
	Total	3.756×10^{-8}	0.0041	0.0025
Standard deviation (in)	Ours	7.2615×10^{-8}	0.0064	0.0038
	ANSYS	5.6367×10^{-9}	0.0064	0.0039
	Total	6.1407×10^{-8}	0.0064	0.0038
Maximum displacement (in)		3.0×10^{-5}	0.086	0.4173
Relative error: Average error/maximum displacement		0.2311%	4.7674%	0.5991%

Table 4.2: Comparison of nonlinear deflection simulation between ANSYS and our model

Parameters \ Method		$Deflection_x$	$Deflection_y$	$Deflection_z$
Point number	Ours	204		
	ANSYS	204		
Maximum error (in)	Ours	1.4603×10^{-7}	0.0219	0.1872
	ANSYS	4.0741×10^{-8}	0.0220	0.1894
Average error (in)	Ours	6.8602×10^{-8}	0.0041	0.0425
	ANSYS	2.3982×10^{-9}	0.0042	0.0430
	Total	3.55×10^{-9}	0.0041	0.0427
Standard deviation (in)	Ours	7.2579×10^{-8}	0.0064	0.0534
	ANSYS	5.7019×10^{-9}	0.0064	0.0539
	Total	6.1172×10^{-8}	0.0064	0.0536
Maximum displacement (in)		3.0×10^{-5}	0.0859	0.2415
Relative error: average error/maximum displacement		0.2287%	4.773%	17.598%

Table 4.3: Comparison of maximal displacement of deflection simulation between theory and our model

	$Deflection_x$ (in)	$Deflection_y$ (in)	$Deflection_z$ (in)
Theory	3.0×10^{-5}	0.108	0.432
Linear algorithm	2.9965×10^{-5}	0.8593×10^{-1}	0.41731
Ratio of linear	0.9988	0.7957	0.966
Nonlinear algorithm	2.994×10^{-5}	0.8594×10^{-1}	0.24151
Ratio of nonlinear	0.9983	0.7957	0.5591

From the above tables, the error between the algorithm of our linear FEM and ANSYS is small, and has the biggest 4.7674% relative error difference in the y-axis deflection simulation. In the comparison with theoretic maximal displacement, the ratio is only 0.79. But, in the simulation procedure, we find that when we increase the fineness of the mesh, which means using smaller finite elements, the simulated value gradually approaches the theoretic value.

In our nonlinear FEM comparison with ANSYS linear FEM, when the deformation is very small as in the case of x-axis and y-axis deflection, the simulation of our nonlinear FEM is close to that of linear FEM. But in the z-axis deflection simulation, we found a much bigger difference, the 17.6% relative error with ANSYS and 0.5591 ratios with theoretic value of linear FEM. This is mainly because the z-axis deflection is a large deformation with 0.417 inch displacement compared with its 0.1 width. The results also confirm that our nonlinear FEM algorithm is correct and its simulated result is within an acceptable tolerance.

4.3 Patient's model

We have obtained the radiographs and the surfaces of a scoliotic patient's trunk before and after the surgical correction of her spine. We used the model of her preoperative trunk to deform and simulate her postoperative trunk. To evaluate our results, we

compared our simulated result with her clinical data. In following section, we describe the collected mesh data of the patient.

4.3.1 Patient's real surface after surgery

After patient's surgery, her external surface is directly acquired from the InSpeck machine, which gives a triangulated surface; also, key points on her internal vertebrae are acquired from her radiograph. To obtain an integral model whose internal and external geometries are in accordance with a single co-ordinate system, we apply a global rigid registration method to adjust the external surface as the following figure, which will be used as a precise postoperative reference to compute the error of our simulated results.

Figure 4.9: Rigid registration

4.3.2 Patient's 3D model before surgery

In order to validate our algorithm in real data, we apply it to a patient's dataset which has been processed using some basic data rectification. Her internal rib cage and vertebra from radiograph and external surface from the 3D digitizer camera InSpeck have been registered, to form a whole human trunk. After tetrahedralizing the internal and external surfaces, we acquire a solid 3D model of the patient's trunk as in the following figure.

Figure 4.10: Patient's 3D mesh model (a) Surface (b) Rib cage (c) Ligament

Although we have the patient's 3D mesh, there exist some shortcomings because of the shortage of information on the structure of the integral trunk, which is simply made of a patient's surface, vertebra and rib cage. The blue color in the above figure shows the patient's soft tissue and surface; the green is her vertebrae and rib cage, and the red is some divided tissue corresponding to the ligament between vertebrae and rib cage. According to anatomy, the ligament should be a kind of heterogeneous material in different directions and its properties and structure are different in different positions. Since the ligament data is unavailable from the deformed the rib cage model, and to reduce the difficulty in meshing of accurately dividing the different ligaments in different junctions, we separated a part of the area around the vertebrae as the ligament, which is considered as homogeneous material, and assigned general material properties to it.

A trade-off between the availability of data and the accuracy of trunk structure has been made. The green part in above figure (a), which belongs to the rib cage, has broken through the surface, which is not reasonable. The error mainly comes from four sources:

1. The collection of radiographic internal and surface data occurs at different times. Because of that, the internal and external data are not completely consistent although the patient tries to keep a fixed posture when the data are captured.
2. The influence of respiration: when the patient respires, her trunk's internal organs and the external surface all move. When we put the data into a whole trunk, their

inconsistency causes the unconventional phenomenon that some bone is outside the skin.

3. The accuracy of the registration method: the accuracy of the thin plate spline registration, which is used to synthesize internal and external mesh, depends on the accuracy, position and number of marks on surface, the position of the marks is not very precise and their number is limited, so that the approximation method introduces some error.
4. The approximation of the rib cage and vertebra: the patient's internal model is created by deforming a standard model of a normal human rib cage. The reference points are placed on it, as the basis of deformation, are introduced by manual insertion of points on a radiograph. The procedures and approximation of the internal organ causes the internal mesh not to match the patient's actual organ accurately enough so that there is inconsistency between the internal and the more precise external mesh.

We have two options to deal with this problem: cutting the rib outside the surface and making the external surface closed, which holds the human anatomical structure and loses some internal information of the rib; or leaving the bone outside of the skin, retaining all geometric information from acquired data. We choose the second scheme to keep all data information although the mesh violates the conventional human anatomical structure.

4.3.3 Mesh quality analysis

For the finite element method, the simplicial elements of the mesh should be well-shaped to ensure accuracy and stability of the solution. Large angles reduce interpolation accuracy. Small or large angles increase the condition number of the stiffness matrix. Poorly conditioned elements slow down solvers and introduce large round-off errors. To reduce the bad elements, a metric must be defined to evaluate the mesh quality. The metric is defined as:

Aspect ratio = r (radius of circumscribed sphere)/R (radius of inscribed sphere)x3. This means that the minimum (and ideal) quality ratio is 1.0 for regular tetrahedron, i.e. where all sides are of equal length. Conversely, larger values indicate poorer mesh quality.

A traditional method based on histograms is used to address grid quality assessment. It gives the mesh a statistical sense of cell quality throughout the entire domain. We apply the color distribution on each tetrahedron to indicate the mesh volume and quality, and a histogram to show their statistical character.

In the following figure, the tetrahedral volume of the meshed trunk model varies from $1\times10^{-4}\left(mm^3\right)$to $3.5\times10^{3}\left(mm^3\right)$ which is very unbalanced. Its histogram shows there is a small quantity of tetrahedrons with large volume. The extreme unevenness of the distribution should be reduced after some processing (merging and subdivision of tetrahedron). Figure 4.12 also shows the distribution of the aspect ratio which is mainly concentrated in range ($1\sim1.8\times10^{4}$). But a few tetrahedrons have a bad ratio (> approximately 3×10^{6}) which indicates the tetrahedrons have a very thin and long shape. They are mainly in the region where the trunk surface and the bone intersect and there has been a poor match between surface triangulation of trunk and bone. Consequently, we manually regulate the bad tetrahedra when they severely influence the progress of equation solution.

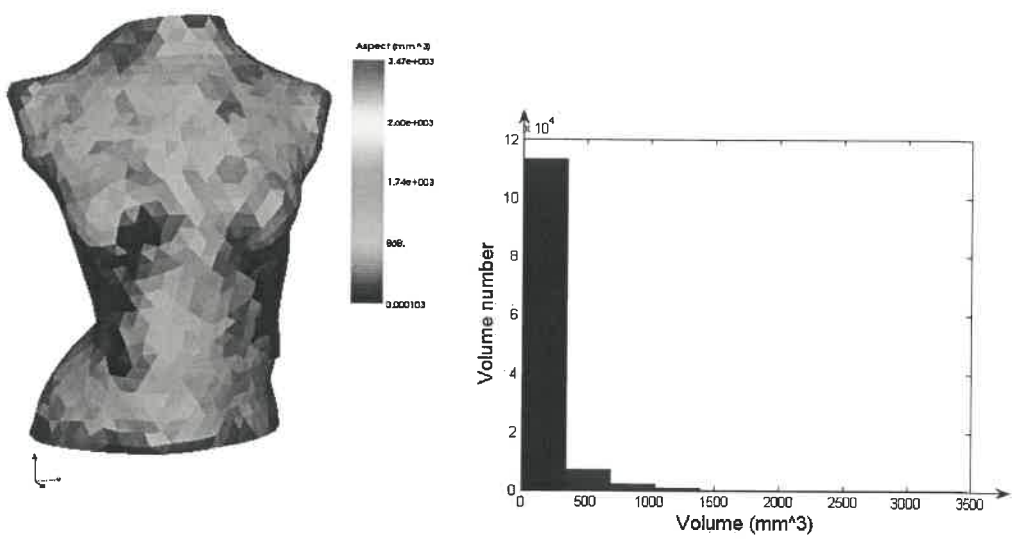

Figure 4.11: Distribution of mesh volume

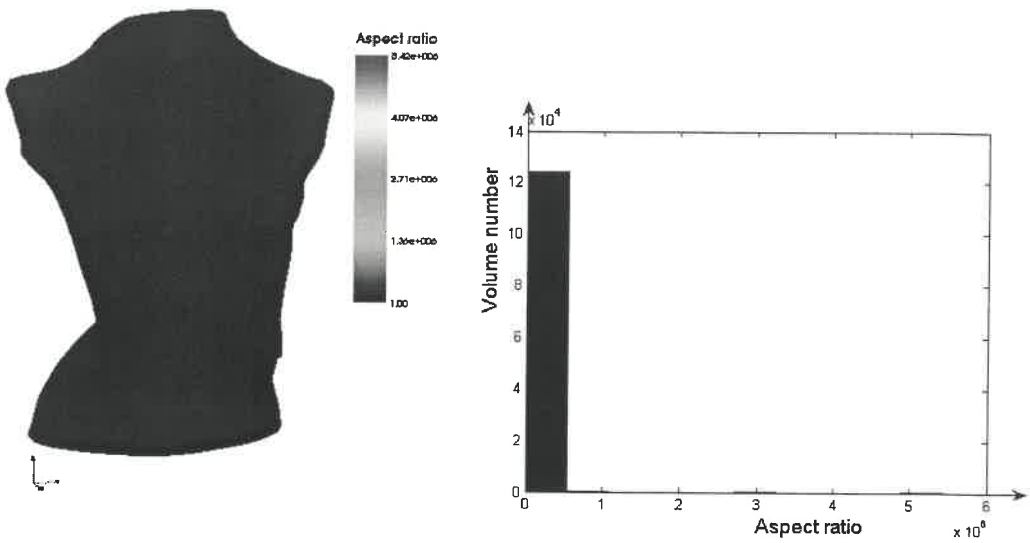

Figure 4.12: Mesh quality analysis

4.4 Linear elastic model

In this section, we describe two types of deformation simulation based on linear elastic model. The deformations move the boundary points on vertebral mesh through displacing the points or applying forces on the points. We will present some statistical data results and compare their effects.

4.4.1 Pure displacement

First, the deformation of the trunk is computed stepwise with ten iterations and each time step causes the deformation to advance one tenth of the whole distance. The total time length is ten seconds and one iteration takes one second. When the dynamically deformed model reaches stable status after more than ten seconds, we obtain the following figures, which describe the distribution of stress on the patient's trunk surface and her vertebrae.

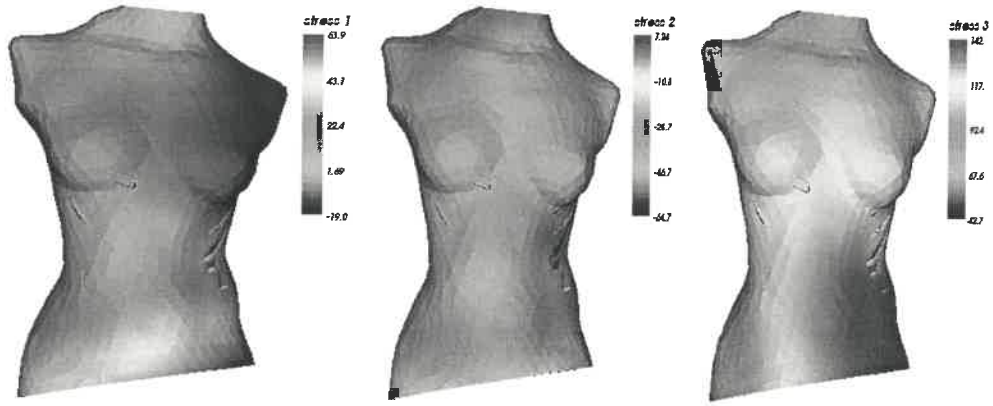

Figure 4.13: Distribution of principal stresses on surface

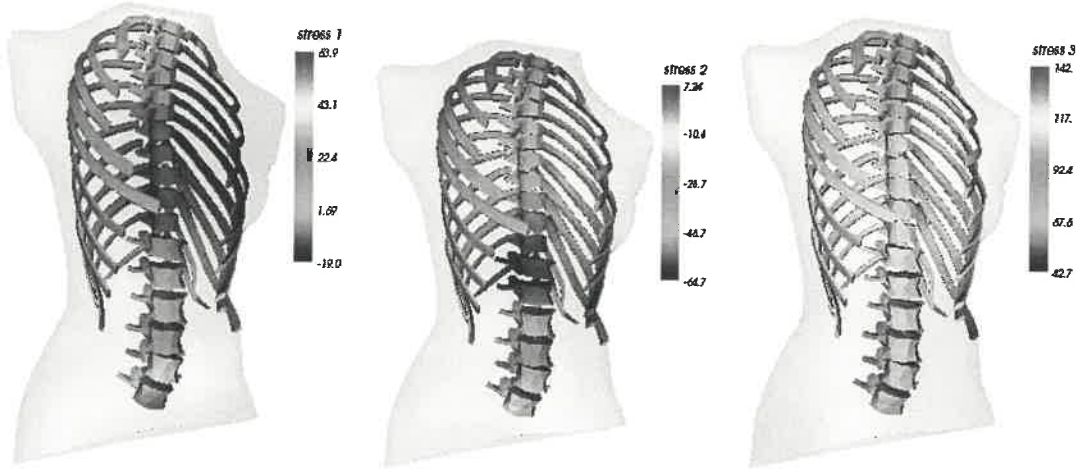

Figure 4.14: Distribution of principal stresses on vertebrae

We present the three principal stress distributions which show patient's trunk and vertebrae enduring great force to counteract the deformation caused by the surgical vertebral correction. Because the inferior part of the patient's vertebra deforms very seriously and the correction of vertebra is concentrated in the low part of spine, our result shows that her lower vertebra deform greatly much and bears bigger stress.

4.4.2 Distance error analysis

To compare our simulation results in different implementation conditions and to provide some quantitative analysis, we calculate the distance from each point on our simulated trunk surface to a reference model which derives from the same patient's postoperative geometric model, and compute the distance from each point on the reference model to the simulated trunk surface. Since the preoperative and postoperative models give only part of the patient's trunk, without head, arm and leg, and the omitted part is not the same, we reduce them to a standard size by cutting the upper and lower part of trunk using two horizontal planes and compute the error distance of points between the two planes. In figure 4.15 the front error distribution is shown and figure 4.16 shows the back error distribution. These distance errors are from the deformed to the reference model.

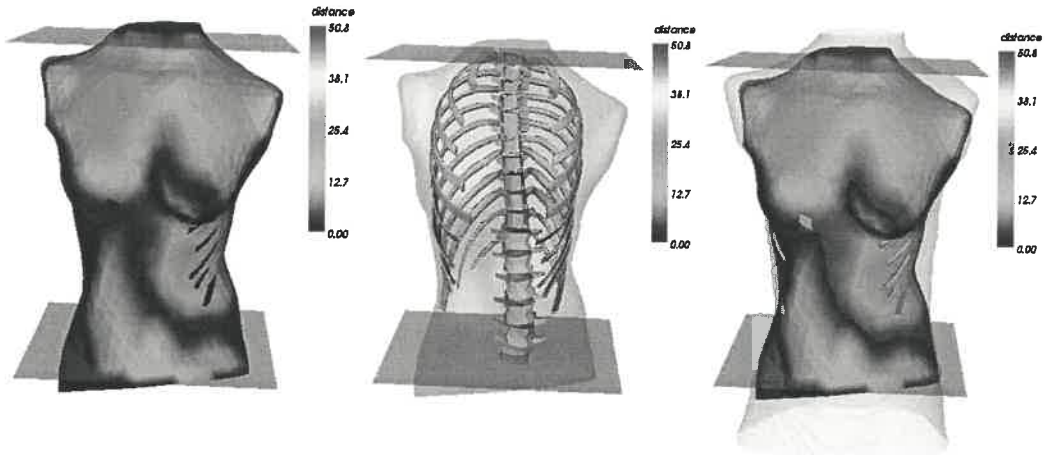

Figure 4.15: Distance distribution of the front error from deformed to reference model

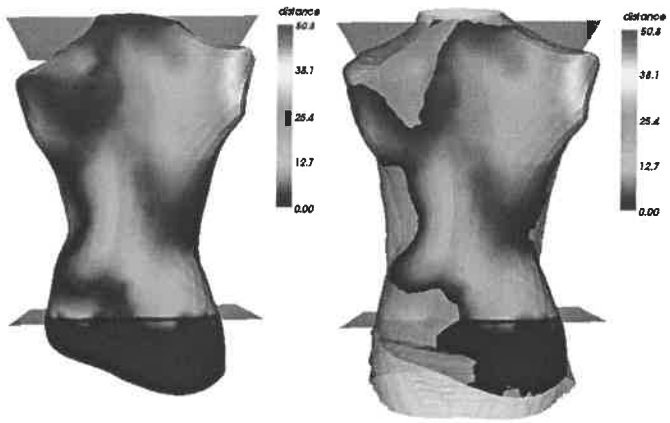

Figure 4.16: Distance distribution of back from the deformed to reference model

Error distance for ribs outside the trunk is omitted. In the above figure, we can observe that there are still some rib bones outside the surface because of the drawback of the initial mesh. During deformation, the connecting topological structure of the mesh does not change and the final result still keeps the bone outside. Although they occur on the external surface, they are excluded from the error distance statistics.

The error distribution figures show that the error distribution is not even. The error is mainly concentrated on front upper chest and the biggest error occurs on the right shoulder, where those values are up to 50 mm. From the patient's preoperative image, the patient's surgery mainly deforms her middle and lower vertebra, and the right lumbar part of the external surface has larger change after surgery.

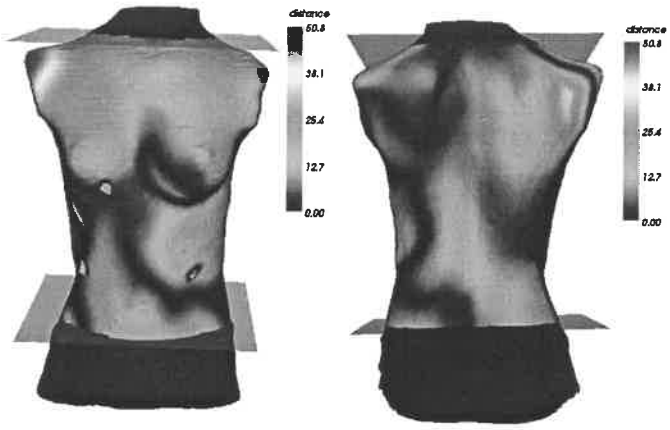

Figure 4.17: Distance distribution of error from reference to deformed model

Figure 4.17 shows the error distribution from the reference surface, i.e. the patient's clinic data, to our simulation surface. It leads to a similar conclusion that the error mainly concentrates on front upper chest and that most error occurs on the right shoulder. But its maximal and average error distances are apparently less than the error distances from our simulated surface to the reference surface, and the number of points on the surface is much greater than our optimized surface, and its resolution is very high so as to represent patient's surface more accurately.

We also present the histogram of error in the following figures; the left figure (blue) is the error distance distribution from the surface of simulated model to the surface of the patient's postoperative model and the right figure (red) is in the opposite direction, so that the error is computed from the patient's to our simulated surface. From the statistics of the points on the histogram, we find the number of points on our simulated surface has been reduced to 1460 and the points chosen to compute error distance on reference surface are 51549.

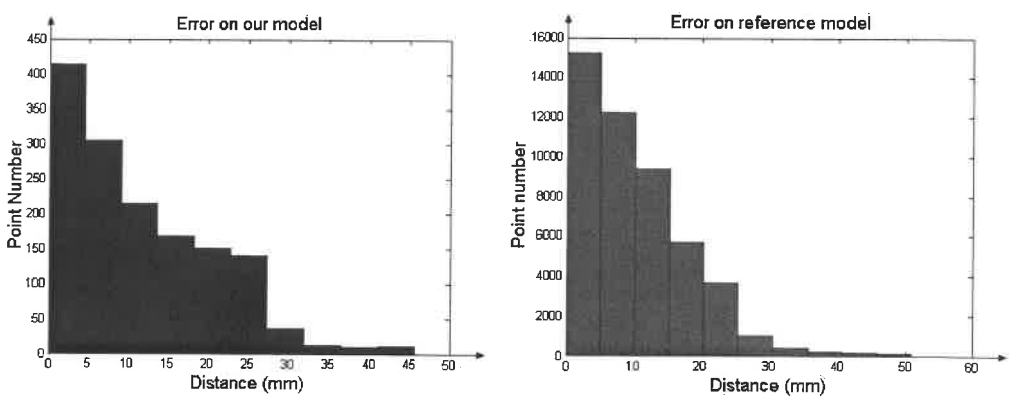

Figure 4.18: Histogram of error distance (blue on surface of our simulation, red on surface of reference)

4.5 Linear application of force

To execute the smoother deformation procedure, we substitute the pure displacement on each key point (102 points on the vertebra mesh) with the force boundary condition on each point, which attracts each point to the destination position. We also define the ten iterations to make the key points arrive at the final position; each step makes them

approach one-tenth of the way along the path. After many iterations, we obtain the final stable status, and the stresses on each point which counteract the effect from external forces and form a dynamic balance. The following figures show the distribution of three principal stresses on surface of trunk and vertebrae. According to the stress distribution, we can judge that the patient's lower trunk and internal lower vertebrae undergo the much great pressure after surgery correction.

Since it is unlike the pure displacement application, the force boundary condition must define the value of force at each key point. Because we use the spring force to move these points toward the destination, the bigger the spring constant, the closer to destination is to the final position of the moved point. But too large a force may drive the system to an unstable situation in the numerical solution. After many trials, we assigned the spring constant 1.0×10^7(N/m) which makes the differential equation arrive at the final stable solution in a reasonable number of time steps (about 10 steps). The following two figures show the three principle stress distributions on the deformed surface and the internal vertebrae of our simulated model.

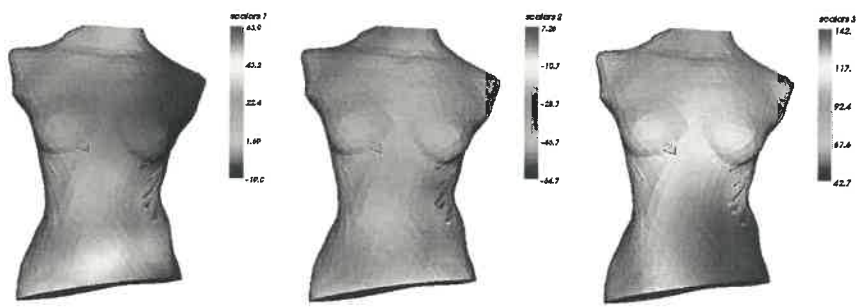

Figure 4.19: Distribution of principal stresses on surface

Figure 4.20: Distribution of principal stresses on vertebrae

4.5.1 Distance error analysis

We also computed the error distance from the surface of our simulated model to the standard clinic reconstructed model, and the error distance from the standard model to ours. Like the displacement, because the two models do not have the same size after the head and legs are removed from the patient's model, to obtain the comparison on the same part of trunk, we also selected two positions above and below cutting planes to get the same part of trunk between them and compute the surface error distance in two directions. Figure 4.21 presents the front error distribution from our simulated model to patient's postoperative clinical data, and figure 4.22 shows the back error distribution, where these distance errors are from the deformed to the reference model. Figure 4.23 shows the distribution of distance on the reference model, from its surface to the surface of our deformed model. The histogram of the distance error is also shown in figure 4.24, where the blue is the error distribution on the surface of our model, and the red is the error distribution on the surface of the standard clinical model.

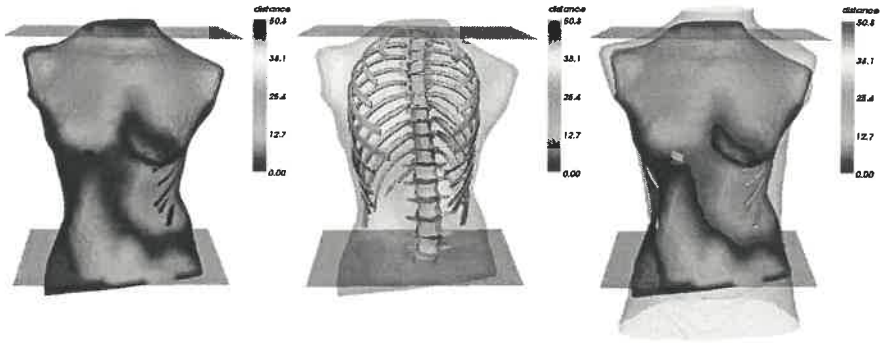

Figure 4.21: Distance distribution of front error from deformed to reference model

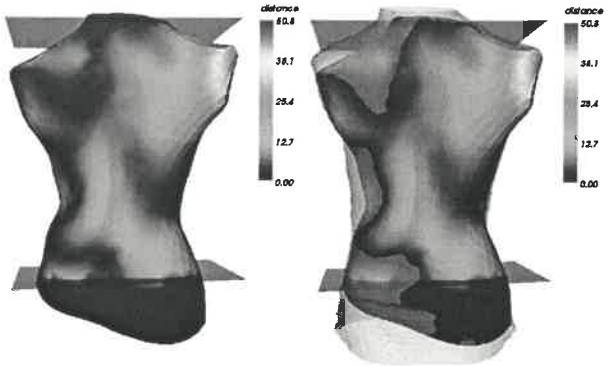

Figure 4.22: Distance distribution of back from deformed to reference model

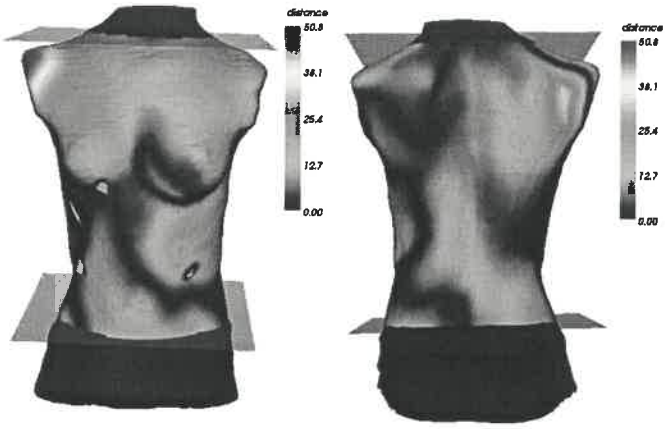

Figure 4.23: Distance distribution of error from reference to deformed model

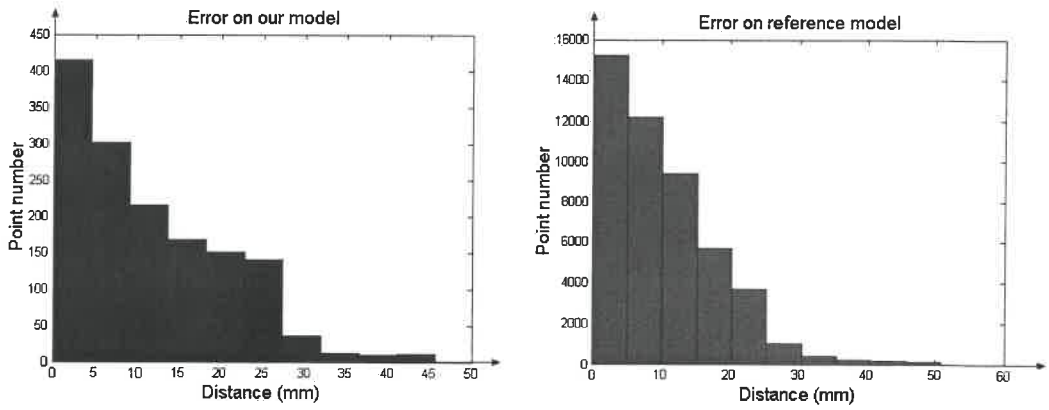

Figure 4.24: Histogram of error distance (blue on surface of our simulation, red on surface of reference)

4.5.2 Residual of spring distance

Unlike the displacement boundary, the key points on vertebrae on which the spring forces are implemented do not move to specified positions. At the final balance status, the position of the moved points must remain a certain distance from their ideal positions, so that the external forces still remain in the end to keep the trunk deformed. Although increasing spring constants can reduce the tolerance distance, as we discussed above, too large a spring force could cause instability, and require a smaller time step and more computation time to reach equilibrium. We have used a spring constant as large as 1.0×10^7(N/m), and the final tolerance has been very small (see table below). Some statistical analysis results are given in the following figure and table.

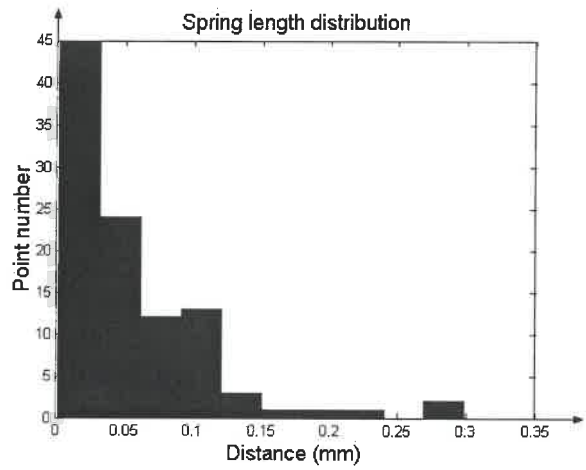

Figure 4.25: Histogram of tolerance error

Table 4.4: Tolerance error at final balance

Parameters	Point number	Maximum error (mm)	Average error (mm)	Standard deviation
Linear finite element pure displacement	102	0.2990	0.0562	0.0555

With 102 moved points, their final position is very little from the ideal position as the table shows the maximal distance is 0.2999 (mm), the mean is 0.0562 (mm), and the standard deviation 0.0555 (mm). Compared with the error of the simulated result of our model which is about 10 (mm), their influence on deformed result can be ignored.

4.6 Non-linear application of force

When an object deforms beyond 10% of its volume, the accuracy of linear FEM simulation declines with the increase of degree of deformation. Also, when an object rotates, it produces unnecessary deformation. However, the nonlinear FEM gives more precise estimation at the cost of increased computation time, complexity of the algorithm, and difficulty of convergence of the nonlinear equation solver. To improve the accuracy of our simulation under great deformation of soft tissue, we implement an

algorithm of nonlinear finite element and obtain some conclusions. Because the pure displacement implementation for nonlinear finite element still produces divergence in spite of the great reduction of the time step, we use instead spring force to slowly move the key points.

As in the linear system, we solve the dynamic system by dividing total time (10 seconds) into 10 time steps and each time step makes the key points undergo one tenth of the deformation. After the deformation reaches stable status, we obtain the stress distributions on the surface of the trunk and vertebrae, which are displayed in the following figures, based on its three principal stresses. The stress distribution also shows that the deformation forces are mainly concentrated on the lower part of the patient's trunk to correct her lower vertebrae, which had serious deformation before surgery.

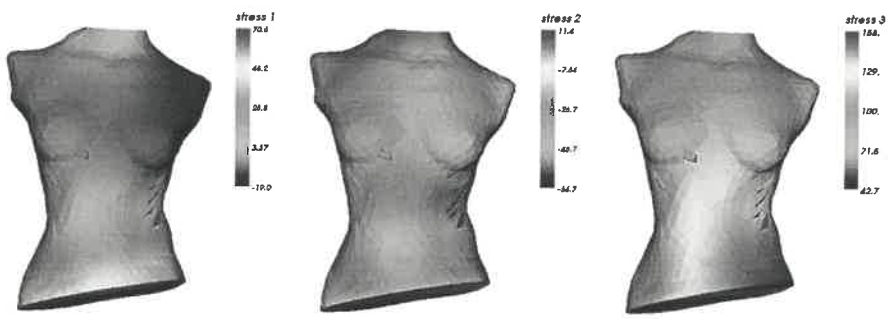

Figure 4.26: Distribution of principal stresses on surface

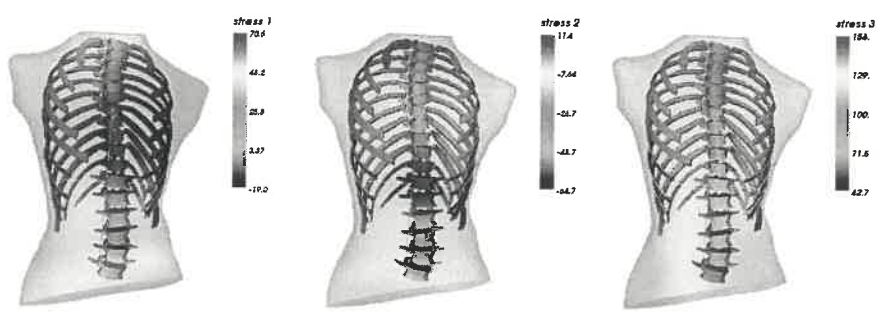

Figure 4.27: Distribution of principal stresses on vertebrae

We also assign a relatively big value $1.0x10^7$(N/m) to the spring constant to drive the nonlinear finite element to final stable status. Unlike the linear situation, the convergence of the equation of nonlinear finite element is very sensitive to the nonlinear parameter settings, boundary conditions and different materials. Some finite element materials can undergo deformation under more severe compression; for example, the Mooney-Rivlin hyperelastic material can endure 200% deformation with a stable solution. We select the Saint Venant-Kirchhoff hypoerelastic material which can accommodate nonlinear deformation below 100%. After more than ten iterations, we attained the final stable status.

4.6.1 Distance error analysis

To evaluate our deformed model, we again compute the distance error from our simulated model to the clinic standard model and from clinic standard model to our simulated model. As in the linear situation, we only evaluate the middle part of trunk between two cutting planes in order that the two models have a common surface to compare. Figure 4.28 shows the distribution of distance error on the front surface of the patient's trunk, and figure 4.29 shows the distribution of error on the back surface of her trunk.

We also draw the distance distribution (figure 4.30) on the surface of the standard clinical model which is based on the distance computation from its surface to the surface of our deformed model.

The histogram of the distance error is also shown in figure 4.31 where the blue is the error in the surface of our model and the red is the error distribution on the surface of the standard clinic model.

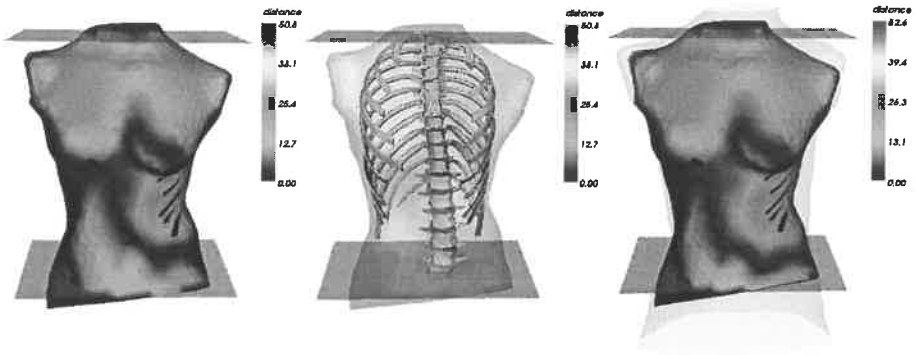

Figure 4.28: Distance distribution of front error from deformed to reference model

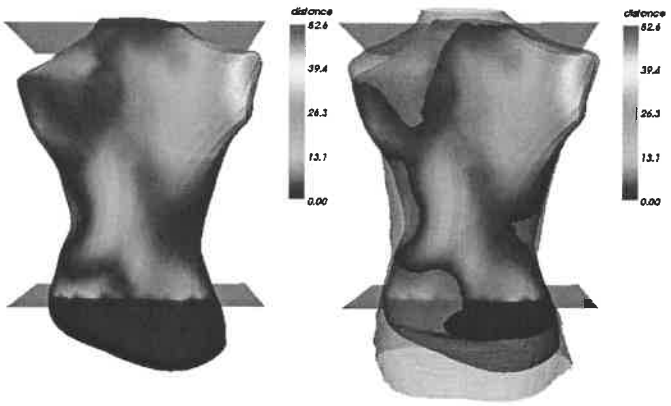

Figure 4.29: Distance distribution of back from deformed to reference model

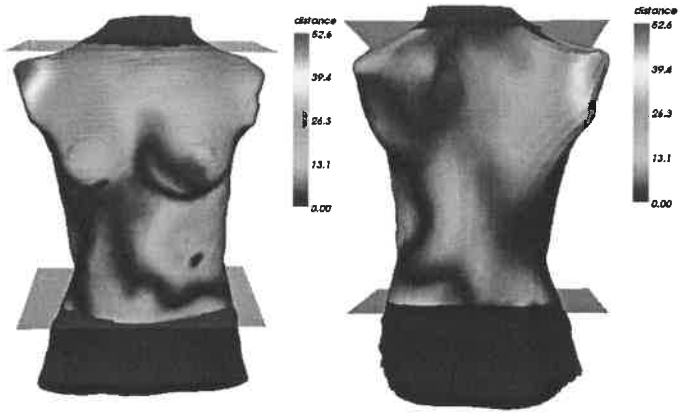

Figure 4.30: Distance distribution of error from reference to deformed model

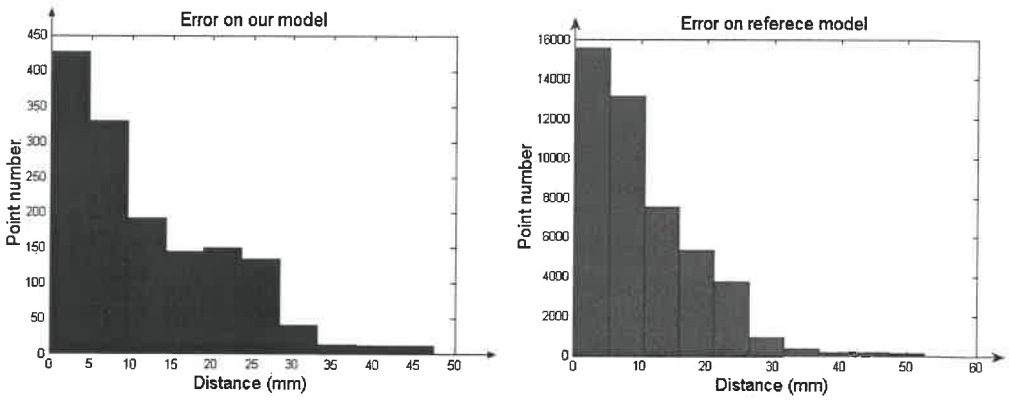

Figure 4.31: Histogram of error distance (blue on surface of our simulation, red on surface of reference)

4.6.2 Residual of spring distance

We apply some spring forces on the key points on vertebrae until the model reaches a balance status. Of course, when the forces are removed, the model will go back to the undeformed situation. To maintain the deformed status, we keep the spring forces which are determined by the distance between the coordinates of the points and specified points defined as the ideal positions to which the key points should move. The gap distance can be reduced with the increase of the spring constant, but at the final equilibrium status, the springs always remain extened to keep the deformed trunk. The lengths are shown in figure 4.32 and table 4.5. From analysis of the statistical results, the maximal distance between the 102 moved points and their postoperative positions is 0.263 (mm), mean distance is 0.0514 (mm), and the standard deviation 0.0439 (mm). So the small distance gap can be ignored compared with the error 10 (mm) of our simulated model.

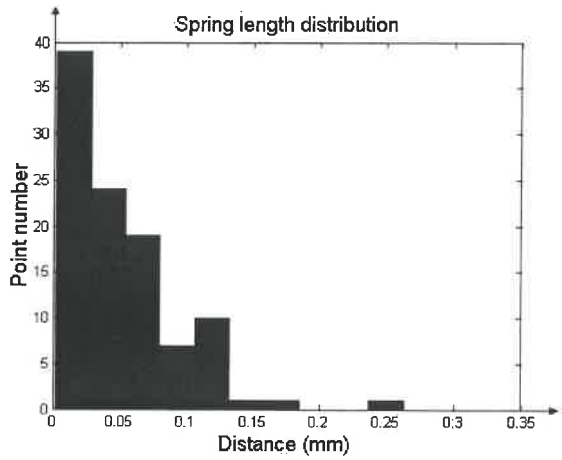

Figure 4.32: Histogram of tolerance error

Table 4.5: Tolerance error at final balance

Parameters	Point number	Maximum error (mm)	Average error (mm)	Standard deviation
	102	0.2630	0.0514	0.0439

CHAPTER : 5 DISCUSSION

As summarized in the following table, we used finite element methods with different boundary conditions and different material types to acquire the final deformed surface and compute some quantitative indexes to compare their effects. The Euclidean distance metric was used to compute the distance error in two directions: one is from the simulated surface (postoperative surface) to the reference surface (postoperative standard model) and the other is from the reference surface to the simulated surface. Their maximum and average error and standard deviation are also listed in table.

Table 5.1: Analysis of simulation of three FEM

Method / Parameter		Linear finite element pure displacement	Linear finite element force application	Non-linear finite element force application
Point number	Simulation	1460	1460	1450
	Reference	48080	48076	46972
Maximum error	Simulation (mm)	45.6589	45.6632	47.3865
	Reference (mm)	50.7616	50.7633	52.5780
Average error	Simulation (mm)	11.6171	11.6174	11.8449
	Reference (mm)	10.2195	10.2203	10.2661
	Total (mm)	10.2607	10.2615	10.3134
Standard deviation	Simulation (mm)	9.1513	9.1519	9.6047
	Reference (mm)	7.8796	7.8805	8.2029
	Total (mm)	7.9235	7.9243	8.2526

From the above analysis we conclude that the linear elasticity based finite element method with pure displacement achieves the best simulation result, where the average distance error is only 10.2607 (mm) after averaging the distance error in two directions. Next is linear finite element force application. The order from best to worst is linear finite element pure displacement, linear finite element force application, and non-linear finite element force application.

The two linear methods show very little difference and their average error index have a maximum error difference of only 0.002 (mm). Since the linear finite element method with force application has the distance tolerance of springs between the key points at the final equilibrium status and the posteroperative extended landmark position to keep the deformed model, this leads to a slightly bigger error.

The distance error of nonlinear FEM is also very near to linear FEM, and the difference range of the average error is within 0.05 (mm). In this simulation, the nonlinear FEM does not produce as good a result as we expect. This is mainly because the patient's trunk after surgery does not undergo large rotation or deformation so that the advantage of nonlinear finite element does not appear.

To quantify the effect of our simulation, we computed the difference between the pre and post operative surfaces of trunk. Their maximum distance is 143.738 (mm) and the average distance is 40.7889 (mm). The ratio of the maximal distance error of our best linear pure displacement is 35.315% and the ratio of average distance error is 25.156%. This shows that our simulation approaches the postoperative external surface and may, with some improvements, accurately predict postoperative appearance.

The following table lists the initial configuration of our deformable model and the computation time of different finite element methods. The nonlinear model uses almost twice time as much as the linear model under the same configuration. Most of the time is consumed by the force and stiffness matrix computations because the stiffness matrix must be recomputed at each time step in nonlinear model.

Table 5.2: Computation analysis

Method / Parameter		Liner model with pure displacement	Linear model with spring force	Nonlinear model with spring force
Computation time(1.4 G CPU 512M Mem)		1h 10min	1h 20min	2h 32min
Number of tetrahedron	Rib cage and spine	20,689		
	Soft tissue	86,557		
	Ligament	16,895		
Number of nodes		22,336		
Simulation time (sec)		10		
Iteration time		10		

Based on our experiments, we clearly must discuss the following problems. First, the quality of the mesh we used for experiments is not good enough; for example, some of its tetrahedrons have a very thin and long shape, and the tetrahedrons vary very greatly in size and shape. This variation directly affects our result, and even makes the stiffness matrix ill-conditioned when some tetrahedrons have zero volume. In large deformations, some tetrahedrons will change into zero or negative volume (according to the right-hand sign definition of volume), which makes the gradient computation in tetrahedron impossible and prevents the assembly of the stiffness matrix, even though we reduce the integration time step.

We have shown that our proposed algorithm and constructed models are suitable and robust in simulating the deformation of anatomical models. On the other hand, we are now constructing a more accurate model which can describe the human trunk with more

internal tissues, by using volume mesh. However, accurate simulation, in the sense that one can confidently control the numerical error compared to real subjects, is quite difficult at this point. The difficulty is not only due to the problems in computational methods, but also (and more importantly) due to the premature state of the art of biomechanics: there are great difficulties in building mathematical models of real biological tissues. First of all, the material models (constitutive laws) of tissues are not yet established. Even if it could be assumed that a simple constitutive law can be applied, there is no equipment or method that can measure heterogeneous *in vivo* material properties of tissues.

At present, there exist no accurate mechanical parameters in the biomedical field to describe the mechanical properties of human tissue because the behavior of human tissue is different in different situations, such as tissue *in vivo* or *ex vivo*. Another difficulty is that different people, even different parts of the trunk of the same person, also have different properties. Since applying the same parameters on the whole trunk is not reasonable, more research in the biomedical field is needed to find a set of relatively good parameters to reach a more realistic deformable model. We at least need three types of parameters, one for tissue, one for ligament and one for bone (whose linear parameters can be obtained from Aubin [Aub95]). Finally, although some values of general parameters can be attained from medical measurement, they are not completely adapted to our application so that some discrepancy appears between our deformable model and the real deformed skeleton of the patient.

Generally, a smooth surface is better than a polygonal surface because it looks more realistic on computer screens and can be easily detected by human visual systems. But the smoothness of the surface does not help the physics simulation. Many mechanical parts have mathematically-defined smooth curved surfaces. Some of the surfaces of internal organs (like the liver) certainly look smooth. Although initial object boundaries in the reference configuration are smooth, the domain of the PDE and the shape of the finite element mesh do not always match. The PDE can be integrated within curved boundaries by adjusting the weights and positions of quadrature points. However, such

decoupling may make the meshing process more difficult. On the other hand, the smoothness requirement of shape functions is directly related to the order of the PDE. The linear bases for tetrahedral elements are sufficient for the PDEs used for our deformable object where the PDE is only second order. Of course, the continuity must be increased as the order of the PDE increases. By using shape functions with a broader basis, the continuity of the deformation function can be achieved. However, a broader basis results in denser stiffness matrices. Consider a trilinear hexahedral element. The size of the stiffness matrix is $2^3 \times 2^3$. If a tricubic B-Spline is used, the size jumps to $4^3 \times 4^3$, and the latter is computationally impractical. The area-integration smoothing technique is preferable when high curvature surfaces are treated and normal smoothing techniques may be more efficient. Ultimately, the differential equations decide how smooth the surface should be.

Second, an accurate mesh representation of human trunk with different tissues is still not available; our mesh does not accurately represent the body's anatomical structure. When we created the mesh based on medical images, we just segmented the vertebrae, the ribs, and all the rest of the body, which is represented by soft tissue. This is unrealistic and results in inaccuracy in the experimental results.

Third, the purpose of our finite element simulation program is to demonstrate the usefulness of our algorithm to predict the deformation of external surface of human trunk. Thus, the error estimate is essential to the evaluation of the system. The numerical errors contained in the computed results come from several factors. An important one comes from the discretization procedure. All physical phenomena are described in the form of partial differential equations (PDEs) and discretization (FEM in our project) converts the PDEs into algebraic equations. When the final solution of the nonlinear equation is found, putting the solution back into the original PDEs, one would find that the solution does not satisfy the PDEs. They would have non-zero values (residual errors measured as volumetric forces). The residual error does not vanish even if the nonlinear solver finds an exact solution for the algebraic equations since the algebraic equations are different from the original PDE. A residual error (force) implies that the solution also

contains an error (measured as position). This error in the solution is introduced by discretization; hence it is called the discretization error. The discretization error is mainly introduced by the shape and size of each element. The polynomial orders of shape functions can also adjust the error. But it is hard to estimate the discretization error before computation (*a priori* error estimation). Most methods estimate the error from residual error (*a posteriori* error estimation) (Babuska 1984).

Sparse matrices reduce the need for memory and some iterative methods speed up the solution of the equations. Since the matrices are very large, general matrix methods do not fit our requirements. In particular, matrix inversion is very slow or impossible on such a large matrix. But because the use of an implicit integration method generates large unbanded sparse linear systems, we can solve these systems through a conjugate gradient (CG) or generalized Minimum Residual Method (GMRES) iterative method. GMRES methods exploit sparsity quite easily, since they are based solely on matrix-vector multiplies, and require only rudimentary sparse storage techniques.

CHAPTER : 6 CONCLUSION AND FUTURE WORK

6.1 Conclusion

This project was a simulation of postoperative body deformation of scoliotic patients. We applied the finite element method to achieve the simulation. After constructing a dynamic differential equation to describe the deformation procedure, trying different methods to solve the nonlinear algebraic equations and different values of material properties, we obtained the expected results. We first constructed the deformable trunk structure which consists of three types of tissues with different material properties. Second, we have designed two types of boundary conditions based on preoperative and postoperative anatomical landmarks on vertebrae which are measured from a scoliotic patient's X-rays. Third, we have implemented the dynamic deformation of linear and nonlinear elastic models and quantitatively compared their simulated results with the patient's postoperative clinical data.

We devoted a great part of our work to the development of deformable models allowing the representation of the human trunk, on which a variety of deformation drivers were applied. We select the scoliotic patient's trunk model, which can be made of a variety of shape elements such as tetrahedra with different degrees of freedom, to implement the deformation test. To simplify and decrease the computation time, our model consisted of simplicial tetrahedron volumes with degrees of freedom consisting of 4 nodes. The model allows the results to be more quickly obtained and rendered, because computation in each tetrahedron is reduced to one Gauss quadrature point.

We have constructed the dynamic model from the static model. After we have acquired the static relationship between the vertices of each finite element, and the internal and external forces exerted on it, we add two items (acceleration and velocity) and two parameters (material mass and damping) into the static equation so as to acquire a dynamic equation to simulate the successive motion of deformation, modeled by an ordinary differential equation of order 2.

There are two types of methods to solve the ordinary differential equation: explicit and implicit methods. We have implemented the explicit and implicit methods on linear and nonlinear models with an adaptive time step adjustment. The results of the explicit method show a dynamic sequence which exhibits the successive deformation of soft tissue under the external forces. In the linear and nonlinear models, we have also observed that if we assign a very small value to parameters which express the stiffness of material i.e. very soft material, the deformation is very fast. In contrast, in experiments, the deformation seems slow when very rigid material parameters are applied. To use a larger time step, we resort to implicit methods to accelerate the solution of the differential equation.

We have applied the Newmark implicit integration method to the linear finite element model. It guarantees the stability of the linear system unconditionally by controlling the range of parameter values. Meanwhile, we can also control the deformation speed by assigning Newmark integration's parameters different values. The experimental results have shown that the implicit integration is more stable and accurate because the same ten time iterations give the implicit method a longer deformation process than the explicit method.

We have evaluated the error of deformation between the simulated result of our deformable model and a realistic postoperative trunk, and selected suitable physical parameters (Young's modulus and Poisson's Ratio) according to the comparative error.

Finally we succeeded in developing a stable solver that combines various numerical techniques such as Newton iteration, adaptive incremental loading, two-point predictor, and line search. However, to handle the nonlinear Saint Venant-Kirchhoff material with high rigidity, the simulation must be carried out as a full dynamic simulation to avoid bifurcation and indefinite stiffness matrix problems.

6.2 Future work

In the future, we should try to improve the quality of our mesh and use some dynamic algorithms to prevent occurrence of bad tetrahedra, thus increasing the robustness of the

FEM. In the experiments, we only used the simplicial finite element (tetrahedron with four nodes). Although it can approximate any geometric shape accurately and with low computation time, its stability during the solution of the dynamic equation is relatively lower than other geometric forms. In the future, we may try other finite element forms such as the hexahedron. Our tetrahedron element has C^0 continuity which means the interpolation function or shape function is a polynomial of order 1. To improve the continuity, the tetrahedron element with ten nodes or thirty degrees of freedom can be implemented, which requires that each finite element consist of ten nodes. This will change the mesh structures. A mixture of different finite element structures, such as a mixture of hexahedron and tetrahedron, is also a research direction which may improve stability and accuracy of the nonlinear equation.

To build a high-fidelity mathematical model of the subject, we should also consider the incompressibility of biological tissue, because biological tissues contain 60-70% water, which is nearly incompressible. Therefore, an accurate material model should exhibit incompressibility. While the fluids are incompressible, the underlying protein networks are compressible. The use of biphasic constitutive laws is a possible way to simulate both incompressible and compressible phases (Mow 1980, Donzelli 1995).

The parameters we used for material properties were derived from the extrapolation of cadaveric data, and therefore they are different from those of living tissues. In research on properties of human organs, *in vivo* measurement is preferred and can produce more accurate parameters. Its development will help us to obtain better results. Besides, if the human anatomical structure includes sliding contacts between different tissues, frictional properties on interfaces should also be estimated by the method and be taken into consideration in model construction.

Dynamic error estimation as an index to evaluate the biomechanical simulation system is a very important research direction. It is the basis and premise for a finite element method involving a dynamic self-adaptive mesh, which might reduce computation and improve accuracy. The technology of the error estimates can be used to indicate if the error has exceeded the threshold and if the finite element mesh should be adjusted

(Zienkiewicz 2000). At present, at least three aspects of the mesh can be adjusted. If the element sizes are adjusted, the method is called h-adaptive ("h" is usually the choice of symbol for the step size i.e., element size. With an h-adaptive method, the FEM analysis can be started with a coarse mesh, and, according to the *a posteriori* error distribution, the mesh can be locally refined until a sufficient accuracy is achieved. If polynomial order is adjusted, it is called p-adaptive. And finally, if the position of an element is moved (relocated), it is called r-adaptive. The dynamic mesh adjustment with error estimate can potentially relax the convergence criteria in solving the equation. In our simulation, our present mesh has been fixed so that it cannot adjust in a way compatible with local accuracy, but the adaptive method is very valuable to reduce computation time and improve accuracy. In our future model, the h-adaptive method can be considered as research direction to enhance the adaptability of our model because it can easily control the local mesh quality.

The balance of accuracy and speed needs to be considered in the mesh construction. The most decisive factor for computation time is the complexity of the problem. Fast simulations can be achieved by simplifying (hence reducing the fidelity of) the simulation models. The time complexity of FEM computation is roughly linear relative to the number of elements. The simplest way to reduce the computation time is to use fewer elements. So reduction of unnecessary elements at a specified accuracy is helpful to quickly simulate deformation. As mentioned above, mesh refinement and coarsening locally is very effective in reducing the number of elements (Hirota G. 2002).

The combination of linear and nonlinear finite elements can reduce computation time and the complexity of mesh structure. Although human tissues exhibit nonlinear and inelastic behavior, we can implement the material properties only in a local region and some simple linear and elastic models in the rest of the model so as to reduce the computation time and complexity of assembly of FEM.

Since the nonlinear FEM consumes too much time and memory, the parallelization of computation is a good choice to achieve better results. In the processing of finite elements, most of the computation is local to each finite element. For example, force and

stiffness matrix computations can be performed for a small collection of elements making it possible to use parallel algorithms. The final assembly of forces and matrices can be done by a parallel summation algorithm. Thus, parallelization can be implemented to improve execution speed.

REFERENCES

ANDRÉ B., DANSEREAU J., and ALLARD P. (1990). Calibration object measurements and three-dimensional reconstruction accuracy of the DLT algorithm. In Proc. 14th Annual Meeting American Society Biomechanics, 89–90.

ANSYS. ANSYS Release 8.1 Documentation. Cannonsburg, Pennsylvania: ANSYS, Incorporated, 2000.

ASCANI E., BARTOLOZZI P., LOGROSCINO CA., MARCHETTI PG., PONTE A., SAVINI R., TRAVAGLINI F., BINAZZI R., SILVESTRE M. Di. (1986). Natural history of untreated idiopathic scoliosis after skeletal maturity. Spine, 11(8): 784-789.

AUBIN C.-É. (1995). Rôle biomécanique de la cage thoracique dans le traitement de la scoliose par orthese. Thèse à l'École Polytechnique, Montreal, Canada.

AUBIN C.-É., DANSEREAU J., LABELLE H. (1993). Biomechanical simulation of the Boston braces effect on a model of the scoliotic spine and thorax (in French). Ann. Chir. 47(9):881-887.

AUBIN C.-É., DANSEREAU J., PARENT F., LABELLE H., and GUISE J. A. de. (Nov. 1997). Morphometric evaluations of personalized 3D reconstructions and geometric models of the human spine, Med. Biol. Eng. Comput., vol. 35, 1–8.

AUBIN C.-É., LABELLE H., RUSZKOWSKI A., PETIT Y., GIGNAC D., JONCAS J., DANSEREAU J. (1999). Variability of strap tension in brace treatment for adolescent idiopathic scoliosis. Spine 24-4:349-354.

BABUSKA I., CHANDRA J., and FLAHERTY J. E. (1984), Adaptive methods for partial differential equations. SIAM, Philadelphia.

BAGNALL K. M. (2000), Ligamen s and muscles in idiopathic scoliosis, Spine, State of the Art Reviews, Eds. Burwell R.G. & Dangerfield P.H. , Hanley & Belfus, Philadephia, USA, 14(1): 447-457.

BAINVILL E., BRICAULT I., CINQUIN P., LAVALLÉE S. (1999). Concepts and methods of registration for computer integrated surgery. Computer Assisted Orthopedic Surgery, Ed. Nolte, L.P., Ganz, R., Hogrefe & Huber Publishers, 15-24.

BARR A. H. (1984). Global and local deformations of solid primitives. Computer Graphics, 18(3):21–29.

BARTELS R. and BEATY J. (1989). A technique for the direct manipulation of splines curves. In Proceedings of Graphics Interface.

BARTELS R., J. BEATY, and BARSKI B. (1987). An introduction to splines for use in Computer Graphics and Geometric Modeling. Morgan Kaufmann, Los Altos.

BASMAJIAN John V. (1977). Anatomie, 7th ed., Maloine S.A. SOMABEC Ltée.

BATHE K. J. (1996). Finite Element Proceedures. Prentice Hall, Englewood Cliffs, NJ.

BEAUCHAMP A., DANSEREAU J., GUISE J. de, and LABELLE H. (1992). Computer assisted digitization system for scoliotic spinal stereoradiographs. In Proc. Int. Symp. 3-D Scoliotic Deformities, J. Dansereau, Ed. 18–25., Montreal, Canada.

BELYTSCHKO Ted, LIU W. K., MORAN B. (2000). Nonlinear Finite Elements for Continua and Structures. John Wiley & Sons, Ltd.

BLOOMENTHAL J. (May 1987). Polygonization of implicit surfaces. Xerox Technical Report CSL-87-2, 1–19.

BLOOMENTHAL J. (1988). Polygonisation of implicit surfaces. Computer Aided Geometric Design, 5:341–355.

BOOKSTEIN F. L. (1989). Principal Warps: Thin-Plate Splines and the Decomposition of Deformations June IEEE Transactions on Pattern Analysis and Machine Intelligence, Volume 11 Issue 6.

BOURGUIGNON D. and CANI M.-P. (2000). Controlling Anisotropy in Mass-Spring Systems. In Proceedings of the 11th Eurographics Workshop on Animation and Simulation. Springer-Verlag.

BOUX DE CASSON F. and LAUGIER C. (1999). Modeling the Dynamics of a Human Liver for a Minimally Invasive Surgery Simulator. In Second International Conference on Medical Image Computing and Computer Assisted Intervention-MICCAI'99, 1156-1165, Cambridge, UK.

BRADFORD D. S, LONSTEIN J. E., MOE J. H., OGILVIE J.W. Winter R.B (1987) Moe's textbook of scoliosis and other spinal deformity.

BRIDWELL K. (2004) Ligaments. www.spineuniverse.com/.

BRO-NIELSEN M. (1995). Modeling elasticity in solids using active cubes–application to simulated operations. In Computer Vision, Virtual Reality and Robotics in Medecine, 535-541, Springer.

BRO-NIELSEN M. (March 1996). Medical Image Registration and Surgery Simulation. Ph.D. dissertation, IMM Technical University of Denmark, Lingby, Denmark, IMM-PHD-1996-25.

BRO-NIELSEN M. and COTIN S. (1996). Real-time Volumetric Deformable Models for Surgery Simulation using Finite Elements and Condensation. In Proceedings of Eurographics'96-Computer Graphics Forum, 57-66.

BUCHOLZ R. D., SMITH K. R., HENDERSON J. and MCDURMONT L. (1994). Intraoperative localization using a three dimensional optical digitizer, First international Symposium on Medical Robotics and Computer Assisted Surgery, 2: 283-2900.

BURTNYK N. and WEIN M., (October 1976). Interactive skeleton technique for enhancing motion dynamics in key frame animation. Communications of the ACM, 19(10):564–569.

BURWELL R. G., DANGERFIELD, P. H. (1992), Pathogenesis and assessment of scoliosis, Spline, 17: 108-111.

BURWELL R. G., DANGERFIELD P.H (2000), Adolescebt idiopathic scoliosis hypothesis of causation, Spine. State of the Art Reviews, Eds. Burwell R.G. and DangerFiels P.H., Hanley & Belfus, Ohiladephia, USA, 14(1):319-333.

CARRIER J. (2002) Étude biomécanique de l'effet immédiat et à long terme de chirurgies costales pour le traitement des scoliosis. Mémoire de maîtrise, École polytechnique, Département de genie biomédical.

CHEN D. T. and ZELTZER D. (July 1992). Pump it up: Computer animation of a biomechanically based model of muscle using the finite element method. In Edwin E. Catmull, editor, Computer Graphics (SIGGRAPH '92 Proceedings), 89-98.

CHEN Y., ZHU Q.-H. and KAUFMAN A. (1998). Physically-based Animation of Volumetric Objects. In Computer Animation '98, 154-160.

COQUILLART S. (1990). Extending free-form deformation: a sculpting tool for 3d geometric modeling. Proceedings of SIGGRAPH'90, 187–196.

COLLIER J., COLLIER B., O'TOOLE G., and SARGAND S. (1991). Drape prediction by means of finite elements analysis. In Journal of the Textile Institute, volume 82(1), 96–107.

COTIN S. (1997) Modèles anatomiques déformables en temps-réel. PhD thesis, Epidaure-Sophia Antipolis.

COTIN S., DELINGETTE H., and AYACHE N. (1996). Real Time Volumetric Deformable Models for Surgery Simulation. In K. Hohne and R. Kikinis, editors, Vizualisation in Biomedical Computing, 535-540, Springer.

CRISFIELD M. A. (1981). A Fast Incremental/Iterative Solution Procedure that Handles "Snap-Through. Computers & Structures, 13, 55-62.

D'AULIGNAC D., LAUGIER C. and CAVUSOGLU M. (1999a). Modeling the dynamics of a human thigh for a realistic echographic Simulator with force feedback. In Second International Conference on Medical Image Computing and Computer Assisted Intervention MICCAI'99, 1191-1198, Cambridge, UK.

D'AULIGNAC D., LAUGIER C. and VUSOGLU M. C. (1999b).Towards a realistic echographic Simulator with force feedback. Dans Proc. of the IEEE-RSJ Int. Conf. on Intelligent Robots and Systems, 727-732, Kyongju (KR).

DANSEREAU J. and STOKES I. A. (1988). Measurements of the three-dimensional shape of the rib cage. J. Biomech., vol. 21, 893–901.

DAVIES P. J., CARTER F. J., ROXBURGH D. C. and CUSCHIERI A. (1999). Mathematical modelling for keyhole surgery simulations: spleen capsule as an elastic membrane. The Journal of Theoretical Medicine, 1:247-62.

DEACON P., ARCHER I. A., DICKSON R. A. (1987). The anatomy of spinal deformity: a biomechanical analysis, Orthopaedics, 10: 897-901.

DELAUNAY B. (1934). Sur la Sphère. Vide. Izvestia Akademia Nauk SSSR, VII Seria, Otdelenie Matematicheskii i Estestvennyka Nauk Vol. 7, 793-800.

DELINGETTE H., COTIN S., and AYACHE N. A hybrid elastic model allowing real-time cutting, deformations and force-feedback for surgery training and simulation. In Computer Animation, Geneva Switzerland, May 26-28 1999.

DELORME S. (1996). Étude de la Modélisation par Krigeage Géométrique Tridimensionnel des Vertèbres Saines et Scoliotiques. M.S. thèse, École Polytechnique de Montréal, Dept. Mech. Eng., Montreal, Canada.

DELORME S., PETIT Y., GUISE J.A. de, AUBIN C.-É., LABELLE H., LANDRY C. and DANSEREAU J. (1999). Three-Dimensional Modelling and Rendering of the Human Skeletal Trunk from 2D Radiographic Images. Proceedings of Second International Conference on 3-D Digital Imaging and Modeling, 497-505, Ottawa, Canada.

DESBRUN M., SCHRÖDER P. and BARR A. (1999). Interactive Animation of Structured Deformable Objects. In Graphics Interface '99, Kingston, Canada.

DESBRUN M., TSINGOS N., and GASCUEL M. (May 1995). Adaptive sampling of implicit surfaces for interactive modelling and animation. Computer Graphics Forum, 15(5):319–327, December 1996. A preliminary version of this paper appeared in Implicit Surfaces'95, Grenoble, France.

DESCHAMPS C., RODARTE J. R., WILSON T. A. (1988). Coupling between rib cage and abdominal compartments of the relaxed chest wall.

DESCRIMES J. L., AUBIN C.E., SKALLI W., ZELLER R., DANSEREAU J., LAVASTE F. (1995). Introduction des facettes articulaires dans une modelisation par elements finis de la colonne vertebrale et du thorax scoliotique: aspects mecaniques, Rachis 7-5:301-314.

DEUSSEN O., KOBBELT L. and TÜCKE P. (1995). Using Simulated Annealing to Obtain Good Nodal Approximations of Deformable Bodies. In Sixth Eurographics Workshop on Simulation and Animation.

DONZELLI P.S. (1995). A mixed-penalty contact finite element formulation for biphasic soft tissues, PhD Thesis, Dept. of Mech. Eng., Aeronautical Eng. and Mechanics, RPI, Troy, NY.

DUCK F. (1991). Physical properties of tissues: a comprehensive reference book. Academic Press, London.

FARIN G. (1990). Curves and Surfaces for Computer Aided Geometric Design. Academic Press Inc., San Diego, 1996. Sixth edition.

FRYMOYER JW. and CATS-BARIL WL. (1991). An overview of incidences and costs of low back care. Orthop Clin North Am 22: 63–71.

FUNG Y. C. (1993). Biomechanics-Mechanical Properties of Living Tissues. Springer-Verlag, 2nd edition.

GAO D. Y. (1995). Nonlinear Elastic Beam Theory with Application in Contact Problems and Variational Approaches. Mech. Research Communication.

GAO D. Y. (1996). Contact Problems and Dual Variational Inequality of 2-D Elasto-plastic Beam Theory. Appl. Math. and Mech. 17, 10.

GAO D. Y. (1997). Dual Extremum Principles in Finite Deformations with Applications to Post-Buckling of Extended Nonlinear Beam Theory. Appl. Mech. Rev. 50, 11, part2, Nov.

GAO D. Y. (2000). Finite Deformation Beam Models and Triality Theory in Dynamical Post-Buckling Analysis. Int. J. of Non-Linear Mech. 35, 103-131.

GRÉALOU L. (2000). Modélisation biomécanique d'interventions chirurgicales sur la cage thoracique pour le traitement des déformations scoliotiques. Mémoire de maîtrise, École polytechnique, Département de génie mécanique.

GELDER A. V. and WILHELMS J. (1997). Simulation of Elastic Membranes and Soft Tissue with Triangulated Spring Meshes. Technical Report UCSC-CRL-97-12, University of California, Santa Cruz, Jack Baskin School of Engineering.

GOURRET J.-P., MAGNENAT-THALMANN Nadia, and THALMANN Daniel. (July 1989). Simulation of object and human skin deformation in a grasping task. Proceedings of SIGGRAPH'89 (Boston, MA), 21–30.

GUISE A. and MARTEL Y. (1988). 3D-biomedical modeling: Merging image processing and computer aided design. in Proc. Annual Int. Conf. IEEE Engineering Medicine Biology Society, New Orleans, LA, 426–427.

HALLQUIST J. O. (1987). DYNA3D Course Notes, Lawrence Livermore National Laboratory.

HAUG E. (1995). Biomechanical models in vehicle accident simulation. In Proc. of PAM'95 Conference.

HIROTA G. 2002. An improved finite element contact model for anatomical simulations. PhD thesis, Department of Computer Science, University of North Carolina at Chapel Hill.

HSU W., HUGHES J., and KAUFMANN H. (1992). Direct manipulation of free-form deformations. Proceedings of SIGGRAPH'92, 177–184.

JAMES D. and PAI D. (August 1999). Artdefo accurate real time deformable objects. Proceedings of SIGGRAPH' 99 (Los Angeles, California), 65–72.

JORDANOGLOU J. (1969). Rib movement in health, kyphoscoliosis, and ankylosing spondylitis. Thorax 24, 407-414.

KAISS M. and TALLEC P. Le. (1996). La Modélisation numérique du contact ceil-trepan. Revue Européenne des Éléments Finis, 5(3):375-408.

KASS M. (1997). An introduction to continuum dynamics for computer graphics. In SIGGRAPH Course Notes. ACM SIGGRAPH.

KAUER M., VUSKOVIC V. and DUAL J. (1999). In-Vivo Measurement of Elasto-Mechanical Properties of Organic Tissue. In European Medical & Biological Engineering Conference, EMBEC'99, 270-271, Vienna, Austria.

KING HA, MOE J. H, BRADFORD D. S, WINTER R. B. (1983). The selection of fusion levels in thoracic idiopathic scoliosis. J. Bone Joint Surg., 65-A (9): 1302-1313.

KYRIACOU S. K., DAVATZIKOS C., ZINREICH S. J., and BRYAN N. R. (1998). Modeling Brain Pathology and Tissue Deformation Using a Finite Element Based Nonlinear Elastic Model. IEEE Transaction on Médical Imaging,

KYRIACOU S. K., DAVATZIKOS C., ZINREICH S. J, and BRYAN R. N. (1999). Nonlinear Elastic Registration of Brain Images with Tumor Pathology Using a Biomechanical Model. IEEE Transaction on Medical Imaging, 18(7):580-592.

LAVASTE F., ASSELINEAU A., DIOP A., GRANDJEAN J. L., LAURAIN J.M., SKALLI W., ROY-CAMILLE R. (1990). Protocole experimental pour la caracterisation mecanique de segments rachidiens et de materiels d'osteosynthese dorso-lombaires. Rachis 2-6:435-446.

LONSTEIN J. E., BRADFORD D. S., WINTER R. B., OGLIVE J. W. (1995). Moe's textbook of scoliosis and other spinal deformation. 3nd ed., W.B. Saunders Company, Philadelphia, USA, 685.

LUENBERGER D. G. (1984). Linear and Nonlinear Programming, Addison-Wesley.

MAASS H. and KÜHNAPFEL U. (1999). Noninvasive Measurement of Elastic Properties of Living Tissue. In 13th Internat. Congress on Computer Assisted Radiology and Surgery (CARS'99), 865-870, Paris, France.

MACCRACKEN R. and JOY K. (1996). Free-form deformations with lattices of arbitrary topology. Proceedings of SIGGRAPH'96, 81–188.

MACHIDA M. (1999), Pathogens of idiopathic scoliosis: experimental study in rats, Spine, 24: 1985-1989.

MARSDEN E. J. and HUGHES J.R. (1983). Thomas Mathematical Foundations of Elasticity, Prentice-Hall.

MATTHIES H. and STRANG G. (1979). The solution of nonlinear finite equations. Int. J. Num. Meth. Eng., 14, 1613-1626.

MAUREL W., Wu Y., THALMANN N. M. and THALMANN D. (1998). Biomechanical Models for Soft Tissue Simulation. Springer-Verlag.

MERLOZ P., TONETTI J., PITTEEET L., COULOMV M., LAVALL.e S., SAUTOT P. (1998). Pedicle screw placement using image guided technique. Clinical orthopaedics and related research, 354, 39-48.

MILLER K., CHINZEI K., ORSSENGO G., BEDNARZ P. (2000). Mechanical properties of brain tissue in-vivo: experiment and computer simulation. Journal of Biomechanics 33, 1369-1376.

MOE J. H, (1958). A critical analysis of methods of fusion for scoliosis: An evaluation of two hundred and sixty-six patients. J Bone Joint Surg. 1958; 40-A: 529-554.

MOW V.C., KUEI, S.C., LAI W.M., ARMSTRONG C.G. (1980). Biphasic creep and stress relaxation of articular cartilage: theory and experiment. ASME Journal of Biomechanical Engineering 102, p 73-84.

NEDEL L. and THALMANN D. (1998a). Modeling and deformation of human body using an anatomy-based approach. In Proc. Computer Animation '98, 34-40, Philadelphia. IEEE Computer Society Press.

NEDEL L. and THALMANN D. (1998b). Real Time Muscle Deformations Using Mass-Spring Systems. In Proc. CGI '98, IEEE Computer Society Press.

PATWARDAN A. G., GAVIN S., LI M. LORENZ T., Meade K.P., Zindrick M. (1990). Orthotic stabilization of thoracolumbar injuries, a biomechanical analysis of the Jewett hyperextension orthosis. Spine 15:654-661.

PETERSON L. E., NACHEMSON AL. (1995). Prediction of progression of the curve in girls who have adolescent idiopathic scoliosis of moderate severity. Logistic regression analysis based on data from The Brace Study of the Scoliosis Research Society. J Bone Joint Surg Am, 77(6): 823-827.

PÉRIÉ D., AUBIN C. E., PETIT Y., LABELLE H. and DANSEREAU J. (2004). Personalized biomechanical simulations of orthotic treatment in idiopathic scoliosis. Clinical Biomechanics, 19. 190-195.

PERDRIOLLER R. (1979), La scoliose: son étude tridimensionnelle, Maloine S.A., Paris, France.

PETIT Y. C.-É., and LABELLE H. (2004). Spinal shape changes resulting from scoliotic spine surgical instrumentation expressed as intervertebral rotations and centers of rotation. Journal of Biomechanics 37:173-180.

PICINBONO G. (2001). Modèles géométriques et physiques pour la simulation d'interventions chirurgicales. PhD thesis, Université de Nice-Sophia Antipolis.

PICINBONO G., DELINGETTE H. and AYACHE N. (May, 2001). Non-Linear and anisotropic elastiv soft tissue model for medical simulation. Proc. ICRA 2001 (IEEE International Conference on Robotics and Automation, 2, 1370-1375, Seoul, Korea, 21-26.

QIU T. X., TEO E. C., LEE K. K., NG H. W. and YANG K. (Dec. 2003). Validation of T10–T11 finite element model and determination of Instantaneous Axes of Rotations (IARs) in three anatomical planes. Spine.

RAMM E. (1980). Strategies for Tracing the Nonlinear Response Near the Limit Points. Nonlinear Finite Element Analysis in Structural Mechanics. ed. W. Wunderlich, E.Stein, K.J. Bathe, Proc. Europe-U.S.Workshop, Ruhr-UniversitÄat, Bochum, Germany,July 28-31.

RCAMI (1996) Second International Workshop on Robotics and Computer Assisted Medical Interventions (RCAMI'96), Bristol, UK, June 1996.

REDDY J. N. (1993). An Introduction to the Finite Element Method. McGraw-Hill, Inc., 2nd edition.

RHOMBERG A., BRECHBUHLER C., SZÉKELY G. and TRUSTER G. (1999). A Parallel Architecture for Interactive FEM Computations in a Surgery Simulator. IN Proceedings of the Parallel Computing conference, ParCo99, Delft, The Netherlands. The non-profit foundation Parco Conferences.

RIKS E. (1979). An Incremental Approach to the Solution of Snapping and Buckling Problems. Int. J. Solids & Structures 15 529-551.

ROAF R. (1966), Scoliosis, E & F Livinstone, Edinburgh, UK.

SAMANI A., BISHOP J., RAMSAY E., and PLEWES D. (1999). A 3D contact problem finite element model for breast shape deformation derived from mri data. In Proc. of ASB'99 Annual Conference.

SATAVA R. (1996). Medical virtual reality: The current status of the future. In Proc. Of 4th conf. Medecine Meets Virtual Reality (MMVR IV), 100-106.

SENET D.A.A., ASHER M.A., COOK L T., GOIN J.E., SHEUCH H.G., ORRICK J.M. (1984). Three dimensional analysis of right thoracic idiopathic scoliosis. Spine, 9 (4), 377-381.

SZÉKELY G., BAJKA M., BRECHBUHLER C., DUAL J., ENZLER R., HALLER U., HUG J., HUTTER R., IRONMONGER N., KAUER M., MEIER V., NIEDERER P., RHOMBERG A., SCHMID P., SCHWEITZER G., THALER M., VUSKOVIC V., and TRUSTER G. (2000a). Virtual Reality Based Simulation of Endoscopie Surgery. Presence, MIT press, 9(3):310-333.

SZÉKELY G., BRECHBUHLER C., HUTTER R., RHOMBERG A. and SCHMID P. (1998). Modelling of Soft Tissue Deformation for Laparoscopic Surgery Simulation. In WELLS, W. M. and OTHERS, editors, First International Conference on Medical Image Computing and Computer-Assisted Intervention MICCAI'98, numéro 1496 in Lecture Notes in Computer Science, 550-561, Cambridge MA, USA. Springer Verlag.

SZÉKELY G., BRECHBUHLER C., HUTTER R., RHOMBERG A. and SCHMID P. (2000b). Modelling of soft tissue deformation for laparoscopic surgery simulation. Medical Image Analysis, 4:57-66.

SAGAR M. A., BULLIVANT D., MALLINSON G., HUNTER P. and HUNTER I. (1994). A Virtual Environment and Model of the Eye for Surgical Simulation. In Computer Graphics (SIGGRAPH'94), 205-212.

SCHNABEL J. A. et al. (2001). Validation of non-rigid registration using finite element methods. In Proc. of IPMI'01 Conference, pages 344–357.

SCHWEIZERHOF K.H. and WRIGGERS P. (1986). Consistent Linearization for Path Following Methods in Nonlinear FE Analysis. Comp. Meth. Appl. Mech. Engng, 59, 261-279.

SEAGER M. (1988). A Slap for the massed. Lawrence Livermore Nat. Laboratory technical report, UCRL-100267.

SEDEBERG T. W. and PARRY S. R. (1986). Free-form deformations of solid geometric models. Computer Graphics, 20(4):151–160.

SEGERLIND L. (1984). Applied Finite Element Analysis. John Wiley and Sons, New York.

SEVASTIK, J.A. (1997). The pathogenesis of Idiopathic Scoliosis is skeletal origin Research into spinal deformities, 457-459.

SHEPHARD M. S. and GEORGES M. K. (1991). Three-Dimensional Mesh Generation by Finite Octree Technique. International Journal for Numerical Methods in Engineering, vol 32, 709-749.

SHIRAZI-ADL A., SHRIVASTAVA SC. and AHMED AM. (1984). Stress analysis of the lumbar disc-body unit in compression, a three-dimensional nonlinear finite element study. Spine 9: 120–134.

TEO EC., NG HW. (2001). Evaluation of the role of ligaments, facets and disc nucleus in lower cervical spine under compression and sagittal moments using finite element method. Med Eng Phys 23(3): 155–164.

TEO E.-C., QIU T.-X., YANG K., NG H.-W. and LEE K.-K. (2003). Biomechanical Effect of Thoracic Posterior Vertebral Elements on Patterns of the Loci of Instantaneous Axes of Rotation in Sagittal Plane.

TERZOPOULOS D. and FLEISCHE K. (1988a). Deformable models. The Visual Computer, 4:306-311.

TERZOPOULOS D. and FLEISCHER K. (1988b). Modeling inelastic deformation: Viscoelasticity, plasticity, fracture. Computer Graphics (SIGGRAPH'88), 22(4):269-278.

TERZOPOULOS D., PLATT J., BARR A. and FLEISCHER K. (1987). Elastically deformable models. Computer Graphics, 21(4):205-214. Proceedings of ACM SIGGRAPH'87 conference, Anaheim, CA.

THOMPSON J. M. T. and HUNT G. W. (1973). A general theory of elastic stability, John Willey &Sons.

VIDRASCU M. (1999). Simulation of the deformations of the liver by domain decomposition. In mini-symposim Decomposition de domaines de USNCCM99, Boulder, USA.

TROCHU F. (1993). A contouring program based on dual kriging interpolation. Eng. Comput. vol. 9, 160–177.

TSAP L., GOLDGOF D. B., SARKAR S., and HUANG W.-C. (1998). Efficient Nonlinear Finite Element Modeling of Nonrigid Objects via Optimization of Mesh Models. Computer Vision and Image Understanding, 69(3):330-350.

VERONDA D. R. and WESTMANN R. A. (1970). Mechanical Characterization of Skin-Finite Deformations. Journal of Biomechanics, 3:111-124.

VUSKOVIC V., BLASER R., and SPIGA A. (1999a.) Vision-Based Device for In-Vivo Measurement of Elasto-Mechanical Properties of Soft Tissues. uromech 406 Colloquium: In Image Processing Methods in Applied Mechanics, 227-230, Warsaw, Poland.

VUSKOVIC V., KAUER M. (1999b). DUAL J. and BAJKA M. Method and device for in-vivo measurement of elasto-mechanical properties of soft biological tissues. Machine Graphics & Vision International Journal, 8(4): 637-654.

VUSKOVIC V., KAUER M., SZÉKELY G., and REIDY M. (2000). Realistic Force Feedback for Virtual Reality Based Diagnostic Surgery Simulators. In IEEE International Conference on Robotics and Automotion: ICRA 2000, 1592-1598, San Francisco, CA.

WEINSTEIN S. L., PONSETI. (1983). Curve progression in idiopathic scoliosis. J Bone Joint Surg [Am], 65(4): 447-455.

WILSON. Dynamic analysis by numerical integration. http://www.csiberkeley.com/Tech_Info/20.pdf

WEINSTEIN SL., ZAVALA DC. (1981). IV. Ponseti. Idiopathic scoliosis: long-term follow-up and prognosis in untreated patients. J Bone Joint Surg [Am], 63(5): 702-712.

WHITE A.A, PANJABI M.M. (1990). Clinical biomechanics of the spine, 2nd ed., JB Lippincott, Philadelphia, USA.

WITKIN A. and HECKBERT P. (July 1994). Using particles to sample and control implicit surfaces. Proceedings of SIGGRAPH'94, 269–278.

WYNARSKY G. T., SCHULTZ A. B. (1991). Optimization of skeletal configuration: study of scoliosis correction biomechanics, J Biomech, 24-8: 721-732.

WYVILL G., MCPHEETERS C. and WYVILL B. (August 1986). Data structure for soft objects. The Visual Computer, 2(4):227–234.

YERRY M. A. and SHEPHARD M. S. (1984). Three-Dimensional Mesh Generation by Modified Octree Technique. International Journal for Numerical Methods in Engineering, vol. 20, 1965-1990.

ZHUANG Y. and CANNY J. (1999). Real-time Simulation of Physically Realistic Global Deformation. In IEEE Vis'99 Late Breaking Hot Topics, Los Angeles, California.

ZHUANG Y. and CANNY J. (2000). Haptic Interaction with Global Deformations. Dans IEEE International Conference on Robotics and Automotion: ICRA 2000, 2428-2433, San Francisco, CA.

ZHUANG Y. (2000). Real-time Simulation of Physically-Realistic Global Deformations. PhD thesis, Department of Electrical Engineering and Computer Science, UC Berkeley.

ZIENKIEWICZ O. C. and TAYLOR R. L. (2000a). The Finite Element Method: Basic Formulation and Linear Problems, volume 1: The Basis, 5th edition, Elsevier.

ZIENKIEWICZ O. C. and TAYLOR R. L. (2000b). The Finite Element Method: volume 2: Solid Mechanics, 5th edition, Elsevier.

APPENDIX A: FORMULATION OF DYNAMIC EQUATION

Implicit iterative algorithm

In 1959 Newmark presented a family of single-step integration methods for the solution of structural dynamic problems for blast and seismic loading. During the past 40 years Newmark's method has been applied to the dynamic analysis of many practical engineering structures. In addition, it has been modified and improved by many other researchers (Wilson).

In general, there is no closed-form solution to the system of differential equations (A.1). We have to solve it approximately by numerically integrating along the time dimension. Namely, given all information up to the current time step t_n, we have to solve the following system for time step t_{n+1} repeatedly:

$$M\ddot{u}^{n+1} + C\dot{u}^{n+1} + K\left(u^{n+1}\right) = F^{n+1} \tag{A.1}$$

(Zienkiewicz 2000a, p. 513). F^{n+1} is the external force exerted on object. In our case, it will mainly be produced by the external spring force.

Note that at time t_{n+1}, the information at all the previous time-steps $t_0, \cdots, t_n$, is considered as known. Namely $u^i, \dot{u}^i$ and $\ddot{u}^i$ are known for $i = 0, \cdots n$.

In the following, we apply the popular Newmark algorithm to the dynamic system to solve our linear and nonlinear equation. The Newmark recurrence scheme is one single-step integration method. Namely it only uses the known values at time t_n to solve (A.1), while ignoring the history before t_n. The Newmark recurrence scheme is as follows:

$$\begin{aligned} u^{n+1} &= u^n + \Delta t^n \dot{u} + \frac{1}{2}(1-\beta)\Delta t^2 \ddot{u}^n + \frac{1}{2}\beta \Delta t^2 \ddot{u}^{n+1} \\ \dot{u}^{n+1} &= \dot{u}^n + (1-\gamma)\Delta t \ddot{u}^t + \gamma \Delta t \ddot{u}^{n+1} \end{aligned} \tag{A.2}$$

(Zienkiewicz 2000a, p. 515), where β and γ are values between (0, 1). For convenience, we represent this system as:

$$R\left(\ddot{u}^{n+1}\right) = 0 . \tag{A.3}$$

Note that when $\beta \neq 0$, (A.3) is a nonlinear system of $\ddot{u}^{n+1}$ because $\ddot{u}^{n+1}$ appears in the nonlinear term $K\left(u^{n+1}\right)$. This leads to an implicit algorithm, such that at each time step, we have to solve a nonlinear system of $\ddot{u}^{n+1}$.

Solving a nonlinear system requires a Newton iteration type of algorithm. Namely, at each iteration, we have to compute the differential matrix $\frac{\partial R}{\partial \ddot{u}^{n+1}}$ and then solve a different linear system at each iteration. Although we can avoid the cost of inverting a differential matrix at each iteration by applying an iterative solver, such as a conjugate gradient solver, the cost of computing the differential matrix alone at each iteration is computationally intractable. We usually have to go through multiple iterations at each time step t_n. Therefore, an implicit integration algorithm makes simulation much slower for a FEM mesh of even moderate size. When $\beta = 0$, the unknown $\ddot{u}^{n+1}$ does not appear in the nonlinear term $K\left(u^{n+1}\right)$. This makes (A.3) a linear system of $\ddot{u}^{n+1}$. In particular, we choose the central difference method with $\gamma = \frac{1}{2}$. This leads to the following equalities:

$$
\begin{aligned}
u^{n+1} &= u^n + \dot{u}^n \Delta t + \frac{1}{2}\ddot{u}^n \Delta t^2 \\
\dot{u}^{n+1} &= \dot{u}^n + \frac{1}{2}\left(\ddot{u}^n + \ddot{u}^{n+1}\right)\Delta t \\
M\ddot{u}^{n+1} &= F^{n+1} - C\dot{u}^{n+1} - K\left(u^{n+1}\right)
\end{aligned}
\tag{A.4}
$$

Now we have converted the nonlinear system to three linear systems. Note that the first two equations are simple algebraic expressions, which are computationally cheap to evaluate.

In general the mass matrix M is a sparse matrix, but not diagonal. Therefore the third equation requires solving a large sparse linear system. Furthermore, the time step Δt_n is, in general, not a constant, therefore it is impossible to preprocess the system by computing the inverse (or the LU decomposition) of this large sparse matrix. We approximate the distributed mass with concentrated masses by lumping the mass matrix (Zienkiewicz 2000a, Reddy 1993): each row vector in the mass matrix is replaced by a

single value on the diagonal entry, which is equal to the sum of all the values in the corresponding row vector. At first glance, this approximation may look unacceptable. Actually it is mathematically equivalent to a special type of numerical volume integration algorithm for linear element: nodal Gauss quadrature. Numerical volume integration basically means sampling the value of the integrand at one or multiple points within the integration volume and then approximating the volume integration with a weighted sum of the sampled values. Given a linear finite element, if we sample exactly at the nodes of the element, (Zienkiewicz 2000b) shows that the mass matrix is automatically a diagonal matrix. Furthermore such a diagonal matrix is identical to the one obtained by lumping the original mass matrix. Hence the diagonal approximation of the mass matrix is simply an approximation with a low order numerical integration.

Intuitively we can also consider this diagonal mass matrix as approximating the mass with concentrated point mass at the nodal points of mesh. The original non-diagonal mass matrix is also an approximation of the inertia property of the continuum, including the total mass and moment of inertia. However this approximation still treats the mass as if it is distributed. The diagonalization process is equivalent to approximating the mass continuum as concentrated masses at each nodal point of the mesh. By doing this, we basically convert the distributed mass to a particle system.

As for any implicit integration algorithm, stability is always a concern. The time integration algorithm is unconditionally stable for $2\beta \geq \gamma \geq 1/2$. For other combinations the algorithm may be conditionally stable or unconditionally unstable. The combination $\beta = 1/4, \gamma = 1/2$, known as the trapezoidal rule, leads to a second order accuracy and to a maximum dissipation of the higher energy items in time, and unconditionally stable modes. According to (Reddy 1993), for the zero damping Newmark's method is conditionally stable if $\gamma \geq 1/2, \beta \leq 1/2$ and $\Delta t \leq \dfrac{1}{\omega_{\max}\sqrt{r/2 - \beta}}$.

So the central difference recurrence scheme is conditionally stable when the time step satisfies the following:

$$\Delta t \leq \frac{2}{\omega_{\max}}, \tag{A.5}$$

where $\omega_{\max}$ is the maximum natural frequency of the dynamic system (A.1).

In the dynamic case the linearization follows the time domain discretization. The usual procedure expresses the displacements at the present time $t + \Delta t$ as a function of the displacements u, velocities and accelerations at the time t, leading to a Newmark-β time integration scheme. Finally, we obtain a balance equation:

$$K\left(u^{n+1}\right)du = F^{n+1\,ext} - F\left(u^{n+1}\right)^{\text{int}} \tag{A.6}$$

Solving the equation implies calculation of the gradient stiffness matrix K at each iteration. This method is called full Newton-Raphson. This is very expensive in the finite element analysis and therefore a modified procedure is usually used. One way is to use the gradient matrix from the first time step. This method is called the initial stress method and it usually leads to more iterations as the solution advances over time. To accelerate convergence, we use a Newton-Raphson with line search algorithm in each iteration as described below.

Newton-Raphson algorithm

After discretizing the continuous time system using the Newmark method, we obtain a nonlinear multidimensional equation. The Newton-Raphson method is considered as the most robust and this locally efficient solver is applied to the solution of the final nonlinear algebraic equation. The method makes explicit use of the derivative of the function for which we wish to find the zero. If we suppose we know more local information about $f(u)$, such as that used in developing a Taylor expansion of the function about the point $f(u_0)$, we can often find the zeroes more quickly. Suppose we have reason to believe that there is a zero of $f(u)$ near the point u_0. The Taylor expansion for $f(u)$ about u_0 can be written as:

$$f(u) = f(u_0) + f'(u_0)(u - u_0) + \frac{f''(u_0)}{2!}(u - u_0)^2 + \cdots \tag{A.7}$$

Let us drop the terms of this expansion beyond the first order term, and write:

$$f(u) \approx f(u_0) + f'(u_0)(u - u_0) \tag{A.8}$$

After we set $f(u) = 0$ to find the next approximation, u_1, to the zero of $f(u)$, we can apply $u_1 = u_0 - \dfrac{f(u_0)}{f'(u_0)}$ as an iteration scheme to converge on the final zero solution.

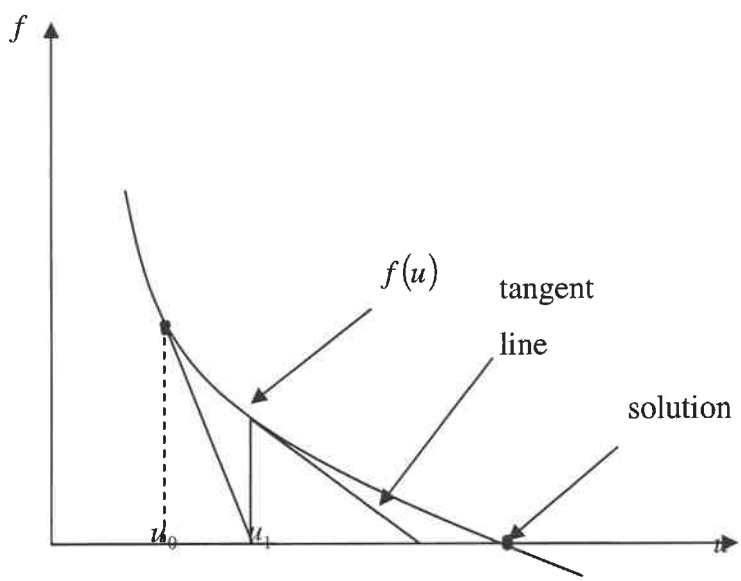

Figure A.1: Schematic representation of the Newton-Raphson method showing the iteration from the initial guess u_0 to the next approximation u_1 to the zero of the function $f(u)$

The Newton-Raphson method is illustrated graphically here for a simple monotonic function $f(u)$. The iteration from u_0, an initial guess for the zero of $f(u)$, involves drawing the tangent to $f(u)$ from the point $(u_0, f(u_0))$ until it intersects the $f = 0$ axis. The point of intersection is the next approximate value u_1. The process is repeated until the change in the intersection point is smaller than the requested tolerance or precision, i.e. until $|f(u_1)| < \varepsilon$ for some specified tolerance ε. The convergence of the method could

be invalid if an initial guess for u_0 was too close to any point with $\dot{f} = 0$, in which case the initial step from u_0 to u_1 is quite large, possibly far away from the zero of interest in the application. To improve the Newton Raphson method's convergence ability, we apply a linear search method to compute the optimal solution in each Newton iteration. We optimize the objective along a given line: $opt\{f(u + s\Delta u) : s \geq 0\}$, where u is a previous displacement point and s is a non-negative scalar, and u is the tangent direction vector of the point. A tolerance, and maximal search times, could be used to control the times of line search.

In the line search algorithm initially the displacements are updated with

$$u_{i+1}^{n+1} = u_i^{n+1} + s\Delta u_i^n \qquad \text{(A.9)}$$

(Zienkiewicz 200b p.30). where s is a parameter between 0 and 1 that is determined iteratively by a line search procedure. Convergence is checked by observing displacement parameter changes or the energy norm.

$\left\|\Delta u_i^n\right\| \leq \varepsilon_d$, $\left\|R_i^{n+1}\right\| \leq \varepsilon_e$, $R^{n+1} = \left(F^{n+1}\right)^{ext} - \left(F^{n+1}\right)^{\text{int}}\left(u^{n+1}\right)$ where ε_d and ε_e are the tolerances for the displacement change and energy norm respectively. Convergence can also be determined by comparison of relative residual norms $\left\|R_i^{n+1}\right\| < \varepsilon\left\|R_1^{n+1}\right\|$ (Zienkiewicz 200b p.30). If convergence is not attained, the displacements are updated by $u_{i+1}^{n+1} = u_i^{n+1} + s\Delta u_i^n$ and the iterations continue. When the solution diverges or convergence is not achieved after a number of iterations, the tangent stiffness matrix K is revised using the current estimated geometry and the equilibrium iterations continue.

To update the stiffness matrix, any of four methods can be adopted:

- Broyden's first method
- Davidon
- Davidon-Fletcher-Powell
- Broyden-Fletcher-Goldfarb-Shano (BFGS).

According to (Hallquist 1987) these methods involving a line search are slightly more expensive in terms of the computation but lead to more stable progress. Details of these

methods can be found in (Luenberger 1984). For our purpose, we will use the BFGS method because of large number of unknowns and limited memory.

One of the advantages of using this algorithm is that the determinant of the global stiffness matrix K and the change in the condition number of K can be easily computed in order to control the updates, especially in the situations when K becomes nearly singular and the condition number very large (Matthies 1979). All the methods mentioned earlier for solving the nonlinear equations are in fact algorithms for minimization for convex problems (Luenberger 1984). In our situation, the potential energy of deformation is the function which needs to be minimized in order to find the solution. As long as the potential energy of deformation remains strictly convex, all those methods will converge. The methods will fail when the energy is no longer a convex function. In this case, a different approach is needed and the problem is still open (Gao 1995, 1996, 1997 and 2000). For example, a particular case is the situation when the energy becomes semi-positive definite, which is the buckling situation. However, for this particular case there are some algorithms that permit us to pass over this limit point, but only for some structures that can exhibit either a snap-through or a snap-back phenomenon.

ÉCOLE POLYTECHNIQUE DE MONTRÉAL
3 9334 00314293 0